FOREWORD

This is the final annual report of investigations performed by the Flight Propulsion Laboratory Department, General Electric Company, under the auspices of the Department of Defense through the Advanced Research Projects Agency, Order No. 24-62, Task 6, Project No. 4776, "Materials Thermal Properties." The work was done under Contract No. AF33(616)-6841, administered by the Air Force Materials Laboratory, Research & Technology Division. Mr. P.W. Dimiduk of that organization served as Project Engineer.

The investigations reported here were performed during the period 1 July 1962 through 30 Oct. 1963 under the general direction of Dr. G.M. Kibler, Flight Propulsion Laboratory Department, General Electric Company. The individual tasks were performed as follows:

Vapor Pressure of Refractories - by Drs. T.F. Lyon & M.J. Linevsky

Spectral Emissivity of Refractory Materials - by V.J. DeSantis

ABSTRACT

In continuation of work begun earlier, vapor pressure studies of hafnium and tantalum nitride were completed using Knudsen effusion method combined with a gas collection and measuring system. The vaporization of ZrB_2 has been studied, also by a Knudsen effusion method, modified in this application to obtain the effusion rate by continuous weighing of condensed effusate. Matrix isolation studies of the vapor from ZrO_2 and HfO_2 have been made as have additional measurements with ThO_2 which was a subject of an earlier investigation. Resonance line absorption photometry has been applied to ZrB_2. The results obtained are presented and discussed.

Normal spectral emissivity data on single crystal tungsten, pyrolytic graphite and tantalum nitride have been obtained and are reported herein.

This technical report has been reviewed and is approved.

Jules I. Wittebort

JULES I. WITTEBORT
Chief, Thermal & Solid State Br.
Materials Physics Division
Air Force Materials Laboratory

TABLE OF CONTENTS

TABLE OF CONTENTS (CONT'D)

LIST OF ILLUSTRATIONS

LIST OF ILLUSTRATIONS (cont'd.)

LIST OF ILLUSTRATIONS (Cont'd.)

LIST OF TABLES

LIST OF TABLES (cont'd.)

I INTRODUCTION

In November, 1959, research was undertaken to provide data, design information, and selection criteria for materials suitable for uncooled rocket nozzle fabrication and able to withstand rocket propellants of the future with their forecast higher temperatures and new chemical products. At the time, such rocket propellant compositions being undefined and unidentified, it appeared most appropriate to determine the physical, chemical, and thermodynamic property data for selected refractories of possible application. Having done so, the later identification of these propellants and the knowledge of the properties of their combustion products would permit prediction of the suitability of the materials studied on chemical and physical bases.

The program undertaken at that time consisted of three separate areas of investigation: 1) a study of the process of thermal degradation of plastics, including the rates thereof as well as the amount and identity of products; 2) a study of the vaporization of selected refractories at very high temperatures, including measurement of vapor pressures, rates of vaporization, identity of vapor species, and accessible thermodynamic functions, all by a number of diverse methods appropriate to the materials chosen; and 3) a study of normal spectral emissivities of selected refractories, also at very high temperatures, to provide radiative heat transfer data. Except for the plastics investigation which terminated in June, 1962, the program continued to the present without change in concept or objective.

This report presents details of the work and the results obtained during the period 1 July 1962 through Oct., 1963. No effort has been made to include the results of earlier studies, reported in prior annual reports (References 1, 2, and 3) page 83.

Manuscript released by authors October, 1963, for publication as a WADD Technical Report.

II VAPOR PRESSURES OF REFRACTORY MATERIALS

A. Background

A study of the vapor pressures of selected refractory materials together with the computation of thermodynamic data accessible from such studies was undertaken at the start of the over-all program in 1959. This program has extended to the present (Oct. 1963). During the period of its existence, three annual reports have been published. They are WADD Technical Report 60-646, Parts I, II, and III[1,2,3]. * This is the fourth and last annual report of this work.

By the end of June, 1962, vaporization studies on TaC, ZrC, HfC, TiC, and WC had been completed by the Langmuir evaporation method. Knudsen effusion had been applied to ZrN and similar study of HfN had nearly been completed. The matrix isolation technique had been applied to ThO_2; and the vapors over two carbides, TiC and ZrC, and one boride, TiB_2, had been studied by resonance line absorption photometry.

Results obtained in continuing these investigations are presented in this report. The Knudsen effusion method has been used in completing the vaporization study of HfN, TaN and ZrB_2. Matrix isolation studies on ZrO_2 and HfO_2 as well as further work on ThO_2 have been made. Vapors over ZrB_2 have been studied by resonance line absorption photometry. Thermodynamic property data obtained from the work are also discussed herein.

B. Knudsen Effusion Studies

1. Hafnium Nitride

In the previous annual report[3], data on nitrogen pressures over hafnium nitride were presented. Results from three series of measurements with cells of different orifice areas were in agreement at high nitrogen content but showed a definite dependence on orifice area at lower nitrogen content. It was suggested that this behavior could be due either to the relatively slow diffusion of nitrogen in HfN or to a non-unit evaporation coefficient, with the former explanation being more likely.

* [1,2,3] See References, Page 83

Results of two additional series of measurements on HfN are presented here. They support the conclusion that previously observed discrepancies are due to the diffusion limitation. The same apparatus and experimental procedure as in the earlier work[3] was employed. For the Series IV measurements, the previously prepared HfN (atomic fraction nitrogen = 0.501) was ground and sieved to -325 mesh and placed in a tungsten cell with orifice area 6.49×10^{-3} cm^2. Under these conditions, effusion measurements were made until the atom fraction of nitrogen was reduced to 0.464. The results of this series are in good agreement with the Series III[3] measurements previously obtained.

After final nitrogen analysis of the material from the Series IV measurements, the remainder was placed in a cell with orifice area -0.0190 cm^2, which is 2.92 times greater than the orifice area for Series IV. The Series V measurements were then made until the nitrogen atom fraction had been further reduced to 0.433.

The first several measurements in Series V gave apparent nitrogen pressures in good agreement with the final measurements of Series IV. This fact indicates that the evaporation coefficient of HfN is sufficiently close to unity that it has no large effect on the apparent pressure measured with different orifice areas. However, as the total nitrogen content was reduced, the apparent nitrogen pressures deviated farther from a reasonable extrapolation of the Series IV measurements. This deviation is consistent with the postulated diffusion limitation.

A total of five series of measurements have now been made on HfN under various conditions. Pertinent data relating to these series are summarized in Table 1 where the initial and final composition is given along with the cell orifice area, the weight of material in the cell, and an indication of the particle size. If the diffusion limitation is indeed the correct explanation for the discrepancies in the pressure measurements, then small particle size, small orifice area and large quantities of material in the cell would give higher apparent pressures; that is, pressures closer to the equilibrium value.

The data from all five series of measurements are compared in Figures 1 and 2 at the temperatures 2031 and 2238°K. As may be seen from these curves, the lowest pressures were obtained in the Series II measurements in which the conditions were most unfavorable for obtaining the equilibrium pressure; that is, a small amount of coarse material in a cell with large orifice (see Table 1). At the other extreme, the experimental conditions for Series III and IV were the most favorable, and the highest pressures were, in fact, obtained in these two series. The agreement between the Series V and Series IV

TABLE 1

EXPERIMENTAL CONDITIONS - HfN MEASUREMENTS

Series	Composition (atom %N) Initial	Final	Particle Size	Orifice Area (cm^2)	Initial Wt. HfN (gm.)
I	50.1	44.2	Coarse	.0304	.98520
II	50.1	40.8	Coarse	.0515	.59893
III	50.1	45.3	-200 Mesh	.00629	1.53269
IV	50.1	46.4	-325	.00649	1.49454
V	46.4	43.3	-325	.01897	1.12103

measurements, cited above, may be noted near 0.463 atom fraction nitrogen with the Series V data falling considerably lower at lower nitrogen concentrations.

In order to determine the equilibrium pressure of nitrogen over HfN using the effusion method, it is now apparent that one must go to rather extreme conditions to minimize the rate at which the over-all composition of the solid changes. The complete results of the Series IV measurements are given in Table 2. These data, along with the results of the Series III measurements[3], are shown in Figure 3. For the sake of clarity, the data points for the temperatures 1715 and 1601°K have been omitted. Generally good agreement between the two sets of measurements may be noted, especially near the composition of 0.49 atom fraction. The maximum difference in the two series may be accounted for by errors of about 0.002 in the determination of the composition, which is well within the accuracy of the measurement. There is no really good evidence that the data shown in Figure 3 actually represent the equilibrium pressure of nitrogen over HfN and perhaps even smaller orifices and finer particles would give higher pressures. It is believed, however, that these values approximate the equilibrium pressure over HfN and, in any case, set a lower limit on the equilibrium pressure.

2. The System Tantalum-Nitrogen

a) Experimental method and materials preparation

The apparatus and experimental methods used for the study of nitrogen pressures in the tantalum-nitrogen system are essentially the same as previously reported[3] for the ZrN and HfN studies. All nitrogen analyses reported here were made by the Kjeldahl method.

Three separate tantalum-nitrogen compositions were prepared for this study by heating pure tantalum metal powder under

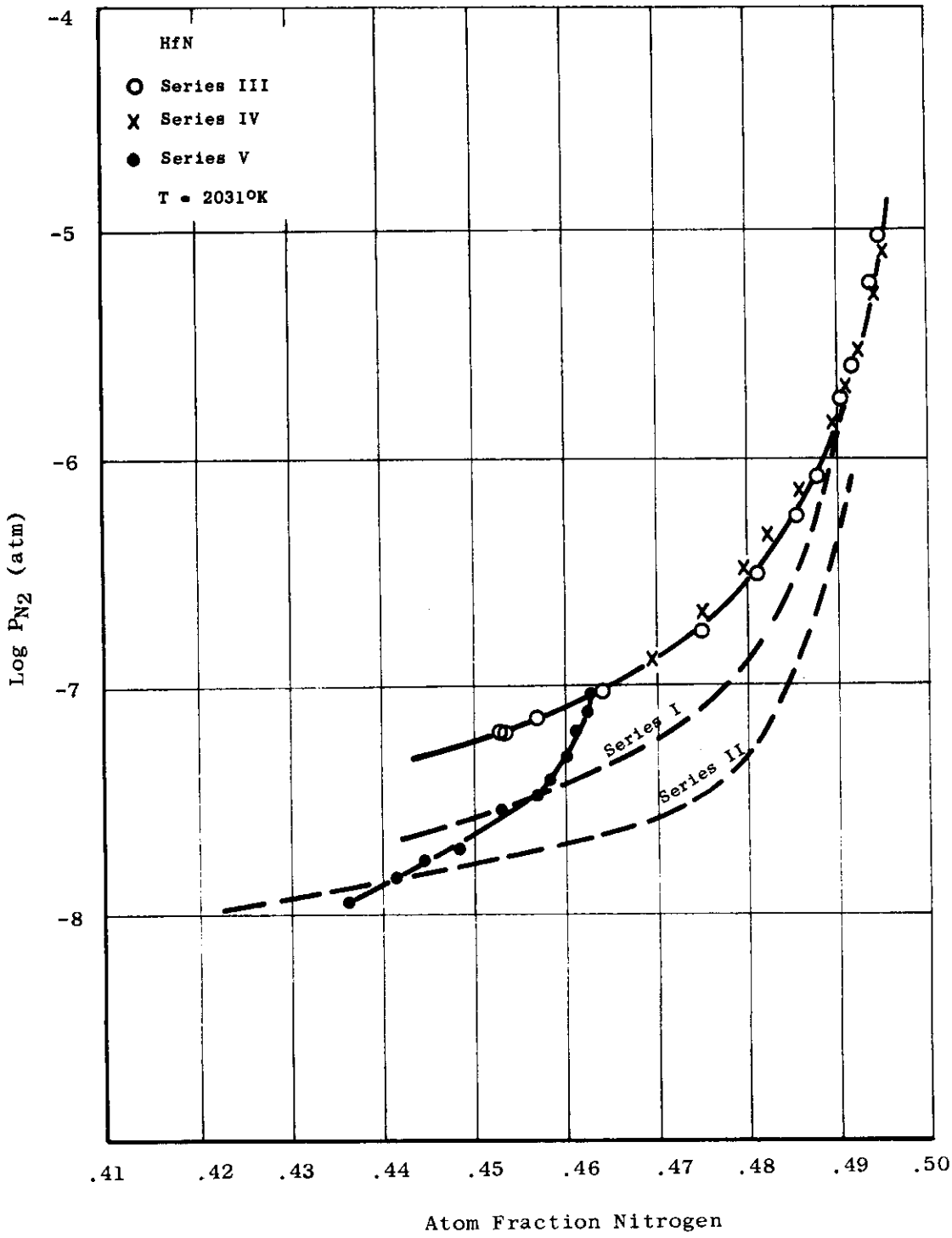

Figure 1. Nitrogen Pressure vs. Composition for Hafnium Nitride. Isotherm at 2031°K

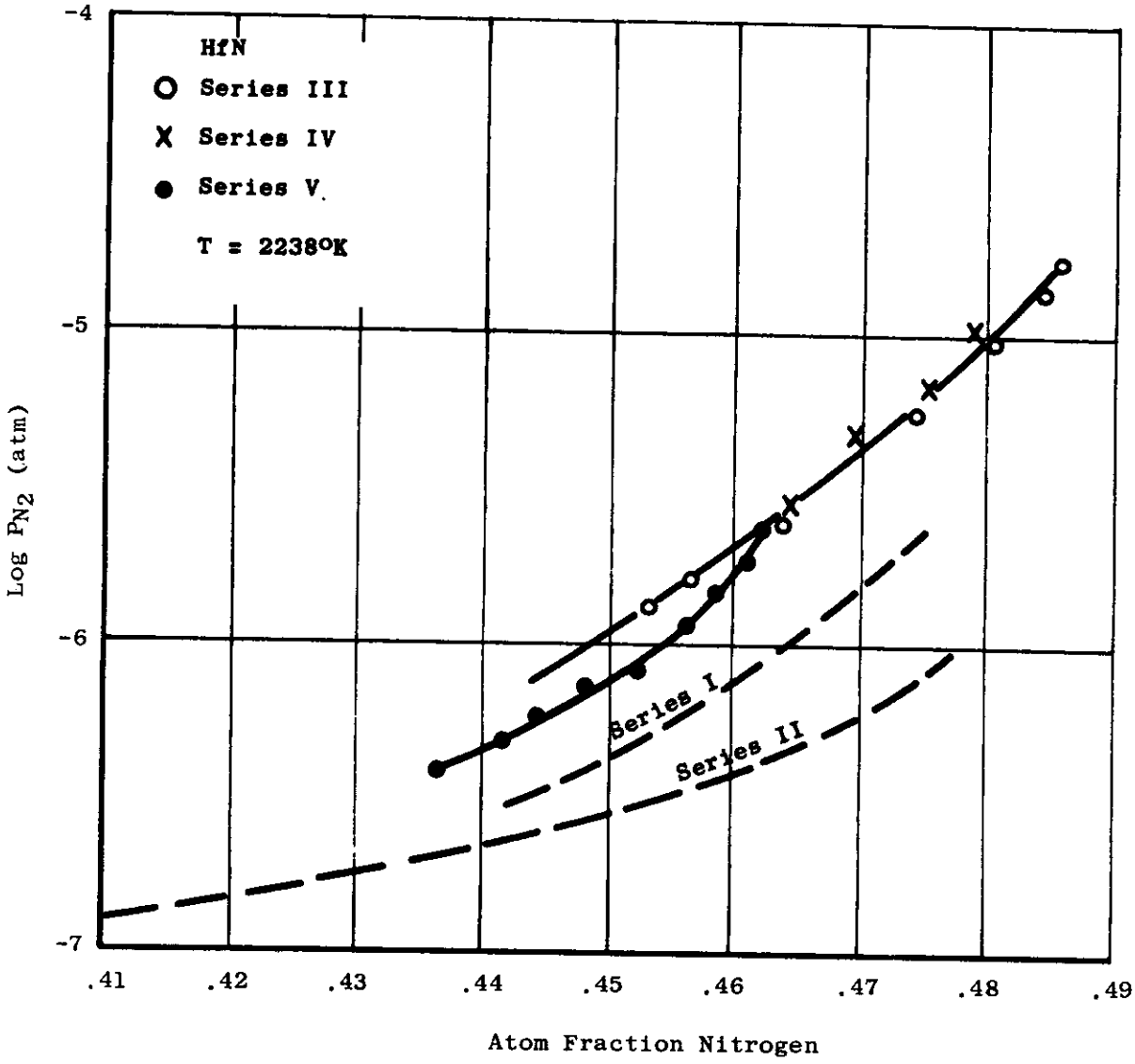

Figure 2. Nitrogen Pressure vs. Composition for Hafnium Nitride. Isotherm at 2238°K

TABLE 2

NITROGEN PRESSURE OVER HfN SERIES IV

P_{N_2} = nitrogen pressure in atmosphere
η_n = atom fraction nitrogen in HfN

Series IV: orifice area = .00649 cm^2; -325 mesh HfN

T(°K)	Log P_{N_2}	η_n
1601	-6.10	.5006
1601	-6.32	.5000
1601	-6.69	.4995
1601	-7.32	.4987
1715	-5.52	.5002
1715	-5.99	.4993
1715	-6.37	.4986
1715	-6.74	.4981
1715	-7.21	.4973
1823	-5.26	.4997
1823	-5.63	.4988
1823	-5.83	.4982
1823	-6.21	.4973
1823	-6.54	.4966
1823	-6.84	.4957
1823	-6.99	.4950
1823	-7.19	.4939
1823	-7.41	.4926
1823	-7.40	.4908
1823	-7.54	.4900
1931	-5.18	.4977
1931	-5.50	.4967
1931	-5.81	.4958
1931	-6.00	.4949
1931	-6.19	.4940
1931	-6.39	.4925
1931	-6.56	.4908
1931	-6.64	.4900
1931	-6.97	.4861
1931	-7.16	.4825
1931	-7.28	.4797
1931	-7.51	.4750

TABLE 2 (Continued)

T(°K)	log P_{N_2}	η_n
2031	-5.09	.4952
2031	-5.29	.4942
2031	-5.52	.4926
2031	-5.70	.4909
2031	-5.84	.4898
2031	-6.14	.4860
2031	-6.34	.4824
2031	-6.49	.4797
2031	-6.67	.4750
2031	-6.89	.4695
2031	-7.07	.4639
2133	-5.02	.4902
2133	-5.34	.4864
2133	-5.54	.4827
2133	-5.69	.4799
2133	-5.89	.4749
2133	-6.12	.4694
2133	-6.29	.4640
2238	-4.98	.4789
2238	-5.16	.4754
2238	-5.32	.4698
2238	-5.54	.4643
2356	-4.72	.4685
2356	-4.84	.4649

one atmosphere of purified nitrogen. The tantalum used as starting material was obtained from the Kawecki Chemical Company and the analysis supplied by the vendor is given in Table 3 along with gas analysis performed here by the vacuum fusion method. Good agreement may be noted between the two analyses. Table 4 shows the analyses and conditions for preparation of three compositions. Comparison with Table 3 shows a small amount of oxygen pickup during preparation. The samples TN (3) and TN (4) were single phase TaN determined from X-ray diffraction patterns. TN (2) was found to contain a small amount of the Ta_2N phase. Indications are that the TaN phase has a rather narrow composition range near stoichiometric.

b) Description of measurements performed

Measurements of nitrogen pressure over various tantalum-nitrogen compositions have been made over the range 0.02 to 0.49 atom fraction N. A summary of the four series of measurements is shown in Table 5. The Series I measurements were made using the material

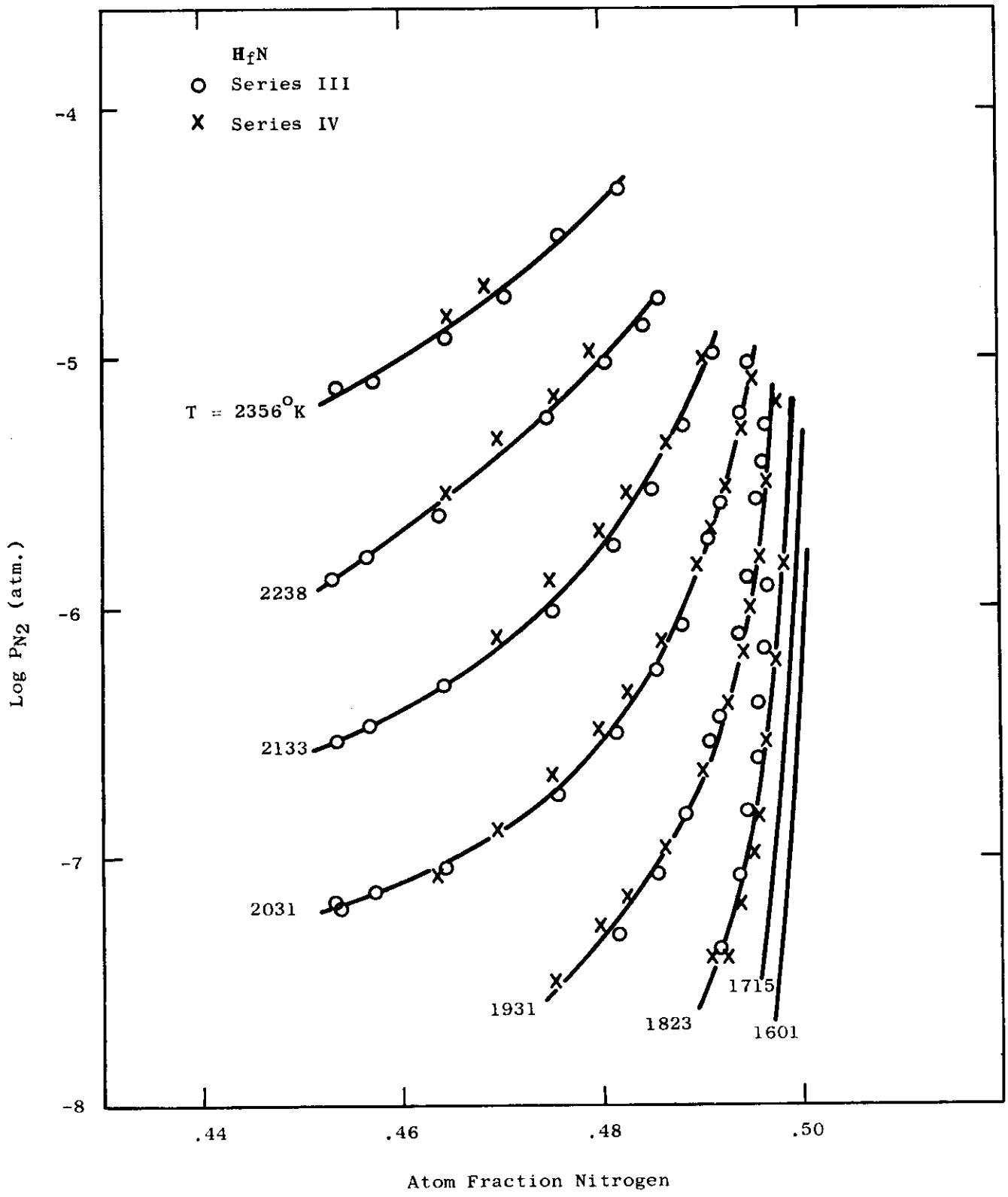

Figure 3. Pressure-Composition Isotherms For HfN Series III And Series IV Measurements

TABLE 3

CHEMICAL ANALYSIS OF TANTALUM POWDER

KAWECKI CHEMICAL COMPANY LOT NO. E-208C

Element	Kawecki and ppm by wt.	Our Analysis ppm by wt.
O	600	530
N	120	120
H	Not Reported	330
C	700	
Nb	<100	
Ti	< 50	
Fe	120	
Mn	< 10	
Si	70	
Sn	50	
Cr	< 10	
Ca	10	
Na	< 50	
Al	< 50	
Ni	10	

TABLE 4

PREPARATION OF

TANTALUM-NITROGEN COMPOSITIONS

Sample Identification	Time at Temp.	Composition Atom Fraction N	Phases	Analysis (ppm) O	Analysis (ppm) H
TN (2)	13½ Hrs at 1500°C	.427	TaN+Ta_2N	-	-
TN (3)	18½ Hrs at 1500°C	.488	TaN	750	60
TN (4)	23 Hrs at 1300°C	.485	TaN	1600	11

TABLE 5

EXPERIMENTAL CONDITIONS FOR Ta - N SYSTEM

Series		Composition (Atom Fraction N)	Phases	Orifice Area (cm^2)	Initial Wt. (gm)
I	Initial	.488	TaN	5.43×10^{-3}	.86181
I	Final	.359	Ta_2N		
II	Initial	.359	Ta_2N	5.43×10^{-3}	.71736
II	Final	.017	Ta		
III	Initial	.472	TaN + Ta_2N	5.25×10^{-3}	.93820
III	Intermediate	.433	TaN + Ta_2N		
III	Final	.325	Ta_2N		
IV	Initial	.485	TaN	5.25×10^{-3}	.97116
IV	Intermediate	.473	TaN + Ta_2N		
IV	Final	.349	Ta_2N		

TN (3) (see Table 4) which was single phase TaN with composition 0.488 atom fraction N. This series was concluded after atom fraction N of 0.359 had been reached at which point the material was single phase Ta_2N. The Series II measurements were made with this single phase Ta_2N and continued through the two phase region, Ta + Ta_2N, and into the single phase Ta region to the composition 0.017 atom fraction nitrogen. Due to the rather strange behavior of the Series I data, additional measurements were made in the high nitrogen region.

The Series III measurements were started at the composition 0.472 using the two phase material TN (2) (see Table 4). At the composition 0.433 atom fraction N, material was removed from the cell for nitrogen and X-ray analyses and found to be still two phase TaN + Ta_2N. Measurements were then resumed and continued to the composition 0.325 atom fraction N. Data from this third series of measurements gave nitrogen pressures considerably less than those obtained in the Series I measurements in the two phase region. A fourth series of measurements was then undertaken using the single phase material TN (4) (see Table 4). This series was interrupted at 0.473 atom fraction N for analyses and found to be two phase at this composition. The series was then resumed and terminated at 0.349 atom fraction N. Nitrogen pressures from this series were lower than those obtained in the previous two series in the same region.

c) Pressure measurements at high nitrogen contents

As stated above, rather wide variations have been encountered between the three series of measurements at nitrogen concentrations 0.33 to 0.48 atom fraction N which range essentially covers the two phase region, TaN + Ta_2N. In figures 4, 5, and 6, isotherms from the various series are plotted at temperatures of 1341, 1420, and 1498°K. The discrepancies between the various measurements are apparent in these curves with the Series I measurements being as much as a factor of 30 greater than the Series IV measurements. In Figures 5 and 6 it may be noted that the data converge near 0.33, the stoichiometric composition of Ta_2N.

It should be immediately pointed out that the origin of these variations is not the same as for the discrepancies in the HfN data since essentially the same orifice area and weight of material was used in each series (see Table 5) and for each series the particle size was the same (-325 mesh).

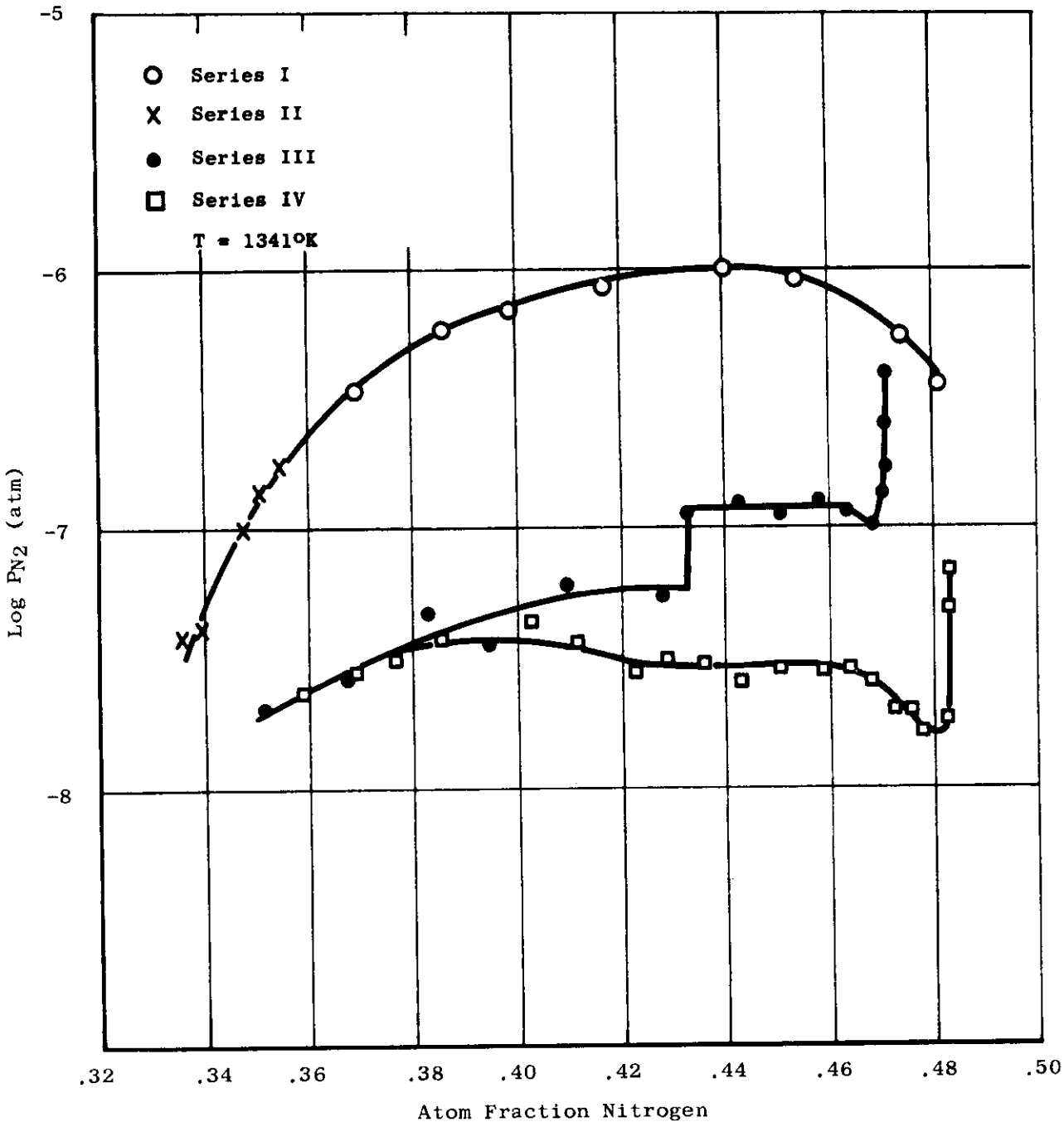

Figure 4. Nitrogen Pressure vs. Composition in Tantalum - Nitrogen System. Isotherm at 1341°K

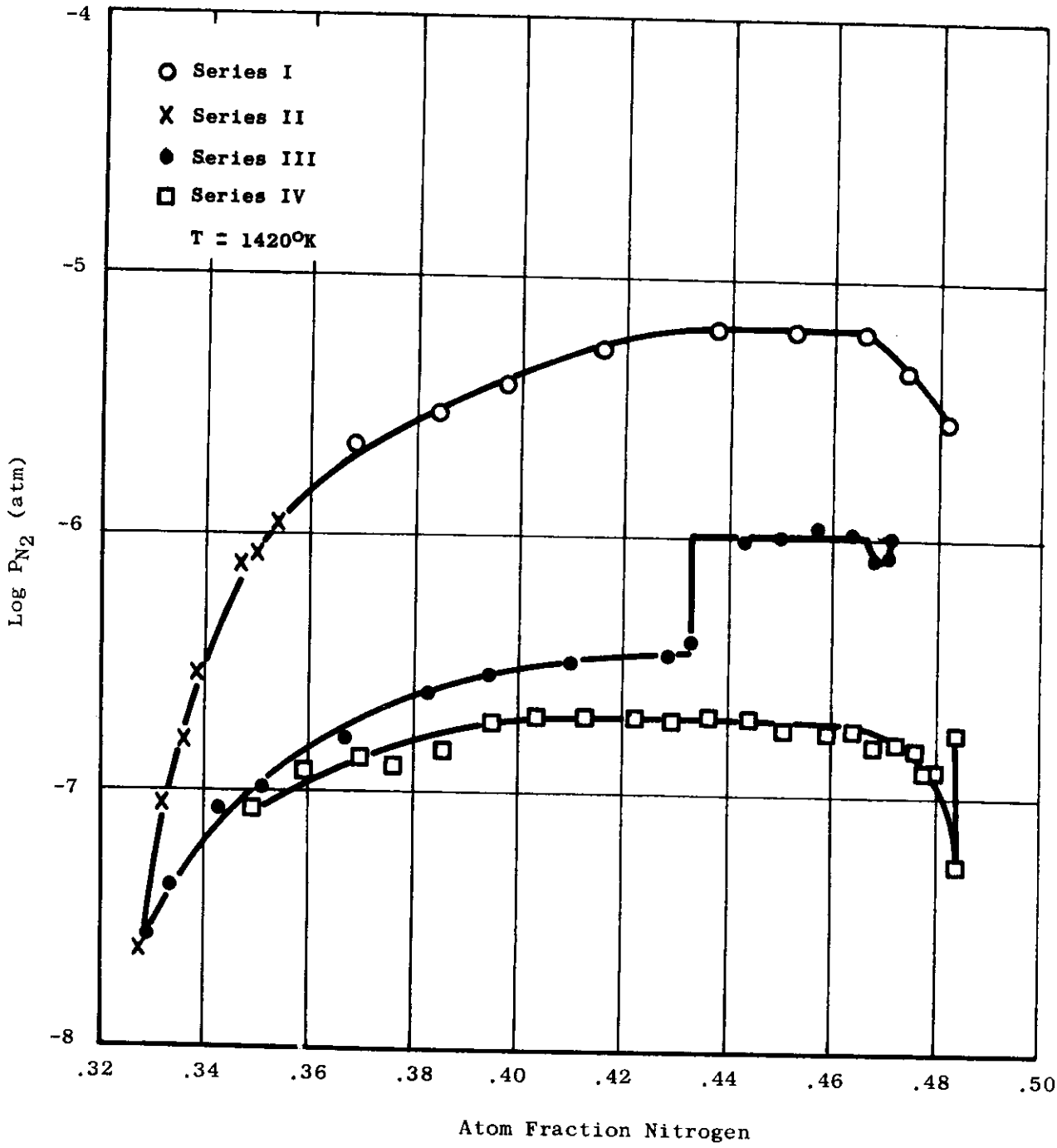

Figure 5. Nitrogen Pressure vs. Composition in Tantalum - Nitrogen System. Isotherm at 1420°K

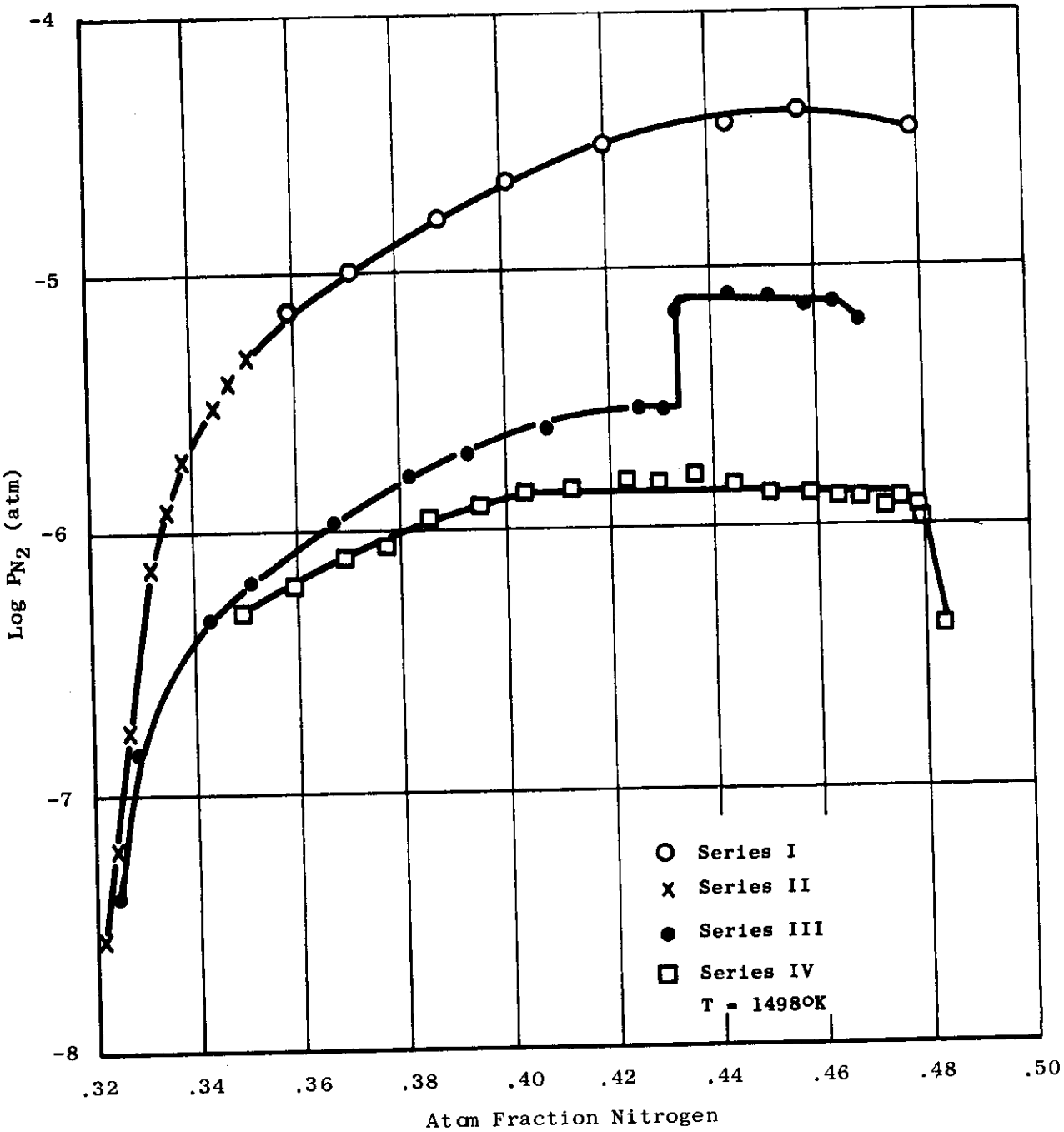

Figure 6. Nitrogen Pressure vs. Composition in Tantalum - Nitrogen System. Isotherm at 1498°K

It seems possible that the variations encountered here are due to the presence of metastable phases. In order to investigate this possibility, X-ray diffraction patterns were made at the intermediate compositions in Series III and IV as shown in Table 5. Only the phases TaN and/or Ta_2N were found at any composition greater than 0.33 atom fraction N (see Tables 4 and 5). However, since the material was not quenched and actually cooled rather slowly from the temperature of the effusion measurement due to the relatively large mass of the cell, it is not certain that the observed phases are actually representative of the high temperature equilibrium.

Some nitrogen pressure measurements over TaN have been reported in older literature. Andrews[4], by a static measurement method, reported an equilibrium nitrogen pressure over TaN of 6.8×10^{-5} atm. at 2240°K. This value is much too low at this composition to be consistent with any of the data reported here. In addition, she found rather constant (within a factor of 2) pressures within the composition range of 0.1 to 0.5 atom fraction N. In contrast, the data reported here (see Fig. 9) show an increase of pressure of several orders of magnitude within the single phase Ta_2N region. Slade and Higson[5], using a static method, found nitrogen pressures of 5.9×10^{-4} and 1.3×10^{-3} atm. at 1443 and 1581°K respectively for a composition "probably" TaN. Both these values are higher than any of the present measurements at about 0.48 atom fraction N and corresponding temperatures. They are not unreasonable values for the equilibrium nitrogen pressure over single phase TaN. However, it is clear that neither of these older studies offer evidence to support the data of one of the present series of measurements over another at high nitrogen contents.

Thus, while no good evidence can be offered in support of the postulated presence of metastable phases in the data reported here, this still seems to be the only reasonable explanation for the discrepancies. In this connection, a quotation by J. S. Anderson[6] seems quite appropriate: "Hence quite low concentrations of impurity atoms can play a disproportionate role in preventing attainment of equilibrium, by retaining metastable random phases, supersaturated with defects."

If the existence of metastable phases is in fact the proper explanation for the wide variations in observed nitrogen pressure, then the lowest pressures would give the lowest free energy of formation and hence represent the most stable phases. As may be seen in Figures 4, 5, and 6, the Series IV measurements were the lowest pressures of the three series, and in addition, this series was most well behaved in that more nearly constant pressures were obtained in the two phase region. It is thus believed that the Series IV measurements most nearly represent the true equilibrium pressure over the two phase system TaN plus Ta_2N. The complete results of this series of

measurements is given in Table 6.

Some additional remarks might be made concerning the shape of the isotherms in Figures 4, 5, and 6. In the Series III measurements, after the material had been removed for analysis, appreciably lower pressures were observed when the cell was replaced and measurements resumed. This may be seen in the Series III isotherms as a sharp break at 0.432 atom fraction N. The reason for this is not clear and no such behavior was noted in the Series IV measurements.

At the beginning of the Series IV measurements (at about 48% N), a sharp decrease and then an increase in pressure was found as may be seen in the curves. This effect has been noted at phase boundaries by Veleckis, et al[7] in similar effusion studies and was attributed to delayed nucleation of the phase being formed. Thus, it would appear that nucleation of Ta_2N occurred during the period of these initial measurements. This same behavior occurred in the Series III measurements to a somewhat lesser extent even though this material was initially two phase.

d) Pressure measurements at low nitrogen contents

The Series II measurements, from 0.36 to 0.02 atom fraction nitrogen, extended through the Ta_2N region, through the two phase region Ta_2N plus Ta solid solution, and well into the Ta solution single phase region of the tantalum-nitrogen phase diagram. The complete results of this series of measurements are given in Table 7.

The low-nitrogen region (up to Ta_2N) has been investigated by Gebhardt et al[8] using a system in which the nitrogen pressure was obtained by isothermal absorption of N_2 until equilibrium was obtained. It is interesting to compare the results of these static measurements with the dynamic results obtained here. Due to the non-uniform temperature of their sample, Gebhardt, et al did not obtain well behaved isotherms and in particular their pressures in the two phase region were not constant with composition. Such behavior is contrary to the requirements for thermodynamic equilibrium. The presently reported data show similar behavior in the two phase region but this is rather typical of this technique as has been pointed out by Veleckis, et al[7].

The data obtained here may be compared with the idealized isotherms which Gebhardt, et al[8] deduced from their data. Such a comparison is shown in Figure 7 at the two temperatures 2012 and 1842°K. Good agreement between the two sets of data may be noted at about 0.30 atom fraction N and also at about 0.02 atom fraction N. The presently reported pressures are more strongly dependent on composition in the Ta_2N region than are the Gebhardt data. At the other extreme, the Gebhardt data increase more rapidly with composition than do the

TABLE 6

NITROGEN PRESSURE OVER Ta - N SERIES IV

P_{N2} = Nitrogen pressure in atmospheres

η_N = Atom fraction nitrogen in TaN

Series IV: Orifice area = 0.00525 cm^2
TaN particle size = -325 mesh

TiK	Log P_{N_2}	η_N
1277	-7.27	0.4839
1277	-7.73	0.4838
1277	-7.92	0.4837
1341	-7.17	0.4838
1341	-7.31	0.4838
1341	-7.73	0.4837
1341	-7.78	0.4786
1341	-7.70	0.4755
1341	-7.70	0.4726
1341	-7.58	0.4681
1341	-7.55	0.4640
1341	-7.55	0.4587
1341	-7.55	0.4508
1341	-7.58	0.4437
1341	-7.52	0.4363
1341	-7.51	0.4292
1341	-7.58	0.4226
1341	-7.43	0.4120
1341	-7.36	0.4031
1341	-7.51	0.3947
1341	-7.43	0.3856
1341	-7.51	0.3766
1341	-7.53	0.3688
1341	-7.63	0.3590
1420	-6.75	0.4837
1420	-7.27	0.4836
1420	-6.90	0.4798
1420	-6.90	0.4786
1420	-6.82	0.4754
1420	-6.80	0.4726
1420	-6.80	0.4681
1420	-6.76	0.4639

TABLE 6

(Continued)

TiK	Log P_{N_2}	η_N
1420	-6.77	0.4586
1420	-6.75	0.4507
1420	-6.72	0.4436
1420	-6.70	0.4363
1420	-6.72	0.4292
1420	-6.71	0.4225
1420	-6.71	0.4121
1420	-6.70	0.4031
1420	-6.73	0.3947
1420	-6.84	0.3855
1420	-6.88	0.3765
1420	-6.87	0.3689
1420	-6.92	0.3590
1420	-7.08	0.3492
1498	-5.93	0.4784
1498	-5.89	0.4752
1498	-5.93	0.4723
1498	-5.89	0.4678
1498	-5.89	0.4637
1498	-5.87	0.4580
1498	-5.88	0.4504
1498	-5.84	0.4433
1498	-5.81	0.4364
1498	-5.83	0.4293
1498	-5.82	0.4227
1498	-5.85	0.4122
1498	-5.85	0.4032
1498	-5.90	0.3948
1498	-5.97	0.3857
1498	-6.05	0.3766
1498	-6.10	0.3690
1498	-6.21	0.3591
1498	-6.31	0.3493
1498	-6.38	0.4836
1498	-5.97	0.4796
1578	-5.48	0.4831
1578	-5.04	0.4786
1578	-4.99	0.4755
1578	-5.00	0.4727
1578	-5.03	0.4682
1578	-5.02	0.4640

TABLE 6

(Continued)

TiK	Log P_{N_2}	η_N
1578	-5.03	0.4587
1578	-5.00	0.4508
1578	-5.01	0.4437
1578	-5.00	0.4369
1578	-5.04	0.4297
1578	-5.02	0.4229
1578	-5.03	0.4133
1578	-5.05	0.4037
1578	-5.11	0.3950
1578	-5.17	0.3860
1578	-5.27	0.3771
1578	-5.33	0.3696
1578	-5.48	0.3594
1578	-5.61	0.3494

TABLE 7

NITROGEN PRESSURE OVER TaN SERIES II

PN_2 = Nitrogen pressure in atmospheres

^{a}N = Atom fraction nitrogen in TaN

Series II: Orifice area = 0.00543 cm^2
TaN particle size = -325 mesh

T, °K	log PN_2	^{a}N	T, °K	log PN_2	^{a}K
1277	-7.26	0.3551	1668	-5.55	0.3224
1277	-7.50	0.3516	1668	-5.97	0.3187
1277	-7.67	0.3475	1668	-6.26	0.3158
			1668	-6.56	0.3120
1341	-6.76	0.3550	1668	-6.77	0.3095
1341	-6.85	0.3514	1668	-7.02	0.3063
1341	-7.01	0.3475	1668	-7.34	0.3010
1341	-7.38	0.3399			
1341	-7.42	0.3357	1761	-4.89	0.3199
			1761	-5.17	0.3164
1420	-5.96	0.3543	1761	-5.55	0.3123
1420	-6.08	0.3502	1761	-5.85	0.3091
1420	-6.12	0.3469	1761	-6.10	0.3056
1420	-6.54	0.3397	1761	-6.39	0.3007
1420	-6.80	0.3366	1761	-6.59	0.2965
1420	-7.03	0.3329	1761	-6.91	0.2890
1420	-7.62	0.3280	1761	-7.06	0.2820
			1761	-7.06	0.2761
1498	-5.33	0.3516	1761	-7.08	0.2681
1498	-5.42	0.3476	1761	-7.10	0.2618
1498	-5.52	0.3448	1761	-7.11	0.2525
1498	-5.72	0.3387	1761	-7.02	0.2418
1498	-5.91	0.3357	1761	-7.07	0.2279
1498	-6.14	0.3324	1761	-7.11	0.2165
1498	-6.75	0.3278	1761	-7.10	0.2073
1498	-7.20	0.3250	1761	-7.12	0.1905
1498	-7.55	0.3224	1761	-7.14	0.1734
			1761	-7.15	0.1622
1578	-5.03	0.3400	1761	-7.22	0.1530
1578	-5.10	0.3367	1761	-7.23	0.1416
1578	-5.31	0.3330	1761	-7.29	0.1311
1578	-5.90	0.3271	1761	-7.30	0.1218
1578	-6.29	0.3246	1761	-7.29	0.1129
1578	-6.65	0.3221	1761	-7.37	0.1030
1578	-7.00	0.3191	1761	-7.37	0.0972
1578	-7.22	0.3161	1761	-7.41	0.0918
			1761	-7.48	0.0858
1668	-4.87	0.3285	1761	-7.54	0.0763
1668	-5.23	0.3251	1761	-7.57	0.0703

TABLE 7

(Continued)

T, °K	log PN_2	n_N	T, °K	log PN_2	n_K
1842	-4.98	0.3101	1928	-5.75	0.2056
1842	-5.17	0.3064	1928	-5.81	0.1887
1842	-5.52	0.3011	1928	-5.86	0.1716
1842	-5.70	0.2960	1928	-5.87	0.1613
1842	-6.08	0.2885	1928	-5.89	0.1522
1842	-6.35	0.2816	1928	-5.93	0.1408
1842	-6.37	0.2758	1928	-5.96	0.1298
1842	-6.38	0.2678	1928	-5.98	0.1212
1842	-6.37	0.2648	1928	-6.04	0.1117
1842	-6.35	0.2520	1928	-6.09	0.1023
1842	-6.41	0.2415	1928	-6.10	0.0966
1842	-6.43	0.2263	1928	-6.13	0.0911
1842	-6.48	0.2163	1928	-6.16	0.0848
1842	-6.47	0.2070	1928	-6.24	0.0759
1942	-6.46	0.1900	1928	-6.30	0.0697
1842	-6.54	0.1730	1928	-6.40	0.0630
1842	-6.55	0.1620	1928	-6.48	0.0526
1842	-6.61	0.1528	1928	-6.57	0.0470
1842	-6.61	0.1414	1928	-6.71	0.0400
1842	-6.69	0.1309	1928	-6.85	0.0344
1842	-6.70	0.1216	1928	-6.99	0.0277
1842	-6.75	0.1126	1928	-7.21	0.0211
1842	-6.80	0.1029	1928	-7.31	0.0179
1842	-6.82	0.0971			
1842	-6.87	0.0917	2012	-4.72	0.2831
1842	-6.88	0.0855	2012	-4.86	0.2769
1842	-6.85	0.0763	2012	-5.03	0.2682
1842	-6.94	0.0701	2012	-5.05	0.2585
1842	-7.00	0.0634	2012	-5.05	0.2480
1842	-7.13	0.0530	2012	-5.09	0.2380
1842	-7.17	0.0479	2012	-5.10	0.2232
1842	-7.26	0.0402	2012	-5.13	0.2126
1842	-7.34	0.0346	2012	-5.15	0.2005
1842	-7.50	0.0279	2012	-5.21	0.1829
			2012	-5.24	0.1686
1928	-4.99	0.2967	2012	-5.26	0.1589
1928	-5.25	0.2892	2012	-5.27	0.1488
1928	-5.56	0.2804	2012	-5.33	0.1384
1928	-5.64	0.2742	2012	-5.36	0.1282
1928	-5.67	0.2670	2012	-5.40	0.1189
1928	-5.66	0.2608	2012	-5.45	0.1089
1928	-5.69	0.2511	2012	-5.47	0.1007
1928	-5.71	0.2409	2012	-5.50	0.0951
1928	-5.72	0.2266	2012	-5.55	0.0889
1928	-5.78	0.2155	2012	-5.58	0.0833

TABLE 7

(Continued)

T, °K	log PN_2	a_N	T, °K	log PN_2	a_K
2012	-5.65	0.0747	2109	-4.76	0.1228
2012	-5.71	0.0684	2109	-4.83	0.1143
2012	-5.80	0.0621	2109	-4.84	0.1042
2012	-5.93	0.0520	2109	-4.88	0.0983
2012	-6.04	0.0472	2109	-4.93	0.0928
2012	-6.18	0.0395	2109	-5.00	0.0864
2012	-6.29	0.0339	2109	-5.02	0.0785
2012	-6.47	0.0274	2109	-5.11	0.0703
2012	-6.70	0.0208	2109	-5.20	0.0636
2012	-6.83	0.0175	2109	-5.35	0.0533
			2109	-5.51	0.0450
2109	-4.40	0.2630	2109	-5.63	0.0383
2109	-4.45	0.2538	2109	-5.80	0.0327
2109	-4.50	0.2437	2109	-5.95	0.0267
2109	-4.49	0.2299	2109	-6.18	0.0202
2109	-4.51	0.2181	2109	-6.34	0.0173
2109	-4.52	0.2090			
2109	-4.52	0.1923	2208	-4.89	0.0481
2109	-4.61	0.1748	2208	-5.06	0.0403
2109	-4.61	0.1639	2208	-5.19	0.0348
2109	-4.65	0.1547	2208	-5.36	0.0279
2109	-4.68	0.1434	2208	-5.63	0.0213
2109	-4.73	0.1331	2208	-5.78	0.0181

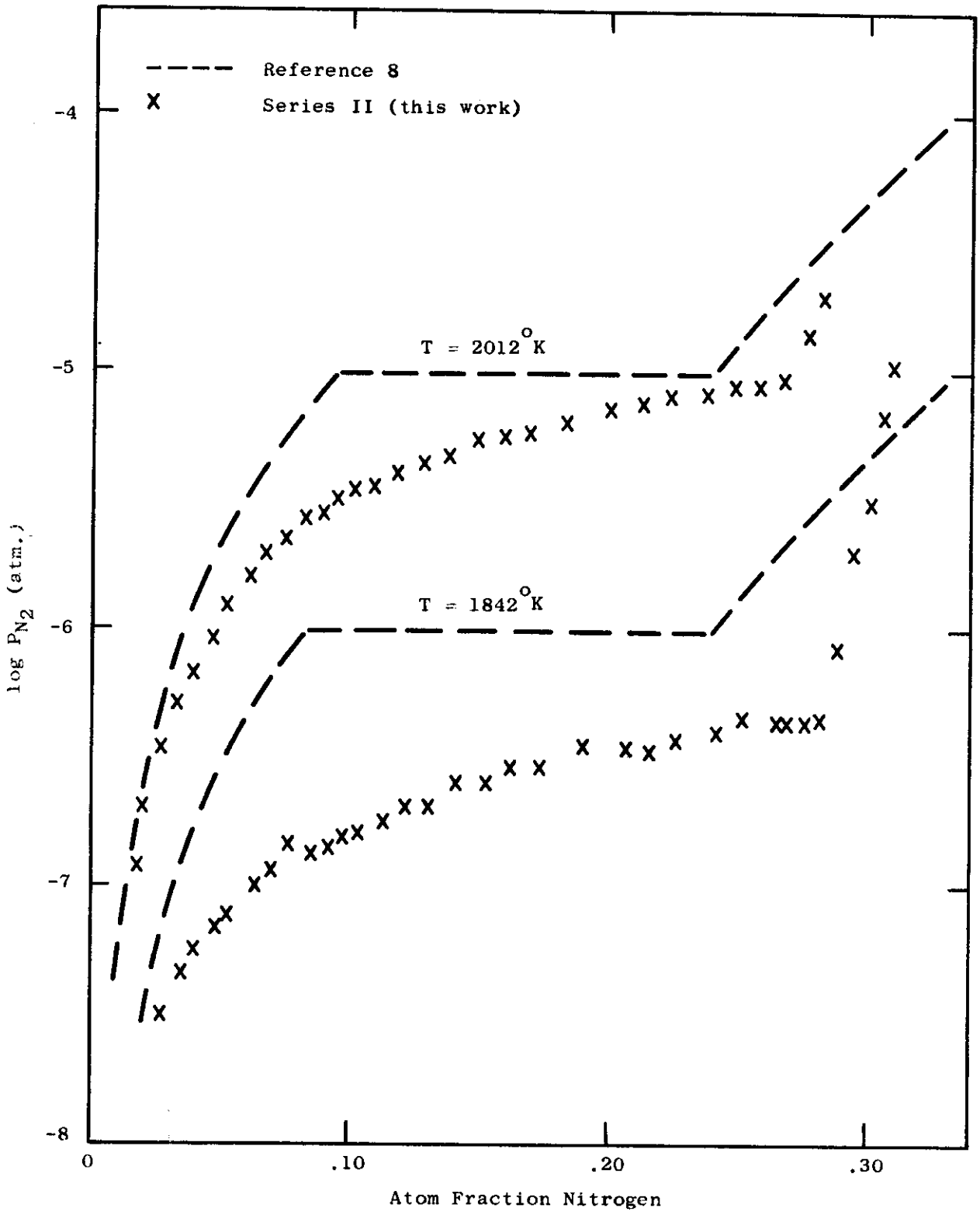

Figure 7. Comparison Of Idealized Static Measurements (Ref. 8) With Series II Measurements At 2012 and 1842°K

dynamic measurements in the single phase Ta solid solution region. The Gebhardt pressures are proportional to concentration to the 2.4 power in this region. This is not in accord with Sievert's law which predicts pressures proportional to the square of the concentration. On the other hand, our data at 2012° are proportional to concentration to the 1.94 power at the lowest concentrations and at 1842° are proportional to the concentration to the 1.43 power. Pemsler[9] found good agreement with Sievert's law at 2663°K but not at higher temperatures. Figure 7 also shows the sharp break in the isotherms at the low nitrogen limit of the Ta_2N phase. Our data indicate this boundary at 0.270 and 0.282 atom fraction N for the temperatures 2012 and 1842°K respectively while Gebhardt reports the boundary at about 0.24 in this temperature region. The low nitrogen limit of the two phase region cannot be accurately determined from the present data due to the gradual decrease in pressure throughout the two phase region.

Pemsler[9] has measured the equilibrium nitrogen pressure in the Ta solid solution region at temperatures between 2660 and 3290°K. In Figure 8, the data of Pemsler, the idealized measurements of Gebhardt, et al, and the data from the present study are compared by plotting log P_{N_2} vs $\frac{1}{T}$ at the composition 0.03 atom fraction nitrogen. The agreement between the three independent sets of measurements is fairly good. One may note from Figure 8 that Pemsler's data are higher than those of Gebhardt by a factor of about 4. However, both of these sets of data have essentially the same slope giving a partial molar enthalpy of solution of N_2, in the solid solution, of -87 kcal per mole N_2 for the Gebhardt data and -88 kcal per mole N_2 for the Pemsler data. Our measurements have about the same value as the Gebhardt data but a greater slope leading to a partial molar enthalpy of solution of -112 kcal per mole N_2 at this composition.

e) Most probable values for isotherm

From the preceding discussion, one may construct a diagram showing the most probable behavior of the pressure-composition isotherms consistent with the experimental observations and the requirements of equilibrium thermodynamics. Such a diagram is shown in Figure 9. For the sake of clarity, the Series IV data above 0.48 and the Series II data above 0.33 have been omitted from Figure 9. The general behavior of these omitted values may be seen in Figures 4, 5, and 6. These isotherms were obtained from the following considerations: From the phase analyses of the various compositions shown in Tables 4, and 5 and from the behavior of the pressure measurements at high nitrogen contents, the TaN phase is found to have a narrow range of homogeneity extending to no less than 0.48 atom fraction N. In the two phase region TaN plus Ta_2N, pressures are constant with composition at the level given by the Series IV measurements. The experimental data fall below this level toward the low nitrogen end of the two phase region due to depletion of the TaN phase. This effect is rather

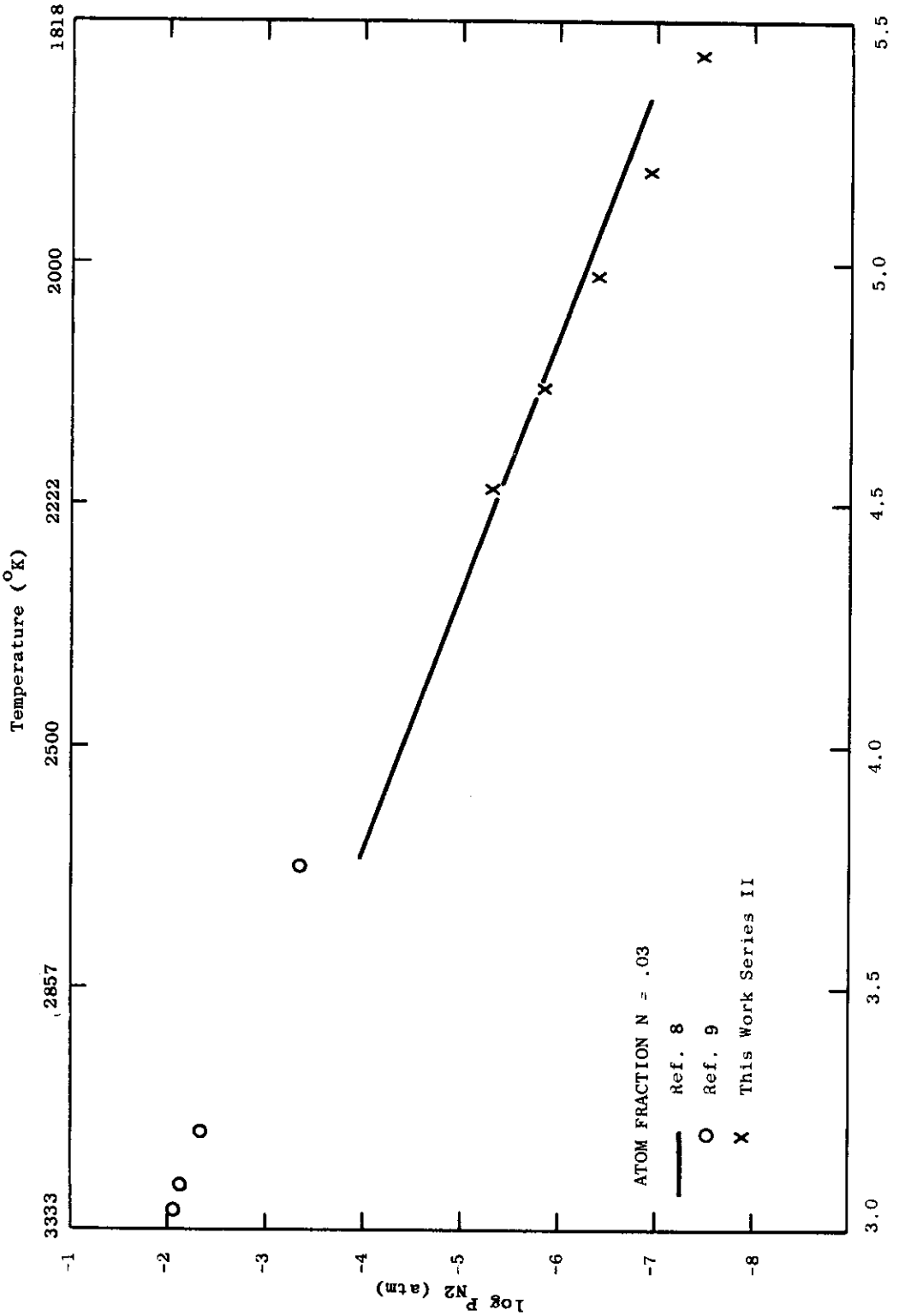

Figure 8. Log P vs. $\frac{1}{T}$ for TaN, Comparing Data Of Pemsler[9], Gebhardt(8), and This Work At 0.03 Atom Fraction Nitrogen

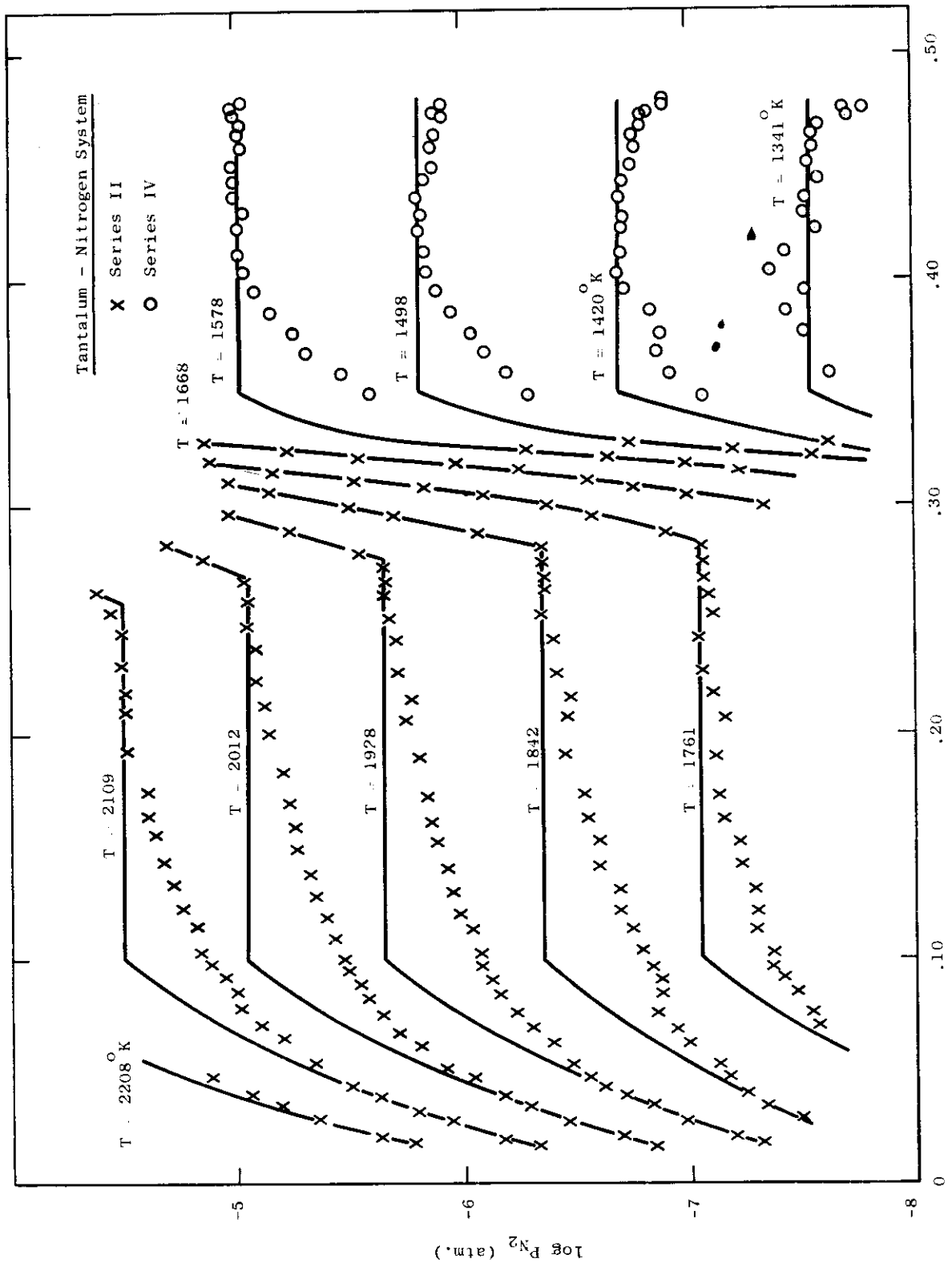

Figure 9. Pressure-Composition Isotherms In The TaN System

typical of the experimental technique and has been discussed by Veleckis et al.[7] No evidence for the existence of a hexagonal δ phase, homogeneous in the range 0.445 to 0.475 atom fraction N has been found in this study. Such a phase had been reported by Schönberg[10].

The high nitrogen limit of the Ta_2N phase was estimated to be at about 0.35 atom fraction N. The low nitrogen limit is determined by the sharp break in the Series II isotherms at 0.28 to 0.26 atom fraction N between 1761 and 2109°K. The range of homogeneity of the Ta_2N phase found here may be compared with 0.291 to 0.333 atom fraction N[11], 0.29 to 0.31 atom fraction N[10] and 0.24 to 0.33 atom fraction N[8].

The isotherms of Figure 9 are constant with composition in the two phase region Ta_2N plus Ta solution at a level determined by the experimental data at the high nitrogen boundary. At lower nitrogen contents, the data again fall below this level. The limit of solubility of nitrogen in Ta was taken as 0.10 atom fraction N between 1761 and 2109°K in agreement with Gebhardt, et al[8].

3. Zirconium Diboride

a. Apparatus

The method used for studying zirconium diboride vaporization is the Knudsen effusion method in which the weight of a known fraction of condensed effusate is continuously recorded. The apparatus used for the study is shown diagrammatically in Figure 10. The balance mounted above the effusion cell and within the vacuum system, is a Cahn RG Recording Electronic Microbalance. Suspended from one end of the balance beam by means of a chain of quartz fibers is a conical quartz collector located with its base directly over the effusion cell, where it intercepts a fraction of the effusate. The effusion cell is heated by direct RF coupling to a three turn coil of a 25 KW induction heater. A "water curtain" heat exchanger is used to cool the quartz furnace tube in which cell and collector are enclosed. This type of cooling was chosen because it requires less space than others and thus permits closer coupling between coil and cell. The swiftly flowing, continuous film (or "curtain") of water which bathes the outside walls of the tube, is formed by a flow of water through the narrow annulus between the upper conical cup and the furnace tube wall. Auxiliary jets in the immediate vicinity of the coil provide additional cooling water.

The effusion cell is mounted on three 0.050" diameter tungsten rods which fit holes drilled near the periphery of the cell bottom. The lower end of each tungsten support rod is turned to fit 0.039" ID quartz capillary tubing, vertical sections of which are fused to the quartz support tube. Details of cell and support are shown in Figure 11 in which the mounted collector cone can also be seen.

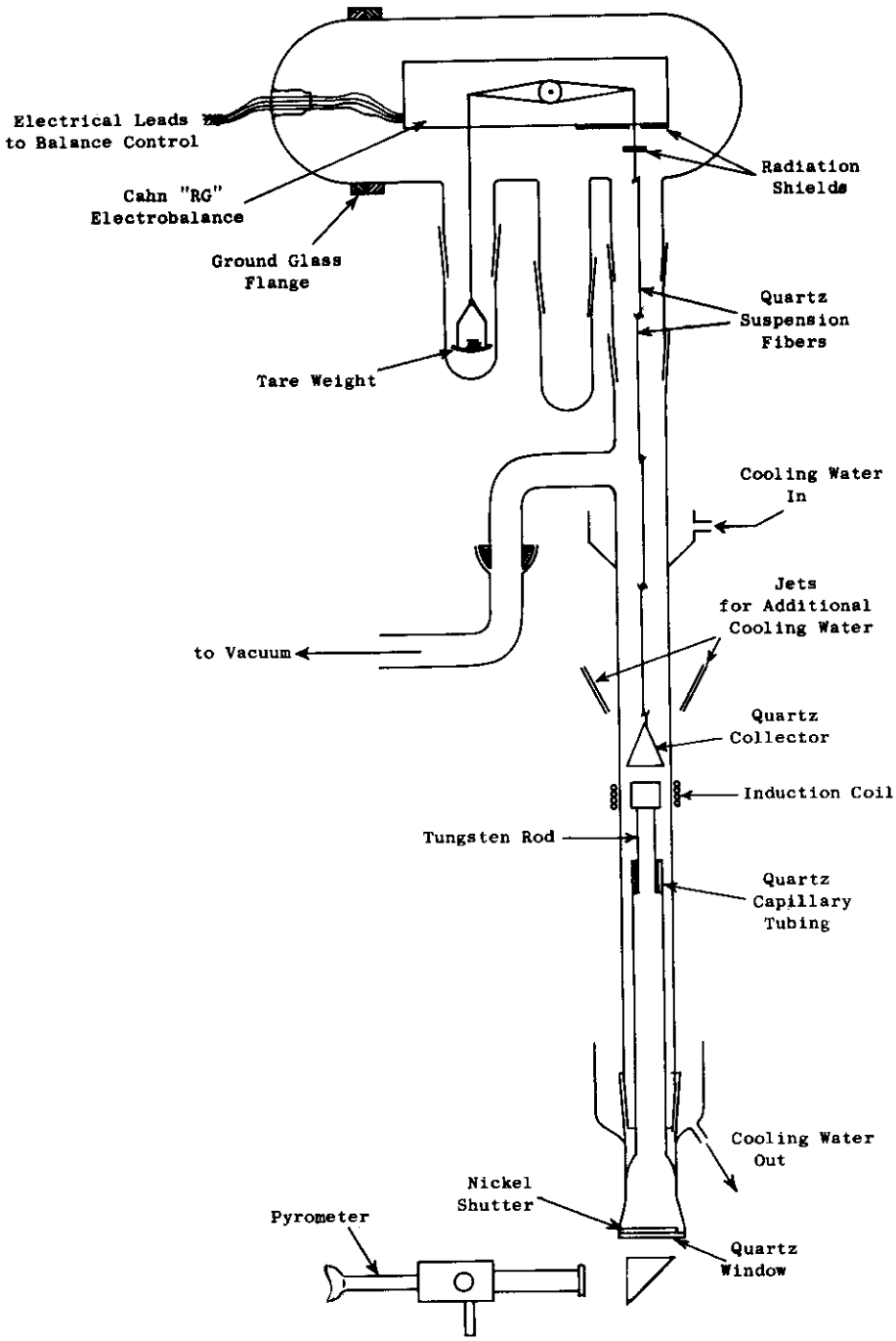

Figure 10. Schematic Diagram Of Microbalance System

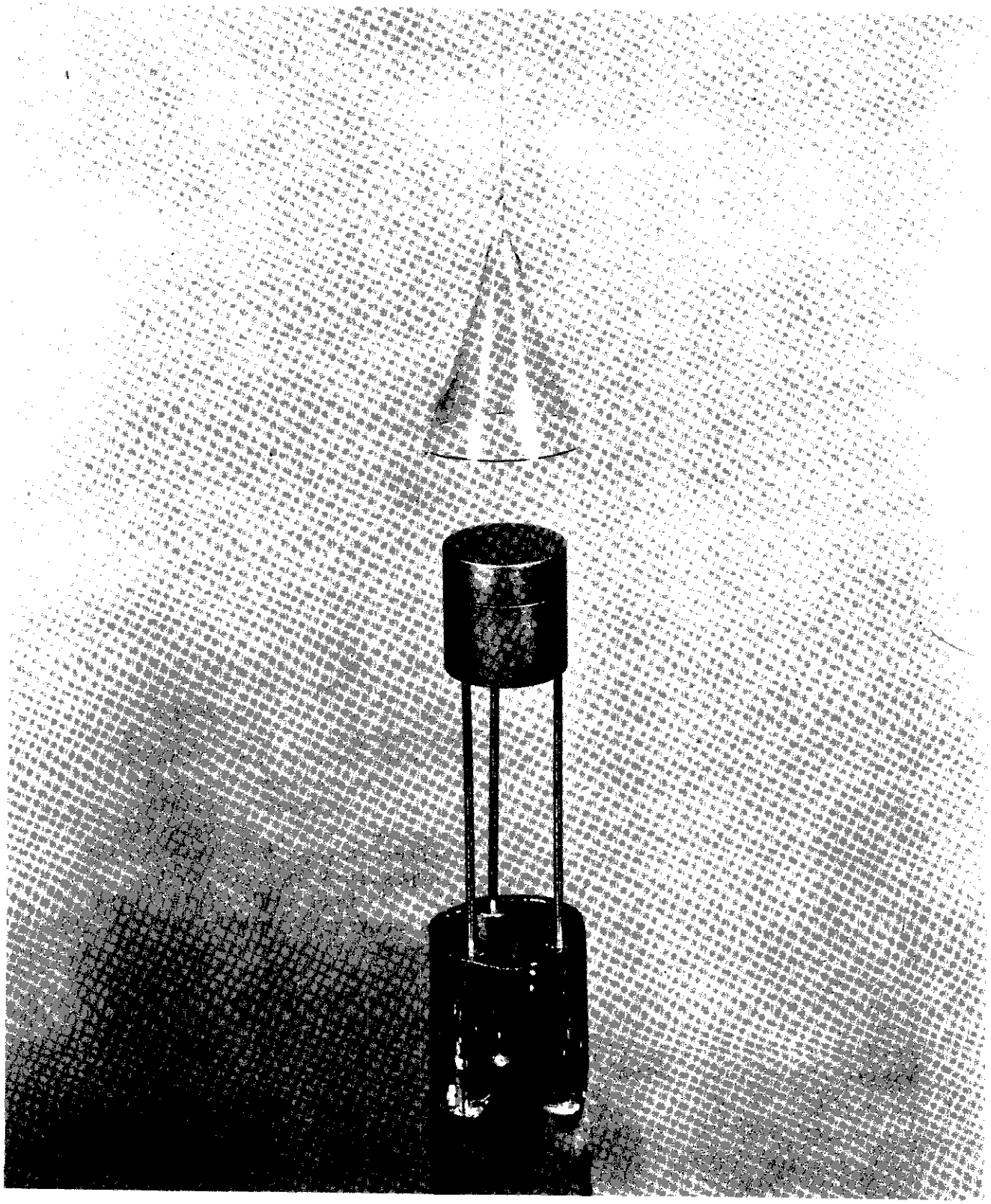

Figure 11. Effusion Cell And Collector Cone Assembly

A circular shield of tungsten sheet 0.005-inch thick rested on top of the effusion cell. This shield was slotted to reduce inductive heating and had a circular hole in its center placed concentric with the orifice. This served both as a radiation shield to warm the top of the cell and thus prevent orifice clogging and also to reduce the rate at which tungsten sublimed from the cell and reached the collector. The shield was not in place when the Figure 11 photograph was taken.

The effusion cells were made of tungsten and their shape and dimensions were the same as for the nitride measurements[3]. The two halves were not welded together in the boride study, and the lower half contained a black body hole 0.030 inch diameter and 0.200 inch deep. The converging conical orifice with 45° half angle and dimensions as in this present study, has a Clausing-factor of 0.976 according to some recent calculations[12]. The angular distribution of effusate from the conical orifice deviates most from that of the ideal orifice at low angles and since material was collected only in the forward direction, we have assumed an ideal orifice for the present calculations; i.e., a Clausing factor of unity.

Figure 12 is a photograph of the apparatus. The microbalance control and the recorder are not shown, nor is the vacuum system which, to the left of the large stopcock was described in an earlier report[3].

Temperatures were measured using a Microoptical Pyrometer which sighted on a black body hole in the cell bottom through a prism and window as shown in Figure 10. For temperature calibration, the microbalance chamber was removed and the top of the furnace tube capped by a second optical window with prism. (The transmission of this window-prism combination was determined in separate measurements using a tungsten strip lamp.) A second optical pyrometer which had been calibrated at the National Bureau of Standards, was mounted so as to observe the cell orifice through the upper window and prism. With the working pyrometer in position to sight on the black body hole in the bottom of the cell, the true cell cavity temperature referenced to the indicated black body hole temperature was determined at a number of temperatures throughout the temperature range of the effusion measurements. With this procedure, the difference between the working pyrometer and the standard pyrometer, the transmission of the lower window prism combination and any difference between the actual cavity temperature and black body hole temperature were factored into a single calibration.

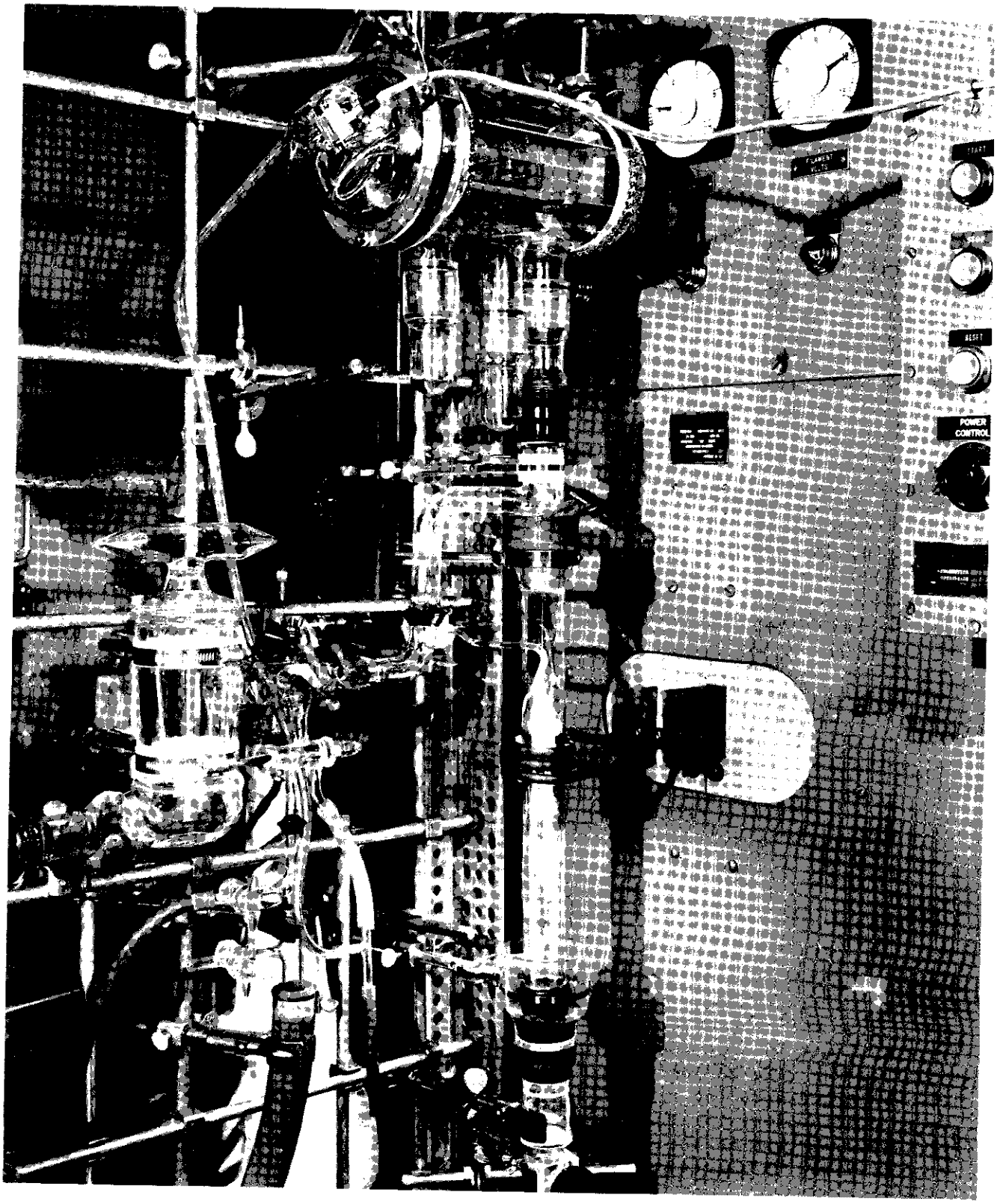

Figure 12. Microbalance System

Initially, with the microbalance in the system, considerable difficulty was encountered in obtaining a good vacuum. Apparently, the balance mechanism evolved considerable quantities of condensible vapors. However, after carefully removing all visible solder flux and several of the plastic connectors and gently heating the mechanism for prolonged periods under vacuum, the pressure was reduced to an acceptable level. Typical pressure readings during the measurements described here were between 1 x 10^{-7} and 5 x 10^{-7} torr while pressures as low as 4 x 10^{-8} torr had been obtained without the balance in the system. It might be noted that relatively severe balance fluctuations were experienced when system pressures were in the 10^{-6} range and the cell heated to high temperatures. This effect must be due, at least in part, to the fact that the collector blocked about 50% of the furnace tube area and could thus cause a sizeable pressure gradient. A pressure of 1 x 10^{-6} torr is equivalent to 7 micrograms force on the collectors used here. Such thermomolecular effects have been previously reported[13] in a system with similar geometry at a pressure of 3 x 10^{-6} torr.

In a typical measurement, the cell temperature was increased slowly to the test temperature in order to maintain the system pressure between 1 and 5 x 10^{-6} torr. After temperature and pressure conditions had stabilized, as indicated by pyrometer and vacuum gauge readings and by the linearity of the balance recorder trace, and after the pressure had fallen to the 10^{-7} torr range, the reading was begun and the temperature and pressure monitored while 30 to 100 micrograms of effusate was collected. A portion of a typical recorder trace of the collector weight gain is shown in Figure 13. The stability of the system and noise level of the balance output can be seen from this trace which shows a weight gain rate of 37.5 micrograms per hour. It should be noted that the weight reading of Figure 13 is not indicative of the total weight on the balance but only of the weight change.

The fraction of effusate collected f, was calculated from the expression

$$f = \frac{D^2}{D^2+4d^2} \qquad (1)$$

where d is the cell to collector distance and D is the collector diameter as shown in Figure 14. The distance d was measured by cathetometer with the cell heated to the temperature of the effusion measurements. There is some possibility of error in this measurement due to the fact that the collector might not be exactly centered over the cell, the collector open end may not be parallel to the plane of the orifice or to difficulties in accurately sighting on the various points due to the water curtain in the line of sight. The fraction of effusate collected was therefore measured by a second geometrical method. If R

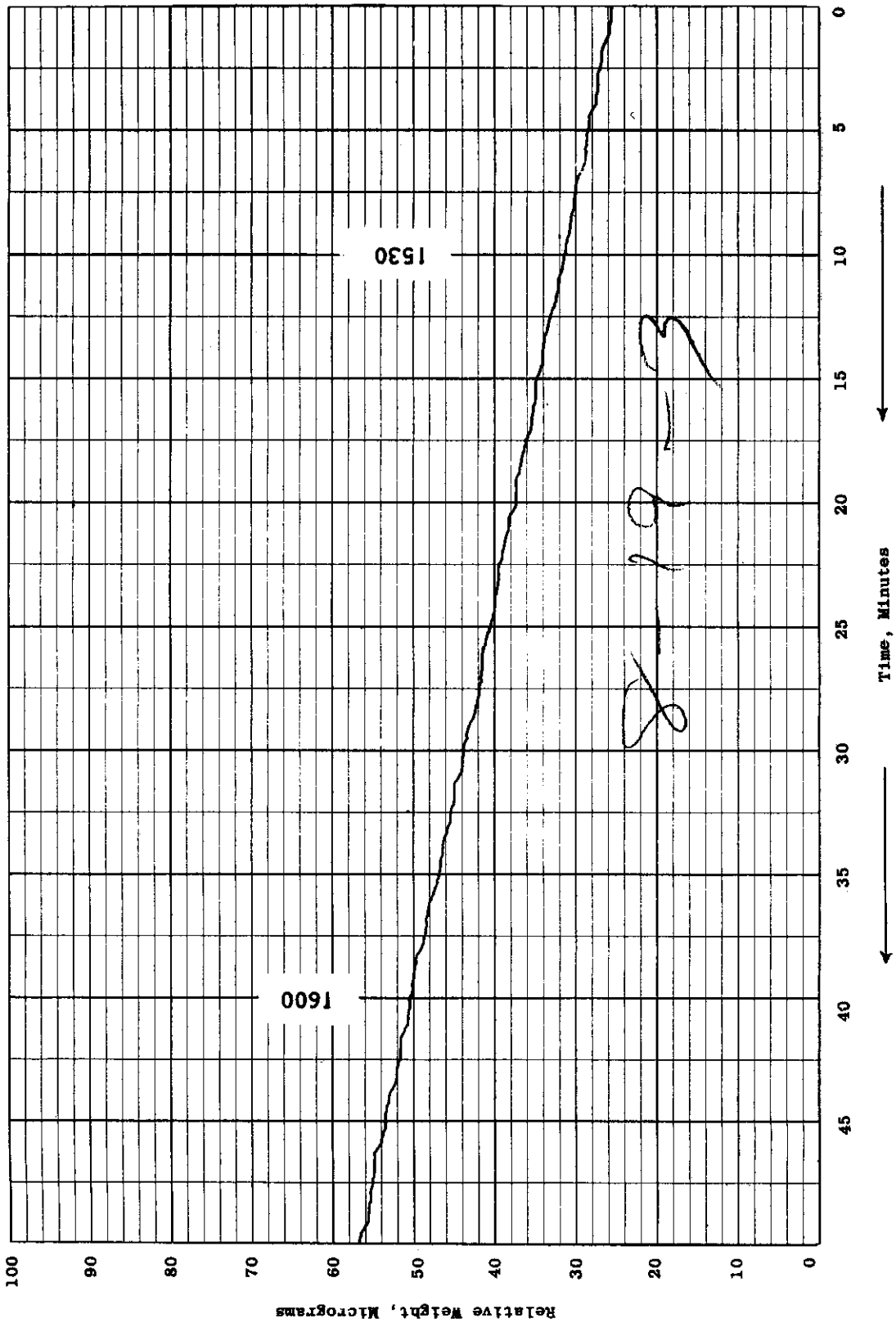

Figure 13. Typical Recorder Trace Of Microbalance Output

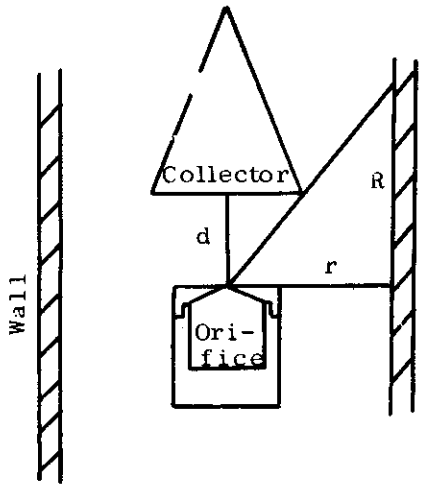

Figure 14. Cell-Collector Geometry

is the distance along the furnace tube from the top of the cell to the top of the condensed film on the furnace wall and r is the inner radius of the furnace tube, then

$$f = \frac{r^2}{r^2 + R^2} \qquad (2)$$

The distance R was also determined with the cell heated to the temperature of the effusion measurements. The two measurements of f were averaged and this value used for subsequent calculations. Generally good agreement was found between the two values.

Before any cell was used for effusion measurements, it was heated empty to temperatures above 2750°K for prolonged periods in order to vaporize impurities from the tungsten. Even after such treatment, it was found that appreciable collector weight gain rates were obtained from the empty cell at temperatures below 2500°K. Under the conditions of these measurements, the vaporization rate of tungsten should not be an important factor.

Two possible explanations for these "blank" rates of weight gain are suggested. The first is that impurities from the tungsten had not been completely eliminated by the high temperature heat treatment. Since the cells were quite massive (weighing about 90 grams), even if the total impurity level were reduced to 0.001%, the cell body would still contain 900 micrograms of impurities. Secondly, reactions of residual gases in the system with the cell or heat shield might cause transport of material which condenses on the collector. This could come about, for example, by the formation of volatile tungsten oxides or, if appreciable hydrocarbon vapor is present, by dissociation to form carbon vapor. This later possibility is suggested since, as has been noted above, the balance mechanism continuously evolves some kind of vapor into the system. This might be hydrocarbon vapor - possibly from plastic insulators.

Since these blank rates could not be reduced to a completely negligible level, the effusion data were corrected for this effect. A number of measurements were made of the collector weight gain rate from the empty cell to temperatures above 2750°K. On the assumption that the condensate originated at the top of the cell, the measured rate was divided by the fraction obtained from eq. 1 and this value was plotted against absolute temperature. It was found that at temperatures below 2600°K this plot approximated a straight line and thus all data below 2600°K were fit to a linear equation by the method of least squares. The plot of these data and the linear equation obtained are shown in Figure 15, which was used as a correction curve for the effusion data. For each effusion measurement, the blank rate was obtained from Figure 15 and subtracted from the measured effusion rate to give the corrected rate, due only to evaporation of material from

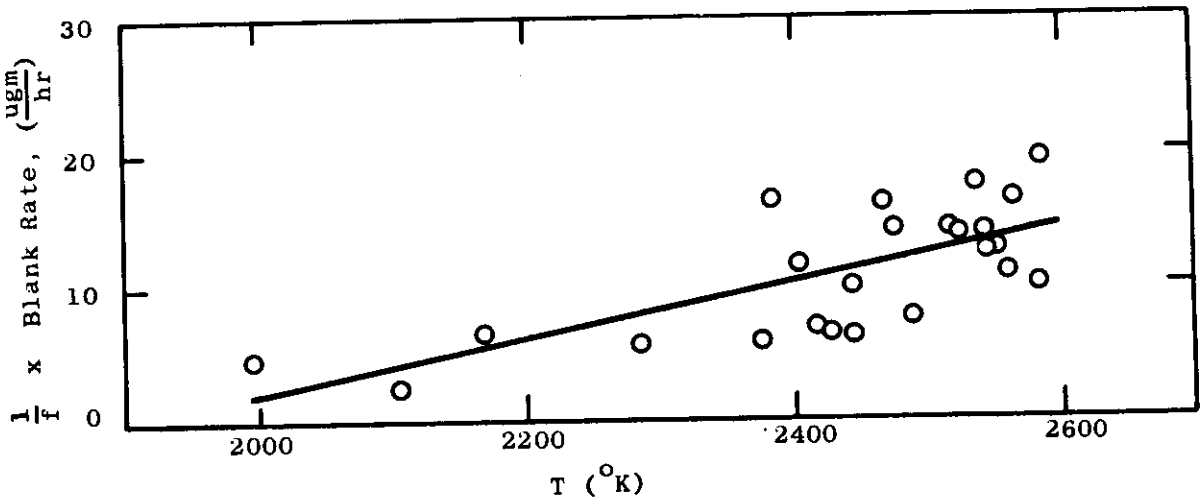

Figure 15. Correction Curve For Effusion Data

within the cell.

b. Description of measurements performed

The zirconium diboride used for these measurements was obtained from Mr. George Feick of Arthur D. Little, Inc. This material had been carefully prepared by zone refining[13a] and was of rather high purity. Analyses of similarly prepared material has been given in the A. D. Little reports[13a, b] and is shown in Table 8 where comparison is made with the results of analyses performed here on the sample supplied (Bar 79). The analytical methods used for our boron and zirconium analyses have been described by Kriege[14]; carbon analysis was obtained by combustion; O, N, and H by vacuum fusion; and other metals by qualitative spectrographic analysis. As may be seen in this table, the material used for this study contains significantly less boron than is considered typical of the A. D. Little zone refined ZrB_2.

Seven series of measurements have been performed in the present study. A summary of the conditions for each series of measurements is shown in Table 9. The material received from A. D. Little, ground to -100 mesh, was used for the first series. For this series rather high rates of collector weight gain were obtained, as compared to later measurements, and the rates decreased with increasing time at high temperature. The residual material from Series I was used for the second series of measurements. Similarly high rates, especially at lower temperatures, were obtained in this series. The material in the cell was analyzed after this series and the boron to zirconium atom ratio found to have increased about .03. This indicated the congruently vaporizing composition to be richer in boron; and so elemental boron (Fairmount Chemical Company 99% B) was added to the original A. D. Little sample sufficient to make the boron to zirconium atom ratio 1.96. For this purpose 0.01086 gm of powdered boron was added to 2.0000 gm of the powdered bar 79 material and thoroughly mixed. The mixture so formed was placed in an effusion cell and heated for prolonged periods to react the constituents. During the course of this treatment the Series III measurements were made. Again high rates of collector weight gain were noted and subsequent analysis of the material showed a decrease of 0.01 in the atom ratio during the course of this series. The Series IV measurements continued using the material from the Series III treatment. Once again, high rates of collector weight gain were obtained. The Series V, VI, and VII measurements were then made in each case using the material remaining from the previous series. In these last three series, collector weight gain rates were quite reproducible and in all three series, had the same temperature dependence. Final analysis after the Series VII measurements showed a boron to zirconium atom ratio 1.929. The results of these last three series of measurements are taken as representative of the evaporation rate of zirconium diboride at the congruently vaporizing composition

TABLE 8

ANALYSES OF A. D. LITTLE ZONE REFINED ZrB_2

Element	"Typical" Analysis (13 a, b.)	G.E. Analysis Bar 79
B	18.92 wt. %	18.32 wt. %
Zr	80.20 wt. %	81.13 wt. %
C	220 ppm	406 ppm
O	52	102
N	134	46
H	1.52	8
Mg	10-100	
Al	10-100	
Si	100-1000	trace
Cu	10	trace
Ti	10	trace
V	10	
Cr	10	
Mn	10	trace
Fe	100	trace
Ag	10	
Hf	100	
Sn		trace
Total	99.25%	99.51%
B/Zr atom ratio	1.989	1.904

TABLE 9

EXPERIMENTAL CONDITIONS FOR ZrB_2 EFFUSION MEASUREMENTS

Series	Initial Material	B/Zr Atom Ratio Initial	B/Zr Atom Ratio Final	Total Collector Wt. Gain (mgm)	Fraction Collected f	Total Collector Wt. Loss (mgm) Calc.	Total Collector Wt. Loss (mgm) Meas.
I	A. D. Little Bar 79	1.904	-	3.673	.428	8.58	8.55
II	From Series I	-	1.932	1.576	.353	4.46	3.29
III	Bar 79 + B	1.960	1.950	1.665	.213	7.81	12.47
IV	From Series III	1.950	-	1.407	.705	2.00	2.27
V	From Series IV	-	-	1.645	.465	3.54	3.90
VI	From Series V	-	-	0.713	.410	1.74	1.70
VII	From Series VI	-	1.929	1.200	.499	2.40	2.53

and only these results are used in the subsequent calculations. Discrepancies in the other four series are attributed to vaporization of impurities from the sample and to non-congruent evaporization.

The congruently vaporizing composition is found to have a 1.931 B/Zr atom ratio by averaging the final analyses of Series II and Series VII. Note that this composition was approached from compositions both deficient in boron (Series I and II) and richer in boron (Series III thru VII). It should be pointed out that accuracy with which the congruently vaporizing composition is determined is very sensitive to the accuracy of the individual analyses. Kriege[14] has indicated that the precisions of the zirconium and boron analyses are respectively 0.21 and 0.42 percent of the element analyzed with no criterion of the accuracy given. If the accuracy of each analysis is estimated to be 0.5% of the element, the accuracy of the elemental ratio would be 1% giving the congruently vaporizing composition as 1.931 ± 0.02 atom ratio boron to zirconium. The final analyses of Series II and Series VII (Table 9) are thus the same within both the accuracy and precision of the measurement.

In Column 5 and 6 of Table 9, the total collector weight gain and the fraction collected are shown for each series. From these two values, the total weight loss of material from the cell may be calculated. This total weight loss is shown in column 7. In column 8, the total cell weight loss as determined by direct weighings before and after each series is given. Comparison of these two values (columns 7 and 8) for each series shows fairly good agreement except for Series II and III. Again, it should be mentioned that the total weight of the cell is about 90 grams and thus a discrepancy of 0.1 mgm in total cell weight is but one part in 10^6. The generally good agreement between the measured and calculated cell weight loss is an indication that complete condensation of effusate was obtained at the collector. However, the measured loss should actually be a bit larger than the calculated value because of the small amount of tungsten evaporated from the cell body which does not reach the collector. Comparisons of columns 7 and 8 show this tendency. (Of course this would be the case also if complete condensation had not occurred.)

c. Experimental Results and Thermodynamic Calculations

The experimental results and thermodynamic calculations for the final three series of measurements are shown in Table 10. In the data reduction, the rate of collector weight gain in micrograms per hour was obtained directly from the recorder chart. This rate was corrected for the weight gain rate of the empty cell as explained in the above text and the corrected weight gain rate, w, in micrograms per hour, was then used to calculate the total evaporation rate, m, in $\frac{gm}{cm^2\ sec}$ from the expression:

$$m = \frac{w}{f\ a \times 3.6 \times 10^9} \tag{3}$$

where f is the fraction collected and a is the orifice area (cm^2) measured at room temperature and corrected for thermal expansion. The evaporation rate so calculated is given in column 2 of Table 10.

Assuming that for the last three series of measurements, the atom ratio of boron to zirconium in the effusate was constant at the congruently vaporizing composition (1.931), the evaporation rate of zirconium is found to be:

$$m_{Zr} = 0.8137\ m \tag{4}$$

Since the Clausing factor for the orifice has been shown to be very close to unity, the zirconium pressure may be found from the ideal Knudsen equation which, for the present conditions, becomes:

$$P_K\ (Zr) = 1.922 \times 10^{-3}\ m\sqrt{T} \tag{5}$$

where P_K is the zirconium pressure in atmospheres.

The logarithm of $P_K(Zr)$ calculated from equation (5) is given in column 3 of Table 10 and in Figure 16 is plotted against reciprocal temperature for the three series of measurements. Figure 16 shows the definite trend toward higher pressures with decreasing orifice area which indicates a non-unit evaporation coefficient.

The equilibrium pressure may be calculated using the treatment of Motzfeldt[15] in which the equilibrium pressure, P_E, is obtained from the expression:

$$P_E = \left[1 + \frac{W_o a}{A}\left(\frac{1}{\alpha} + \frac{1}{W_A} - 2\right)\right] P_K \tag{6}$$

where W_o is the Clausing factor for the orifice, A is the evaporation area of the sample, α the evaporation coefficient, and W_A the Clausing factor for the cell. For the present purposes, W_o, A, α , and W_A are the same for all cells used. Thus, we let

$$g = \frac{W_o}{A}\left(\frac{1}{\alpha} + \frac{1}{W_A} - 2\right) \tag{7}$$

and substitute into equation 6 to find:

$$P_E = (1 + ga)\ P_K \tag{8}$$

equation 8 may be rearranged to obtain:

TABLE 10

EFFUSION DATA AND THERMODYNAMIC CALCULATIONS FOR THE REACTION:

$$Zr\,B_{1.931(s)} \rightarrow Zr_{(g)} + 1.931\,B_{(g)}$$

T(°K)	$m\left(\frac{gm}{cm^2 sec}\right)$	log P_K(Zr)	log P_E(Zr)	log P_E(B)	log K_p	(kcal/mole) ΔH°_{298} (vap)
	Series V: f = 0.465; a = 0.0564 cm^2; g = 14.26 cm^{-2}					
2260	9.5×10^{-8}	-8.061	-7.805	-7.982	-23.216	480.41
2286	1.77×10^{-7}	-7.788	-7.532	-7.709	-22.416	477.52
2294	1.94×10^{-7}	-7.747	-7.491	-7.668	-22.296	477.93
2313	2.56×10^{-7}	-7.625	-7.369	-7.546	-21.938	478.07
2322	2.61×10^{-7}	-7.616	-7.360	-7.537	-21.912	479.66
2337	4.37×10^{-7}	-7.391	-7.135	-7.312	-21.253	475.67
2357	5.36×10^{-7}	-7.301	-7.045	-7.222	-20.989	476.87
2379	7.55×10^{-7}	-7.150	-6.894	-7.071	-20.546	476.49
2394	7.21×10^{-7}	-7.169	-6.913	-7.090	-20.602	480.07
2413	1.05×10^{-6}	-7.004	-6.748	-6.925	-20.118	478.51
2430	1.44×10^{-6}	-6.866	-6.610	-6.787	-19.714	477.37
2445	1.55×10^{-6}	-6.833	-6.577	-6.754	-19.617	479.20
2469	2.03×10^{-6}	-6.712	-6.456	-6.633	-19.263	479.86
2491	2.88×10^{-6}	-6.559	-6.303	-6.480	-18.814	478.99
	Series VI: f = 0.410; a = 0.01015 cm^2; g = 14.26 cm^{-2}					
2370	8.87×10^{-7}	-7.081	-7.022	-7.199	-20.912	478.74
2385	1.05×10^{-6}	-7.006	-6.947	-7.124	-20.702	479.39
2405	1.45×10^{-6}	-6.863	-6.804	-6.981	-20.282	478.74
2432	1.87×10^{-6}	-6.752	-6.693	-6.870	-19.957	480.47
2444	2.63×10^{-6}	-6.602	-6.543	-6.720	-19.518	477.90
2454	2.92×10^{-6}	-6.556	-6.497	-6.674	-19.383	478.31
2454	2.89×10^{-6}	-6.561	-6.502	-6.679	-19.397	478.48
2476	3.81×10^{-6}	-6.439	-6.380	-6.557	-19.040	478.70
2493	4.67×10^{-6}	-6.349	-6.290	-6.467	-18.776	478.96
2504	5.22×10^{-6}	-6.299	-6.240	-6.417	-18.630	479.37
	Series VII: f = 0.499; a = 0.0202 cm^2; g = 14.26 cm^{-2}					
2313	3.89×10^{-7}	-7.444	-7.334	-7.511	-21.836	477.01
2319	4.93×10^{-7}	-7.341	-7.231	-7.408	-21.534	475.02
2336	6.26×10^{-7}	-7.236	-7.126	-7.303	-21.226	475.19
2356	7.72×10^{-7}	-7.143	-7.033	-7.210	-20.954	476.29
2371	9.18×10^{-7}	-7.066	-6.956	-7.133	-20.728	476.86
2372	7.22×10^{-7}	-7.170	-7.060	-7.237	-21.033	480.35
2387	1.08×10^{-6}	-6.996	-6.886	-7.063	-20.523	477.81
2404	1.16×10^{-6}	-6.963	-6.853	-7.030	-20.426	480.13
2417	1.82×10^{-6}	-6.764	-6.654	-6.831	-19.843	476.27
2437	2.30×10^{-6}	-6.661	-6.551	-6.728	-19.541	476.80
2441	2.33×10^{-6}	-6.656	-6.546	-6.723	-19.526	477.41
2460	3.31×10^{-6}	-6.500	-6.390	-6.567	-19.069	475.96
2481	4.30×10^{-6}	-6.385	-6.275	-6.452	-18.732	476.15
2500	4.38×10^{-6}	-6.376	-6.266	-6.443	-18.706	479.50
2502	5.04×10^{-6}	-6.314	-6.204	-6.381	-18.524	477.78

Average 478.06 $\pm$1.50

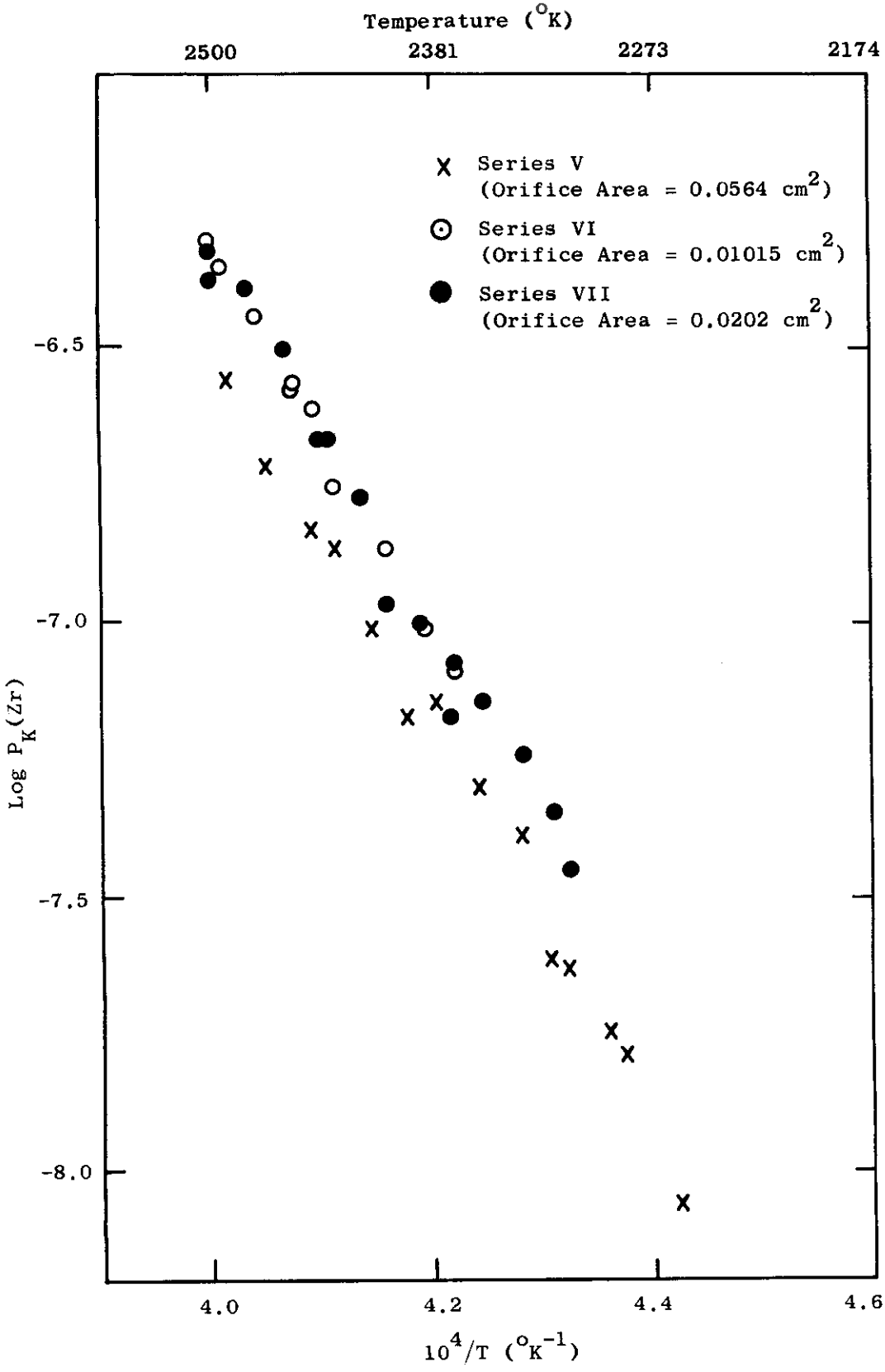

Figure 16. Log Zirconium Pressure Vs Reciprocal Temperature For ZrB_2

$$P_K = P_E - gaP_K \tag{9}$$

Using equation 9, P_K is plotted against aP_K which should give a straight line of slope g and intercept P_E.

For the present treatment, the log $P_K(Zr)$ vs $1/T$ data (Figure 16) was fit to a linear equation by the method of least squares treating each series separately. The following equations were obtained:

Series V $$\log P_K\,(Zr) = 7.488 - \frac{3.497 \times 10^4}{T} \tag{10}$$

Series VI $$\log P_K\,(Zr) = 7.965 - \frac{3.567 \times 10^4}{T} \tag{11}$$

Series VII $$\log P_K\,(Zr) = 7.294 - \frac{3.406 \times 10^4}{T} \tag{12}$$

Three values in the temperature range of overlap of the three series were chosen at $10^4/T = 4.0$, 4.1, and 4.2 and at each temperature, $P_K(Zr)$ was obtained from the least square line for each series and plotted vs $aP_K\,(Zr)$. Such a plot is shown in Figure 17 at T = 2500°K. The slope, g, and intercept $P_E\,(Zr)$, of the line were obtained by least squares treatment. Values of g obtained were 14.79, 14.33, and 13.67 cm^{-2} respectively at 2500, 2439, and 2381°K. The average of these three values g = 14.26 cm^{-2} was then used to correlate all data from the three series of measurements through the use of equation 8. The logarithm of the equilibrium pressure for zirconium, log $P_E(Zr)$, so obtained is given in column 4 of Table 10. Substituting g = 14.26 into equation 7, the evaporation coefficient $\alpha = .0983$ is obtained.

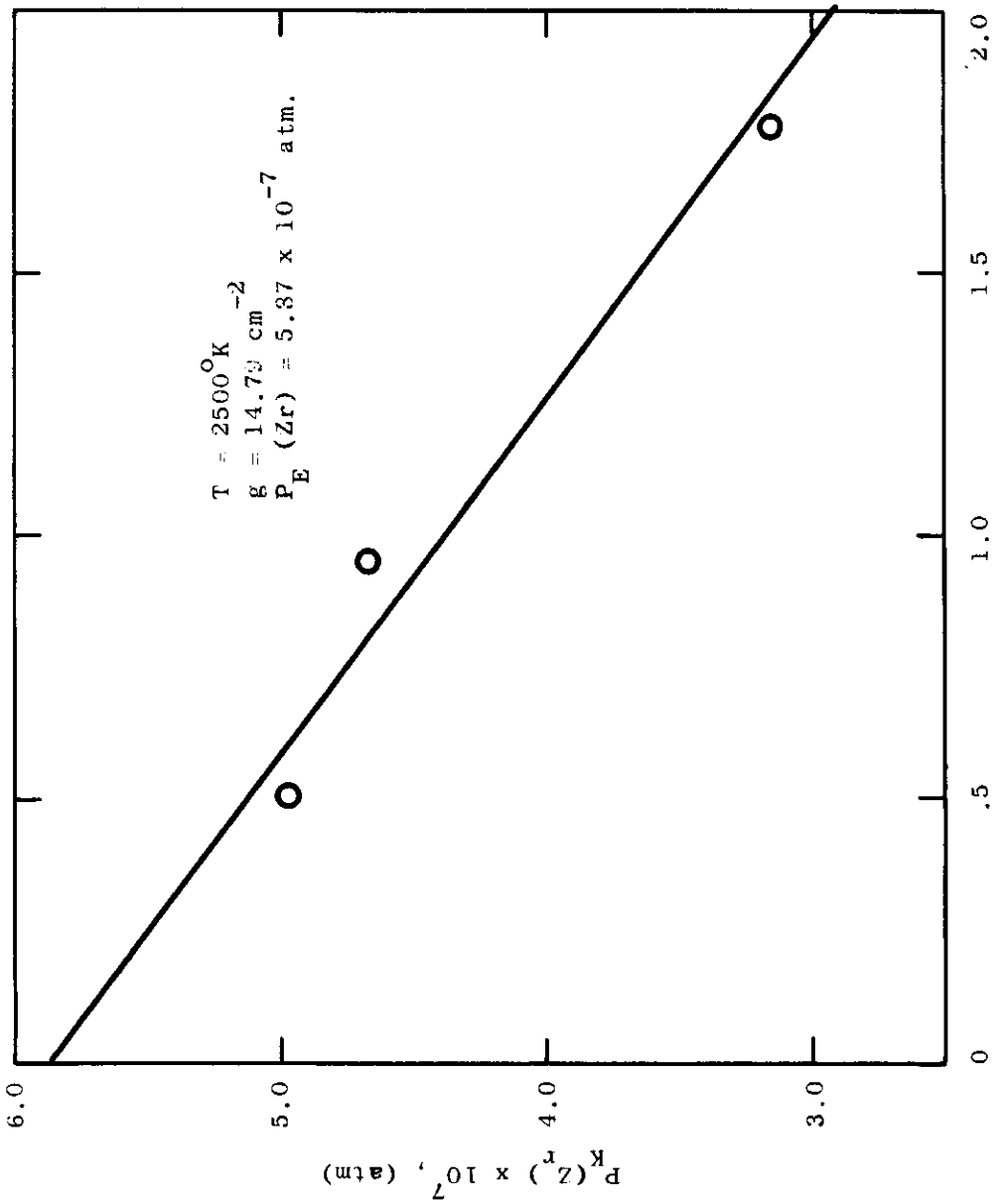

Figure 17. Motzfeldt Plot Of P_K

Again using the observation that the boron to zirconium atom ratio in the effusate is 1.931, the equilibrium boron pressure may be calculated from the relation:

$$P_E(B) = .665\ P_E(Zr) \qquad (13)$$

In column 5 of Table 10, the logarithm of the equilibrium boron pressure is given.

Having thus obtained the equilibrium pressures of the elements, related thermodynamic values for the reaction:

$$ZrB_{1.931} \rightarrow Zr(g) + 1.931\ B(g) \qquad (14)$$

may be obtained. The equilibrium constant for the above reaction is:

$$K_p = P_E(Zr)\ P_E\ (B)^{1.931} \qquad (15)$$

The logarithm of the equilibrium constant from equation 15 is given in column 6 of Table 10 and is plotted against reciprocal temperature in Figure 18. The line shown in Figure 18 is a linear fit of the data by the method of least squares. The equation for this line is:

$$\log K_p = 22.038 - \frac{10.164 \times 10^4}{T} \qquad (16)$$

Using this equation and the usual second law method one obtains $\Delta H^o_{2400}(vap) = 465.1$ kcal/mole as the enthalpy change for reaction 14 at temperatures near 2400°K. For comparison, the second law enthalpy may be calculated for each series of measurements from equations 10, 11, and

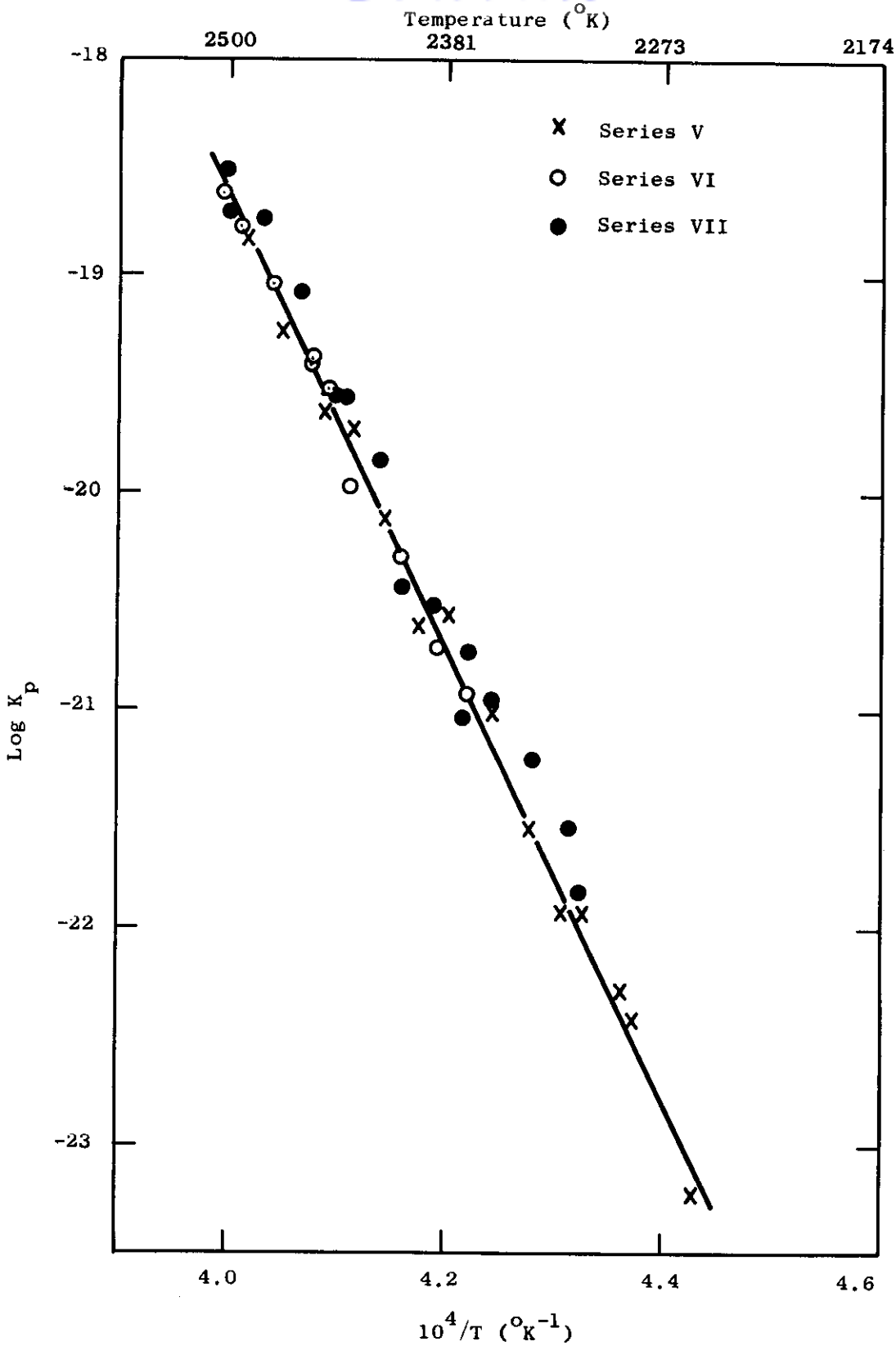

Figure 18. Log Equilibrium Constant Vs Reciprocal Temperature For $ZrB_{1.931}$ (s) → Zr(g) + 1.931 B (g)

12 giving $\Delta H^{o}_{2400}(vap)$ = 469.0, 478.3, and 456.8 kcal/mole for Series V, VI, and VII, respectively. There is no apparent trend in these three values with any of the experimental variables.

Finally, the enthalpy change for reaction 14 may be obtained by the third law treatment using the equation:

$$\frac{\Delta H^{o}_{298}\ (vap)}{T} = -R \ln K_p - \left(\frac{F^{o}_T - H^{o}_{298}}{T}\right)_{Zr(g)} - 1.931\left(\frac{F^{o}_T - H^{o}_{298}}{T}\right)_{B(g)} + \left(\frac{F^{o}_T - H_{298}}{T}\right)_{ZrB_{1.931}} \qquad (17)$$

The free energy functions $F^{o}_T - H^{o}_{298}/T$ for $Zr_{(g)}$ and $B_{(g)}$ have been obtained from the JANAF tables[16,b]. The free energy function for $ZrB_{1.931}$ has been approximated by subtracting 0.069 times the free energy function of solid boron from the free energy function of ZrB_2[16c]. The enthalpy change of reaction 14 at 298°K, ΔH^{o}_{298} (vap), obtained through use of equation 17 is given in the last column of Table 10. The resulting average third law enthalpy of vaporization is then ΔH^{o}_{298} (vap) = 478.1 ± 1.50 kcal/mole where the variation given is the standard deviation from the mean. The standard heat of formation of $B_{(g)}$ is 132.6[16b] kcal/mole and 145.4[16a] kcal per mole for $Zr_{(g)}$ which leads to a standard heat of formation of $ZrB_{1.931}$ of -76.6 at 298°K by the third law method. Similarly, the standard heat of formation of $ZrB_{1.931}$ at 298°K is -67.1 obtained by the second law method.

Errors in the determination of the heat of formation by the two methods may be estimated as follows: for third law calculation, an uncertainty of 0.5 kcal from the determination of P_K, 0.7 kcal from the determination of g and 2 kcal from the temperature measurement (± 10°K) is estimated. This gives a total uncertainty of ± 3.2 kcal in the third law heat of formation, which figure does not include errors in the auxiliary thermodynamic data. It may be shown that the value obtained for the heat of formation is rather insensitive to the composition of the congruently vaporizing substance. The heat of vaporization is, however, quite dependent on this determination.

For the second law calculation we estimate an uncertainty of ± 8 kcal from the variation obtained in the three series and an additional uncertainty of ± 3 kcal due to the empty cell weight

loss correction for a total uncertainty of ± 11 kcal in the second law result.

The final values for the heat of formation of $ZrB_{1.931}$ obtained in the effusion study are thus - 76.6 ± 3.2 kcal/mole from the third law calculation and - 67.1 ± 11 kcal from the second law determination.

d. Comparison with other determinations

A considerable amount of information exists on the thermodynamic properties of ZrB_2 and much work is in progress at the time of this writing. The recent JANAF Table[16c] gives a good summary of the information currently available and is used for the present comparisons.

The JANAF[16c] have adopted the value -71.2 ± 5 kcal/mole for the heat of formation of ZrB_2. This is based on a provisional report using fluorine bomb calorimetry on an A. D. Little zone refined sample. The third law heat (-76.6) obtained in the present study is 5.4 kcal/mole more negative than the value adopted by JANAF. It should, however, be pointed out that the value obtained in the present study is based on a heat of formation of B(g) of 132.6 kcal per mole[16b]. If one were to use a higher value, such as 135 kcal per mole preferred by some[13b], one would obtain -72.0 as the present result in quite good agreement with the value adopted by JANAF. On the other hand, heats of formation obtained from oxygen combustion are -76.7 ± 1.5 and -75.02 ± 3.25 kcal per mole[16c] in agreement with our -76.6 value.

Leitnaker, et al[17] used a Knudsen effusion technique to study the vaporization of ZrB_2. Their ideal Knudsen pressures of zirconium are in quite good agreement with the values obtained here. However, they report an evaporation coefficient of only 0.025, compared to 0.098 obtained here, which leads to higher equilibrium pressures and thus to their more positive heat of formation. Leitnaker et al, have revised their data[16c] and now report a congruently vaporizing composition of $ZrB_{1.967}$ and a heat of formation of -69.5 kcal per mole using JANAF auxiliary data.

Goldstein and Trulson[18] investigated ZrB_2 vaporization using a mass spectrometer and have reported -71.6 kcal per mole for the heat of formation. Complete details of this study are not available for comparison of congruently evaporating compositions and evaporation coefficients.

Heats of formation obtained by resonance line absorption (detailed later in this report) are -74.5 ± 1 and -75.6 ± ¼ kcal per mole.

C. Matrix Isolation Studies:

In the previous annual report[3], some results were given on the spectrum of ThO_2 in solid argon matrices and some tentative conclusions were drawn as to the vibrational assignment and structure of this molecule. During the past year, similar effort has been applied to the refractory oxides of zirconium and hafnium.

As Brewer had recently pointed out[19], there were no spectroscopic data available for any metal dioxide molecules. This research is believed to represent the first attempt to obtain such information. The matrix isolation technique has here been extended to materials that vaporize at temperatures as high as 2700°C and is possibly the only available technique capable of obtaining infrared spectra of very refractory materials. Although it is at present impossible to obtain a complete vibrational frequency assignment on the oxides of thorium, zirconium and hafnium from these measurements, nevertheless it is felt that the asymmetric stretching frequency for ThO_2 and ZrO_2 can be reliably assigned and various possibilities for the other fundamentals can be inferred. It is anticipated that, by using isotopically substituted oxides (viz. O^{18} enriched materials), complete assignments can be obtained.

During the past year, the only apparatus modifications were the use of cesium iodide optics (to extend the spectral range of the apparatus) and, in some cases, the use of iridium crucibles from which vaporization is carried out, the latter to minimize the reaction of the various oxides with the container. It has been possible to extend the optical range to approximately 40 microns under most conditions. The use of the iridium crucibles has been somewhat marginal, especially in the case of zirconia, since the working temperatures are limited by the melting point of iridium, 2450°C.

Several remarks are in order concerning the matrix isolation technique when used at very high temperatures. At extremely high temperatures ($>$ 2500°C), there is a tendency toward the appearance of spurious, non-reproducible, absorption bands of low intensity. For this reason, only bands which appear reproducible and sufficiently intense to be regarded as real and due to the molecule under consideration are reported here. The occurrence of these weak bands at the very high temperatures is not surprising. Undoubtedly there is a sufficient heat flux into the matrix to cause a softening with consequently sufficient mobility of the isolated molecules so that polymerization is possible. Furthermore, since oxygen is an important vaporization product of these refractory oxides, it is conceivable that oxidation of shield materials and dewar parts is possible and can result in some contamination of the matrix with these oxides.

Vaporization of the refractory oxides was carried out from either

tungsten or iridium cells having an orifice of approximately 2 mm. The iridium cell was so constructed as to fit inside of a tungsten cell which thus acted as a susceptor. The iridium cells were fabricated by Englehard Industries and were of welded construction with the effusion orifice being the only opening. Loading of these cells was accomplished through the orifice. A schematic of a typical iridium cell in a tungsten susceptor is given in Figure 19. Temperatures were read on a black body hole located in the base of the tungsten susceptors with a micro-optical pyrometer. All matrix gases were Matheson research grade materials. Prior to isolation, samples were thoroughly degassed in situ at temperatures slightly higher than those at which isolation was carried out. Nevertheless, traces of water were still evident in the resulting matrix isolated spectra and indeed it is well known that both thoria and zirconia tenaciously retain water. The presence of small amounts of both CO and CO_2 were also evident in the various spectra and were presumably due to carbon impurity in the Knudsen cells or to the presence of carbonate in the refractory oxides. All spectra were recorded with a Perkin Elmer Model 112 double pass spectrophotometer.

The results for thoria, zirconia and hafnia are given below.

1. Thoria

The infrared spectrum of thoria in solid argon matrices was reported previously. At that time, those frequencies due to ThO_2 and to ThO were given along with a tentative assignment based on a linear molecular configuration for ThO_2. These spectra are included in Figure 20 (Spectra A and C). During the course of this year's investigation, the spectrum in solid argon was re-examined using an iridium cell and also spectra in solid krypton and xenon were observed. These spectra are given as B, D and E of Figure 20. Unless otherwise noted, the containers used were tungsten. The temperature of vaporization, T_v, and the time of deposition, t_v, are also included in Figure 20. The ratio of matrix to trapped species was estimated to vary between 500:1 to 200:1. It is evident from Figure 20 that the spectrum obtained from the iridium cell shows no signs of the presence of ThO (877 cm^{-1} - 881 cm^{-1} in solid argon), this frequency being definitely established by vaporization of a mixture of Th and ThO_2 (Spectrum C). Apparently the amount of ThO in the vapor is greatly influenced by the tungsten crucible, however, the spectra show no evidence for any tungsten oxides and, except for the disappearance of ThO, the major bands are identical to the spectra obtained from tungsten cells. These major bands must be presumed to be due to ThO_2. The appearance of a very weak band at around 1030 cm^{-1} and the disappearance of the very weak band at 1311 cm^{-1} should be noted. More will be said about these bands when the results for ZrO_2 are given. The spectra obtained in solid krypton and solid xenon (D and E) show typical matrix shifts, the magnitude of which are quite reasonable. It is interesting to note that the weak

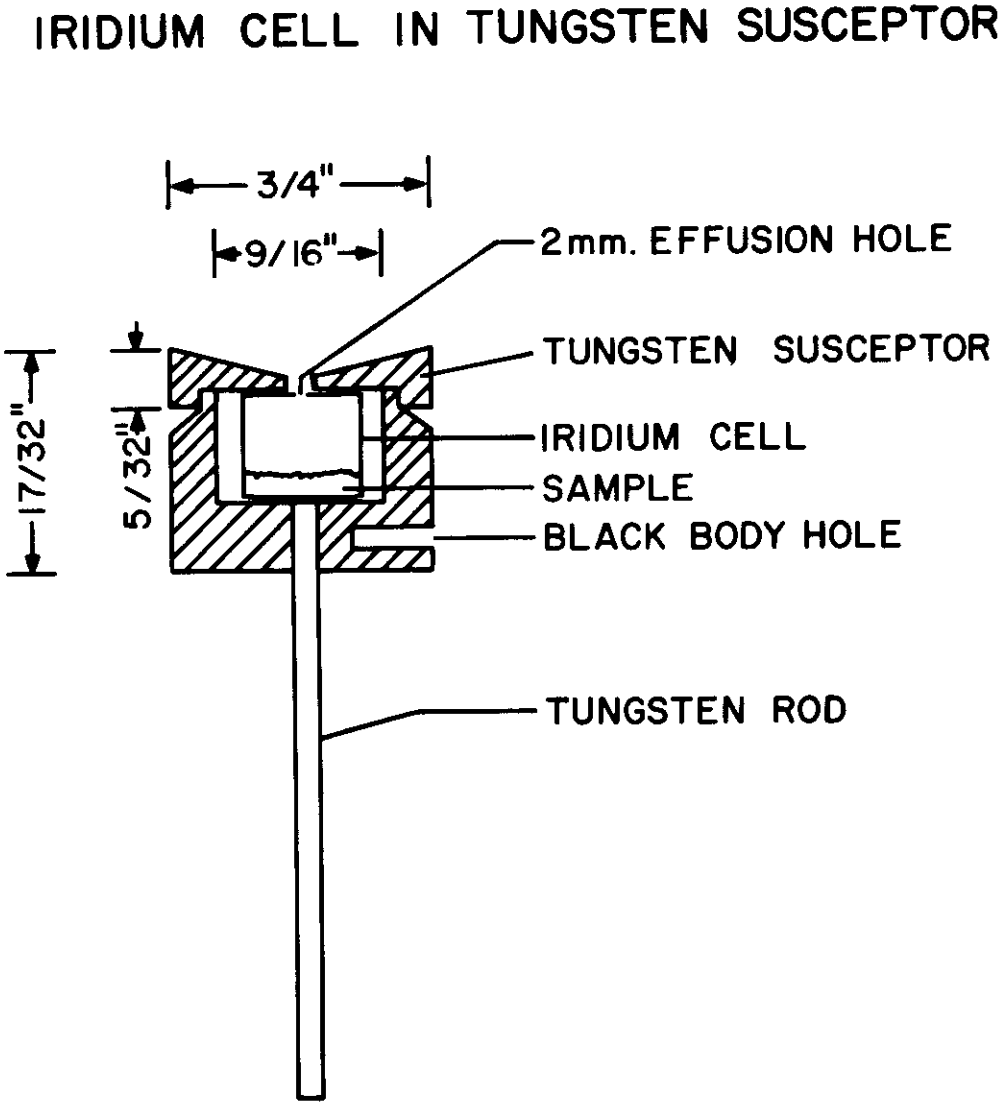

Figure 19. Iridium Cell In Tungsten Susceptor

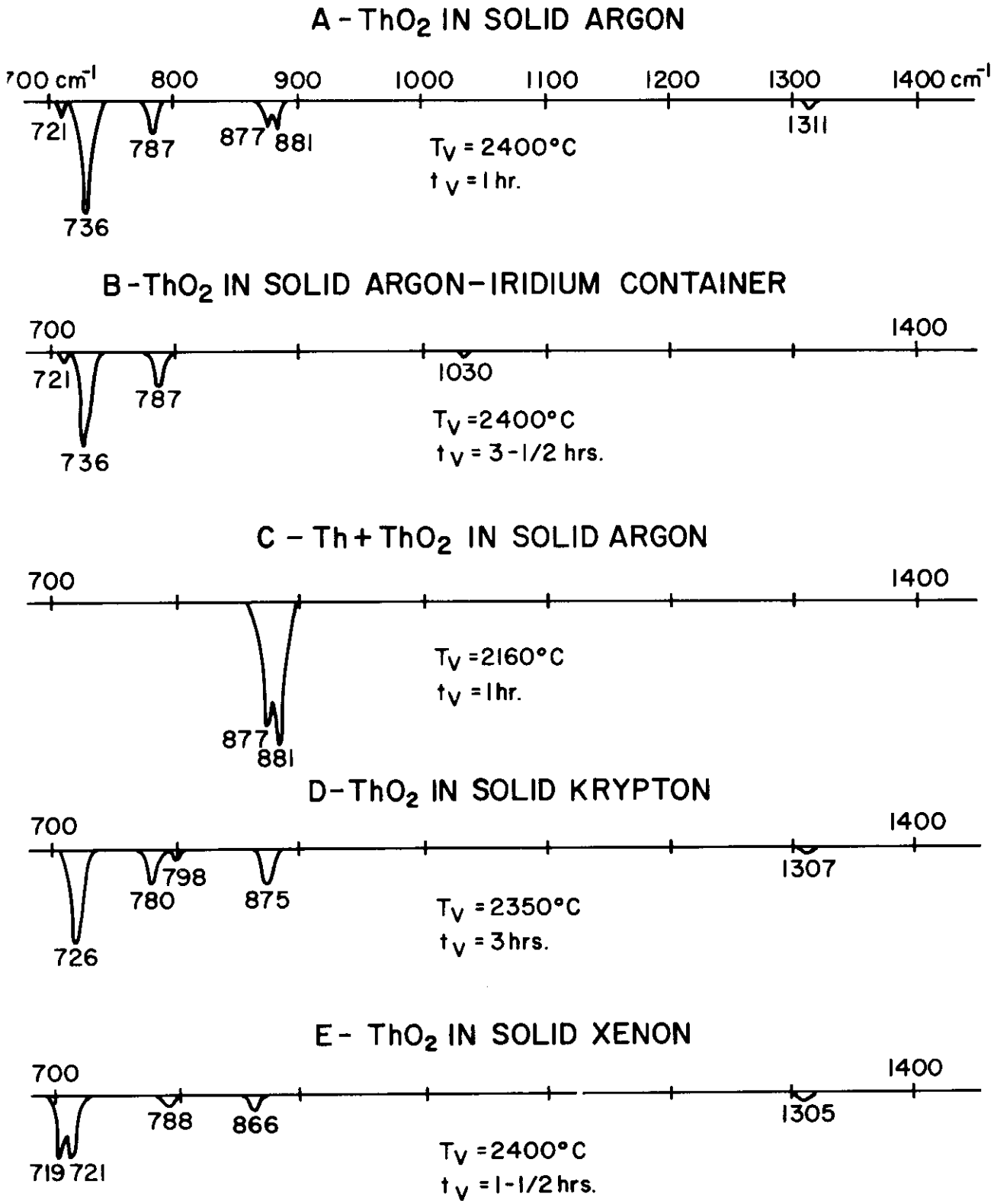

Figure 20. Spectra Of Matrix Isolated Vapors From Thoria

band at 722 cm^{-1} in solid argon does not have a counterpart in either solid krypton or solid xenon and for this reason might reasonably be regarded as a so-called matrix effect, peculiar to argon. The spectrum obtained in solid xenon shows peaks which are much broader, and in one case split (719 cm^{-1}, 721 cm^{-1}), indicating possible multi-site matrix effects.

In general, the spectra are quite simple, with only one strong peak (736 cm^{-1} in A) and one weak peak (approximately 787 cm^{-1} in argon, assignable to the ThO_2 molecule. The frequency around 880 cm^{-1} in argon must be assigned to ThO based on the spectrum obtained from the mixture of Th and ThO_2. Regardless of whether the molecule is bent or linear, the strong peak (736 cm^{-1} in A) for ThO_2 is undoubtedly due to the asymmetric stretching frequency ν_3, since in either configuration this mode should give rise to the most intense fundamental. Assuming a linear configuration, point group $D_{\infty h}$, two fundamental frequencies should be active. These are ν_3 and ν_2 (the bending mode), whereas ν_1, the symmetric stretching frequency is inactive. Unfortunately, the frequency ν_2 is most likely beyond the spectral range of our measurements ($> 40\,\mu$) and is, therefore, not observable. Using the equations for the linearly symmetric XY_2 valence force model, as given in Herzberg[20], the fundamental ν_3 (736 cm^{-1} in A) gives a stretching force constant, $k_1 = 4.49 \times 10^5$ dyne/cm. With this constant and the above mentioned equations, ν_1 is estimated to lie around 680 cm^{-1}. If the frequency at 787 cm^{-1} in solid argon is due to a combination of $\nu_1 + \nu_2$ (active in $D_{\infty h}$), ν_2 must then lie around 110 cm^{-1}. Further credence to this assignment can be added by estimating ν_2 by a comparison with the CO_2 molecule. In CO_2, the ratio of the bending force constant, $k\delta / \ell^2$, to the stretching constant, k_1, is equal to .0336[19]. Using this ratio, a bending constant for ThO_2 of around .15 x 10^5 dyne/cm is obtained which yields a value for the bending frequency, ν_2, of about 135 cm^{-1}. Considering the nature of this calculation, this is in good agreement with the 110 cm^{-1} value obtained from the combination band. On the other hand, if the molecule is bent (point group C_{2v}), all three fundamentals are active and the band at 787 cm^{-1} can conceivably be due to ν_2. However, until further spectra on isotopically substituted materials are obtained, such as the use of O^{18} enriched ThO_2, and the measurement of the resulting isotopic shifts of the observed frequencies, more definite conclusions about the configuration and frequency assignment for this molecule will be deferred.

2. Zirconia

Matrix isolation of the vapors in equilibrium with zirconia was conducted in solid argon and solid krypton. Both tungsten and iridium cells were used as containers for the zirconia. The zirconia powder was obtained from the Zirconium Corporation of America, grade A-H, and had a purity of better than 99.9%. Vapors from a mixture of

Zr and ZrO_2 were also isolated in solid argon. Typical infrared spectra are given in Figure 21. The use of iridium cells proved to be somewhat marginal as containers for zirconia since it was found that temperatures in excess of the melting point of iridium were necessary to obtain reasonably intense spectra. Therefore, the zirconia spectra obtained in iridium cells are in general much weaker than those obtained in tungsten. Except for two bands at around 1850 cm^{-1}, the infrared spectrum of zirconia (e.g. spectrum A, Figure 21) bears a close resemblance as far as relative distribution and intensity of the peaks are concerned, to that of thoria. This suggests that ZrO_2 is quite similar in structure and bonding to ThO_2. The spectrum obtained from the mixture of Zr and ZrO_2 is particularly noteworthy. In this case, the most intense peak, 960 cm^{-1} (spectrum C) is undoubtedly due to ZrO since, in the presence of the metal, ZrO should be the major product of vaporization. One suggested ground state configuration for ZrO[21] is $^3\Delta$ with a vibrational frequency of 936 cm^{-1}. Since, in general, matrix shifts are towards longer wave lengths, the observed frequency of 960 cm^{-1} appears to be inconsistent with the reported value of 936 cm^{-1} for the vibrational frequency of the ground state. (It is, of course, possible in the case of sizeable molecules to have matrix shifts towards shorter wave lengths which would account for the apparent discrepancy.) It is, however, consistent with an alternate suggestion[22] that the ground state configuration for ZrO is $^1\Sigma$ with a measured vibrational constant of 978 cm^{-1}, and that the $^3\Delta$ state is a very low lying excited state. In fact a weak frequency at 925 cm^{-1} in solid argon and a stronger frequency at 913 cm^{-1} (spectrum D) in solid krypton, also observed, it may conceivably belong to the $^3\Delta$ configuration (vibrational frequency 936 cm^{-1}). That the $^1\Sigma$ state is the ground state of the molecule is consistent with the fact that the 960 cm^{-1} band is by far the most intense one. While this explanation would demand that the population of $^3\Delta$ state is somehow frozen into the matrix at the low matrix temperature similar effects have been observed before in the matrix isolation of BO_2[23]. Thus indications are that the ground electronic configuration for ZrO is $^1\Sigma$ rather than $^3\Delta$, but other interpretations are not completely ruled out.

Similar to the case of thoria, the spectra obtained using iridium cells (spectra B and E) show no signs of the ZrO vibrational frequency. Apparently there is also an enhancement of ZrO when vaporization is carried out from tungsten cells. There is little doubt that the frequency at 818.7 cm^{-1} in argon and its counterpart at 810 cm^{-1} in krypton belong to the ZrO_2 molecule. The weak frequency at 884 cm^{-1} in argon and 878 cm^{-1} in krypton likewise can be assigned to ZrO_2. This frequency is only evident in the spectra obtained from tungsten and is lacking in the spectra from iridium cells. However, the iridium spectra are quite weak; the matrix may be so dilute that this frequency is not observable. A new, rather strong, band appears at around 1035 - 1041 cm^{-1} in solid argon (spectrum B) and at 1036 cm^{-1} (spectrum E)

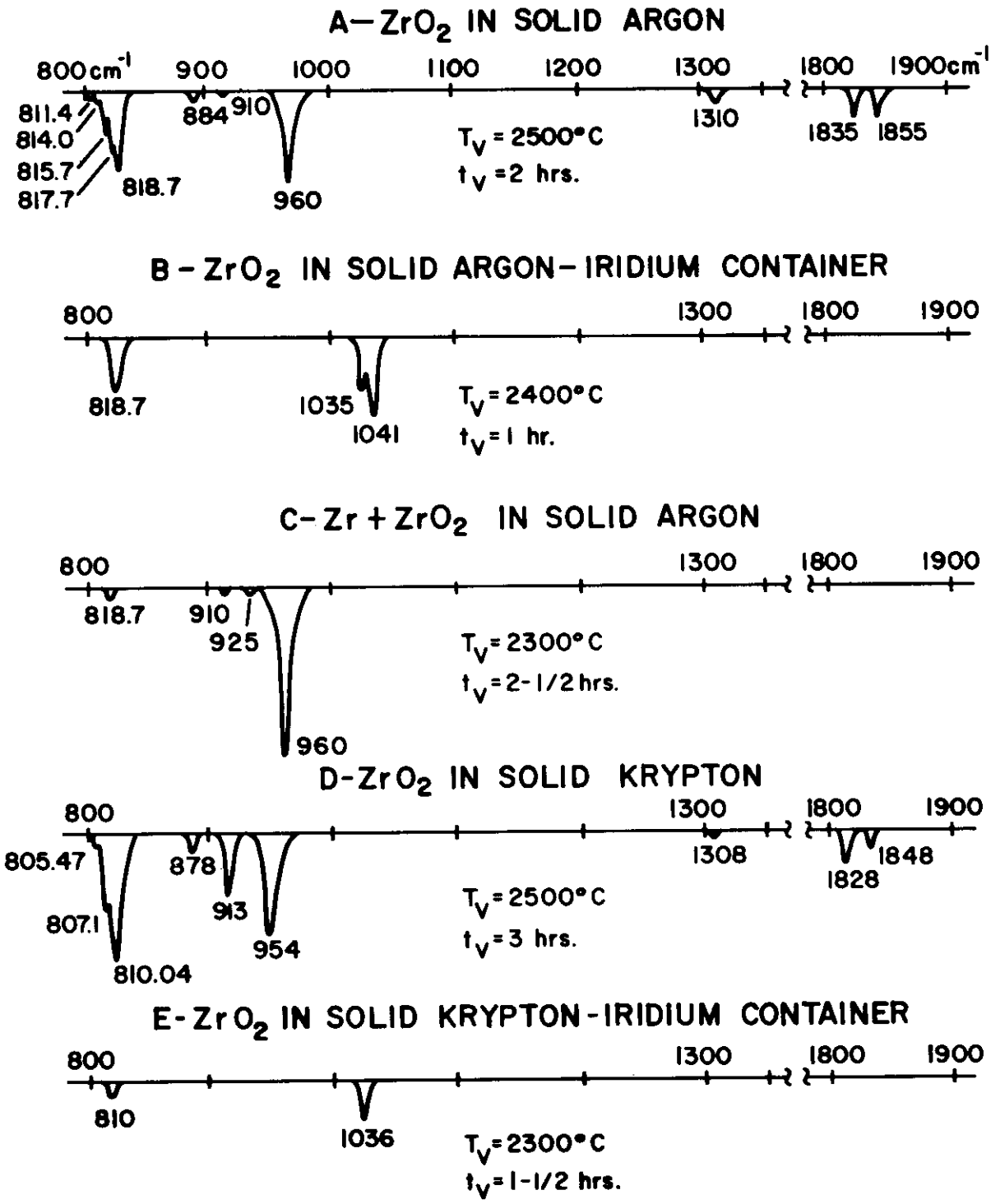

Figure 21. Spectra Of Matrix Isolated Vapors From Zirconia

using iridium containers. It is very unlikely that this feature is due to ZrO_2 since it is not seen in the other spectra. It is possible that this feature is due to some iridium oxygen compound; however, the instability of iridium oxide makes its presence unlikely at temperatures of vaporization. An alternate explanation which appears to be more plausible is that these frequencies are due to the presence of ozone in the matrix. A very intense fundamental for gaseous ozone[20] lies at 1043 cm^{-1} and would be expected to shift towards longer frequencies in the matrix. A great deal of oxygen is presumably evolved when zirconia is vaporized and it is possible that this oxygen, when trapped in the matrix and simultaneously subjected to the rather large radiant flux from the hot Knudsen cell, can undergo a reaction to form a significant amount of ozone. In any case, these frequencies can not be assigned to the ZrO_2 molecule. A similar frequency was reported, although much weaker in intensity, in the spectrum of thoria contained in an iridium crucible. The frequencies in Figure 21 around 1300 cm^{-1} (1311 cm^{-1} in argon spectrum A) do not appear to be due to ZrO_2 since these frequencies, as mentioned previously, are also present in the spectra obtained from the thoria vaporization. It appears then that only the frequencies at 818.7 cm^{-1} and that at 884 cm^{-1} (both in solid argon) and their counterparts in solid krypton are assignable to the ZrO_2 molecule. These are quite analogous to the ThO_2 frequencies, both in intensity and in relative wave length. Therefore, proceeding similarly to the ThO_2 case, the lower frequency is assigned to the asymmetric stretch, ν_3. Again using a linear configuration, a stretching force constant, $k_1 = 4.65 \times 10^5$ dyne/cm. is obtained. This leads to a value of about 700 cm^{-1} for the symmetric stretch, ν_1. If the frequency at 884 cm^{-1} is again assumed to be due to $\nu_1 + \nu_2$ around 184 cm^{-1} is obtained. Using the ratio obtained from CO_2 for $k\delta / \ell^2$: $k_1 = .0336$, the bending constant for ZrO_2 is equal to .156 x 10^5 dyne/cm. and leads to a value of around 150 cm^{-1} for ν_2. Again it seems that the agreement is satisfactory. Further proof of the linearity of ZrO_2 is suggested by the structure of the 818 cm^{-1} fundamental. Under the best resolution attainable in our experimental setup (approximately 1.5 cm^{-1}), four shoulders are just discernable on the low frequency side of the 818 cm^{-1} peak. Five naturally abundant isotopes are present in zirconium; these have masses 90, 91, 92,94, and 96 and relative abundances of 51.5%, 11.2%, 17.1%, 17.4% and 2.8% respectively. It seems plausible to assign the five observed peaks, 818.7 cm^{-1}, 817.7 cm^{-1}, 815.7 cm^{-1}, 814.0 cm^{-1} and 811.4 cm^{-1} to ν_3 of each of the isotopic ZrO_2 molecules. Admittedly, because of the rather poor resolution, it is difficult to obtain good peak frequencies for these bands. Nevertheless, some indication of the O-ZrO angle can be deduced from these frequencies using the usual equations for the frequency ratio for an isotopically substituted XY_2 molecule. The ratio for any two frequencies is given by[20]:

$$\frac{\nu\ 3}{\nu\ 3'} = \left(\frac{1 + \frac{32}{m_x} \sin \alpha}{1 + \frac{32}{m_x'} \sin \alpha} \right)^{1/2} \qquad (18)$$

where m_x and m_x' are the atomic weights of any two zirconium isotopes and α is one-half the apex angle.

Using the observed frequencies, an apex angle around 180° fits the data satisfactorily. These bands should be re-examined under high resolution so that a more precise calculation can be carried out.

The bands around 1850 cm^{-1} can only be accounted for as being due to some impurity or to low lying electronic transitions in ZrO_2. Their assignment to combinations or overtones in ZrO_2 does not seem to be likely.

Again, more definite conclusions concerning the frequency assignment and structure of ZrO_2 should be possible with the use of O^{18} isotopically enriched material.

3. Hafnia

A sample of hafnia of better than 97% HfO_2 was obtained from the Zirconium Corporation of America, the major impurity being ZrO_2. Vaporization was carried out from tungsten cells on hafnia and a mixture of hafnia and hafnium metal. The resulting infrared spectra of the vaporization products in solid argon, krypton and xenon are given in Figure 22. Except for a band at 810 cm^{-1} in solid krypton, assignable to ZrO_2, only a single feature appears in all the spectra. This feature (960 cm^{-1} - 952 cm^{-1}) must be assigned to the HfO molecule since it is present in the spectrum obtained under reducing conditions (Hf + HfO_2). It should be noted that the HfO and ZrO frequencies are very close and indeed are within several wave numbers of each other. This is somewhat unexpected in view of the fact that HfO is heavier and larger than ZrO. It is conceivable that the matrix shift in HfO is towards shorter wave lengths since this molecule is quite large and thus the observed matrix frequency of HfO lies close to that for ZrO. Again, it is seen (spectrum D Figure 22) that the xenon matrix gives a much broader appearing band.

No evidence for the HfO_2 molecule was found in the matrix spectra even at temperatures up to 2700C (spectrum A).

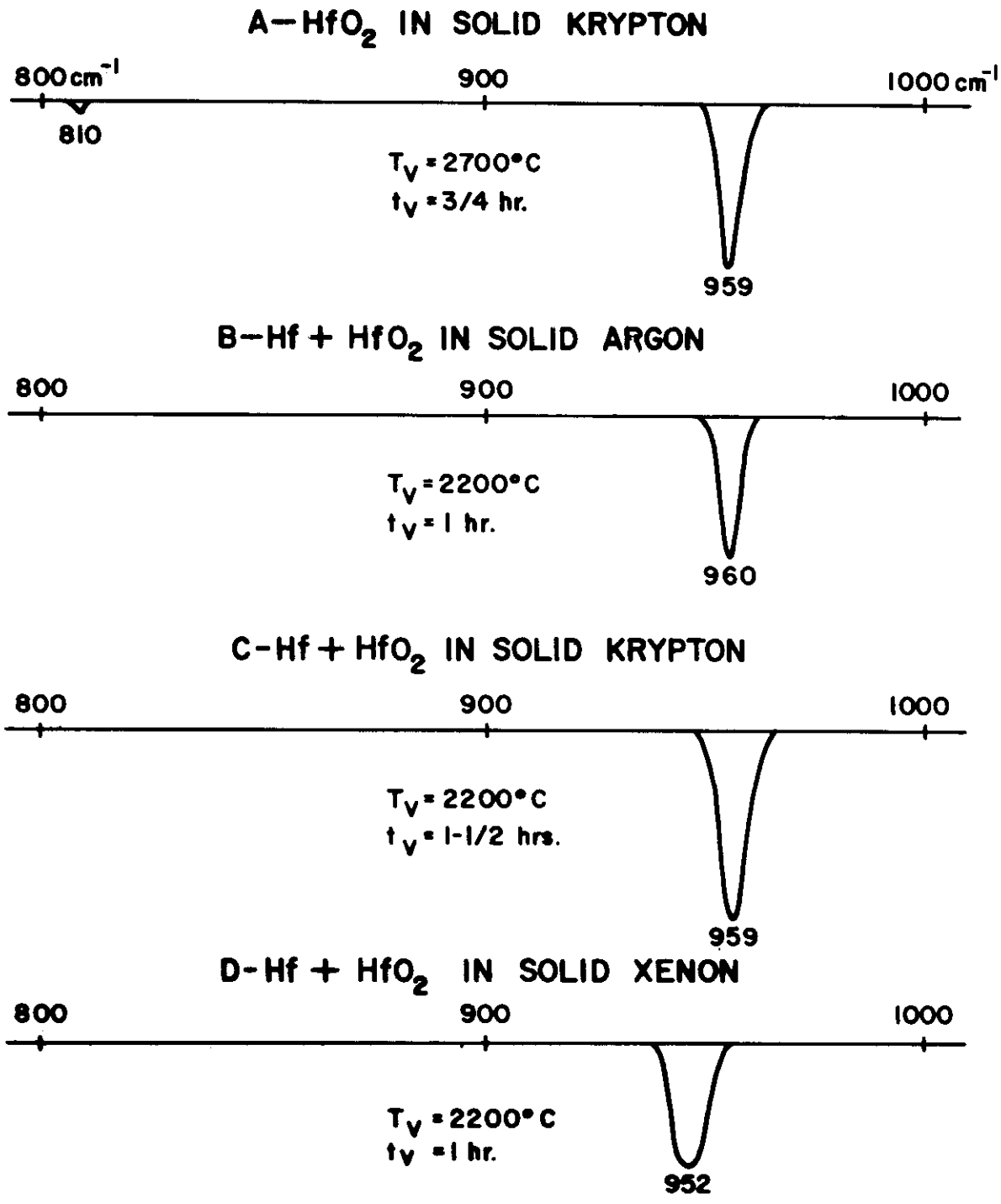

Figure 22. Spectra Of Matrix Isolated Vapors From Hafnia

D. Resonance Line Absorption Studies:

In the preceding annual report[3], the technique of resonance line absorption was used to determine the vapor pressure of titanium over titanium diboride in a fixed boron environment and thereby arrive at the thermodynamics of vaporization of TiB_2. The resonance line absorption technique used here was that of G. Vidale[24-27] which uses a very narrow atomic line source generated in a hollow cathode. This line source is then absorbed by hot atoms of the same element vaporized from the sample in question contained in a furnace. Since the hot atoms give rise to an absorption line much wider than the source emission line, absorption of the source line takes place at the center of the wider line and essentially Beer's law is obeyed. This technique offers the advantages of high sensitivity, ease of calculation, and allows the use of relatively low resolution spectrophotometry. However, when this technique was attempted on the absorption of the boron resonance lines, it was found that a sufficiently narrow and intense enough source line could not be readily generated. For this reason and also since it was of interest to develop new techniques applicable to the investigation of high temperature vaporization phenomena, a technique using the total absorption, i.e., the absorption as a function of wave length, of an atomic line, as a measure of its concentration, was developed. A preliminary discussion of the technique applied to boron has already been given in the preceding annual report[3]. The phenomena of total absorption and its variation with the density of absorbers is discussed in detail by Mitchel and Zemansky[28]. This technique has been applied to alkali metal emission in flames by Hofmann and Kohn[29] and to absorption by Kaskan[30]. The advantage of this technique over the narrow line method lies primarily in being able to use a continuum for a source--thus eliminating the need for the narrow line source and the difficulties in attaining sufficient intensity. This technique is also much less affected by the hyperfine structure of the absorption line.

The total absorption, or integrated absorption, is defined by:

$$Ag = \frac{2\pi \times \text{area under absorption curve}}{I_o} \qquad (19)$$

I_o = incident intensity

and is obtained by measuring the area under the transmission vs wave length tracing as recorded by the spectrophotometer. The variation of the total absorption with concentration is known as the curve of growth and it is this curve of growth which must be determined in order to use the technique to measure concentrations and hence vapor pressures of the atom under question. In general when the gas in question is sufficiently dilute; i.e., optically thin, the total absorption will vary linearly with concentration. As the gas becomes more concentrated, the

total absorption will fall off and in the limit of an optically thick gas, will have a square root dependency on the atom concentration. The absolute magnitude of the total absorption generally will be a function of N, the number of absorbers/cc.; f, the atomic oscillator strength; ℓ, the path length; $\Delta\nu_D$, the Doppler half width; and a, the ratio of collision half width to Doppler half width. In the case of boron, no reliable values for the oscillator strengths are available. Nevertheless, by use of an artifact, a curve of growth for boron can be obtained. In the case of the boron doublet at 2497.73 Å and 2496.78 Å, these lines represent transitions from the $^2P_{3/2,1/2}$ ground state to the $^2S_{1/2}$ excited state. At high temperatures, the population of the $^2P_{3/2}$ state will be twice that of the $^2P_{1/2}$ state, and assuming the oscillator strengths are the same, the ratio of the total absorption of these two lines, in the limit of an optically thin gas, should be 2:1. This indeed is borne out by our measurements. As the gas becomes more concentrated, this ratio falls off, however, the population ratio; i.e., $N_{2497}:N_{2496}$ still remains 2:1. It is this fact that allows us to obtain the total absorption as a function of relative concentration. At a particular temperature, with a cell containing boron in the furnace, the total absorptions for the 2497 Å and 2496 Å are determined; an arbitrary value for the concentration of say the $^2P_{3/2}$ state is selected and hence half this concentration must be assigned to the $^2P_{1/2}$ state. Thus two points are obtained on the curve of growth and a line can be drawn through them. The temperature is changed making sure the parameter "a" is still constant (by maintaining P/T constant where P is the inert gas pressure in the furnace), and the total absorptions of each line are again determined. If the temperature change has been such that the total absorption of either the 2497 Å or the 2496 Å line now falls in between the previously measured points, the concentration for that point can be read off the curve and the corresponding concentration obtained for the other line (this will differ by factor of two from its counterpart). In this manner, a complete curve of growth can be obtained. The procedure will become clearer when the actual data are presented in the next sections. Once the curve of growth is obtained, it can be compared with calculated curves of growth for single lines at various "a" values. By adjusting the relative concentration (abscissa) to make it coincide with a known curve, the value for "a" can be estimated. This procedure has been followed for boron and the results presented in the following section.

Boron

The experimental set-up is quite similar to that which has already been described[3] except for two modifications. The hollow cathode source has been replaced by a Beckman type deuterium lamp in order to provide a continuous source. The light from this source is collimated, chopped and in a manner quite similar to our previous work, is allowed

to pass through a boron containing cell centered in the heater tube of the furnace. The light is then imaged on the slit of the 1/2 meter JACO spectrophotometer and the output amplified and recorded. In order to limit electrical noise, we have replaced the 120 cycle chopper and amplifier with a 13 cycle Perkin-Elmer chopper and amplifier. Spectra of the 2497 Å and 2496 Å boron resonance lines were observed in the second order and extraneous furnace light limited by a Corning #9863 filter. Much difficulty was encountered in finding a suitable container for the boron and finally, boron nitride was found to be the most suitable. A nominal eight inch cell was fabricated out of BN entirely similar to our previously used graphite cells. Temperatures were read with a micro-optical pyrometer on both ends of the cell and in the center, these were then averaged in a manner previously described. Figure 23 shows a schematic of the experimental set-up used and a detailed drawing of the boron nitride cell. A sample of boron powder was obtained from the Cooper Metallurgical Co.; this material had a nominal purity of 99.6%. Prior to use, the empty boron nitride cell was heated to temperatures around 2000°C and thoroughly degassed. The boron powder was placed in the BN cell and spread over the full length of the cell. This cell was placed in the center of the graphite heater tube; the furnace evacuated and the sample thoroughly degassed at 2000°C. The temperature of the furnace was then lowered and purified helium was admitted to the desired ambient pressure. The furnace was then brought to the temperature at which measurements were to be made. The boron 2497.73 Å and the boron 2496.78 Å lines were scanned with the spectrophotometer at its slowest speed (approximately 1 Å/min.) and the transmissions recorded. Each line was scanned at least three times at a particular temperature. The temperature was then changed and the helium pressure adjusted to keep P/T (consequently "a") constant and the spectrophotometric measurements repeated. This process was continued over the entire temperature range reported. The area of the absorbed part of the transmission vs. wave length curves were determined and the total or integrated absorption for each line obtained. Values of the measured total absorption at various temperatures are given in Table 11.

It is seen from Table 11 that, as the concentration of absorbers becomes smaller (lower temperatures) and consequently the gas becomes optically thin, the ratio of the total absorption of the 2497 Å to 2496 Å lines indeed approaches two, indicating the validity of the assumption that the oscillator strengths of the two lines are equal. In the actual construction of the curve of growth, a log-log plot of the variables $\frac{Ag\ (\ln 2)^{1/2}}{\Delta_D}$ and $\frac{Nf\ \ell\ (\ln 2)^{1/2}}{\pi\Delta_D}$ were used rather than the total absorption, Ag, and the concentration, N, respectively. It is actually these variables which are used in the calculation of curves of growth. Following the procedure outlined previously, the curve of growth for boron was obtained and is given in Figure 24. The abscissa in Figure

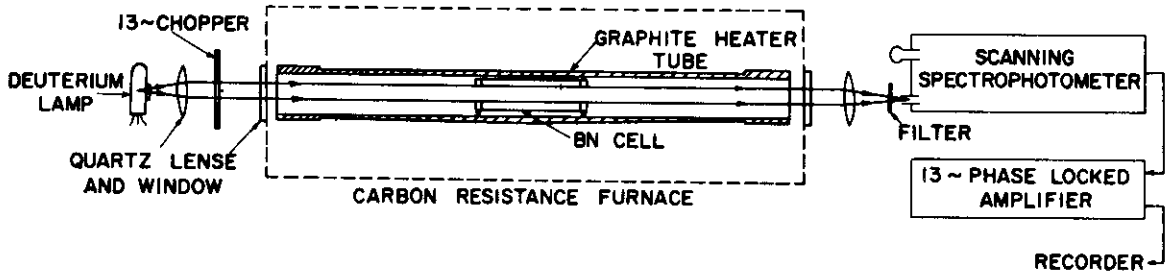

BORON NITRIDE ABSORPTION CELL

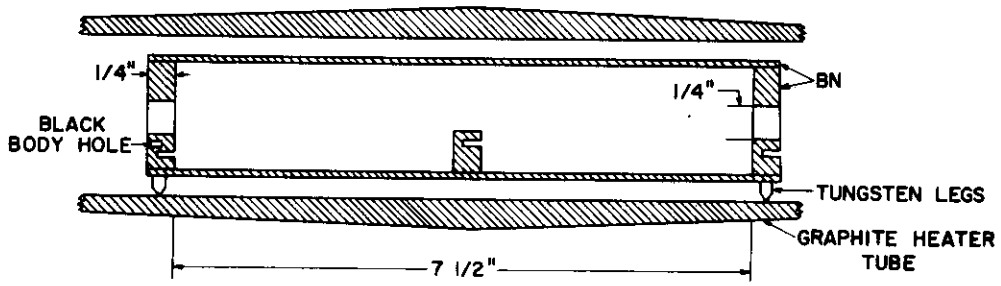

Figure 23. Experimental Apparatus For Total Absorption Studies

TABLE 11

TOTAL ABSORPTION OF BORON

Temperature, ^{o}K	P_{Helium}, cm. Hg.	Total Absorption, sec^{-1}	
		λ =2497.73 Å	λ =2496.78 Å
2065	44.0	1.31×10^{10}	0.71×10^{10}
2095	44.7	1.65×10^{10}	1.01×10^{10}
2117	45.0	1.92×10^{10}	1.30×10^{10}
2137	45.8	2.24×10^{10}	1.58×10^{10}
2175	46.2	2.72×10^{10}	2.00×10^{10}
2220	47.3	3.37×10^{10}	2.63×10^{10}
2268	48.5	4.12×10^{10}	3.09×10^{10}

Path length ℓ = 19.0 cm.

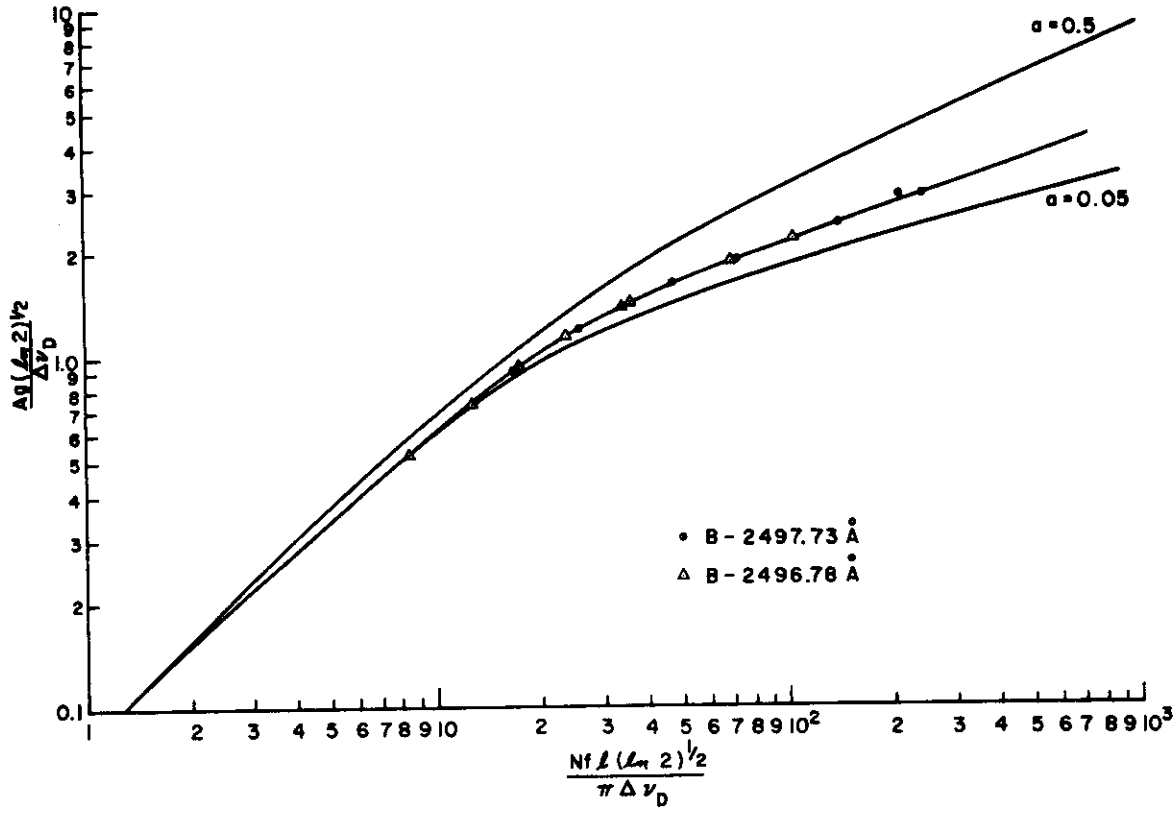

Figure 24. Curve Of Growth Of Boron

24 has been adjusted to make the optically thin end of the curve (small values of $\frac{Nf\ \ell\ (\ln 2)^{1/2}}{\pi\Delta\nu_D}$, coincide with known calculated curves by overlaying the experimental (relative) curve of growth and sliding the abscissa until coincidence is obtained at the low end. In this manner, it is seen from Figure 24 that the value for a, the ratio of collision to Doppler broadening, lies between 0.5 and 0.05. The abscissa values can be looked upon as relative concentrations since the value for f, the oscillator strength, is not known. From these relative concentrations, quantities proportional to the vapor pressure can be obtained. Applying these considerations to the total absorption of the boron 2497 Å line, the relative pressures of boron over boron metal as function of temperature have been obtained. These results are presented in Table 12. A second law treatment of these relative pressures can be used to obtain a heat of vaporization of boron. A Clausius-Clapeyron plot of the data is given in Figure 25, and a least squares analysis leads to the following equation for the relative vapor pressure of boron as a function of temperature:

$$\log AP = -\frac{28.303 \times 10^3}{T} + 28.316 \qquad (20)$$

The corresponding value for the heat of vaporization of boron is found to be $\Delta H_{2150} = 129.5$ kcal/mole, which leads to a $\Delta H_{298} = 132$ kcal/mole. This is in excellent agreement with the value 132.6 kcal/mole as given in the JANAF tables[16]. We have, therefore, evaluated the constant A by comparison of our AP values with the vapor pressure of boron as given in the JANAF tables. This leads to a value for log A equal to -20.925. It is now possible to use the curve of growth to obtain absolute vapor pressures for boron directly by measuring the corresponding total absorptions of the 2497 Å line. Parenthetically, the value for the oscillator strength for the boron transitions can be evaluated from the constant A, since A is $\frac{\pi R}{f\ \ell\ (\ln 2)^{1/2} \times 6.023 \times 10^{23}}$. The oscillator strength obtained in this fashion is equal to 0.033. This appears to be rather small for the resonance transition involved and indeed may reflect some systematic error in our method or might infer that the calibration vapor pressures of boron, from the JANAF tables, are too large. Nevertheless, the method appears to be quite reproducible and indeed is capable of obtaining boron pressures which are compatible with the JANAF tables. We have, therefore, applied this technique to the measurement of boron vapor pressures over the zirconium diboride system.

Zirconium Diboride

The pressures of boron over ZrB_2 were measured using the above described technique. Two kinds of experiments were carried out in-

TABLE 12

RELATIVE BORON VAPOR PRESSURES AT VARIOUS TEMPERATURES

Temperature ^{o}K	$1/T \times 10^{5}$	$\frac{Ag\ (\ln 2)^{\frac{1}{2}}}{\Delta\nu_{D*}}$	$\frac{Nf\ell\ (\ln 2)^{\frac{1}{2}}}{\pi\ \Delta\ \nu_{D}}$	$\log \frac{NTf\ell\ (\ln 2)^{\frac{1}{2}}}{\pi} = \log AP$
2065	48.43	0.92	16.6	14.610
2095	47.73	1.15	25.8	14.809
2117	47.24	1.33	34.0	14.937
2137	46.79	1.55	47.0	15.083
2175	45.98	1.86	74.0	15.292
2220	45.05	2.28	138.0	15.576
2268	44.09	2.76	241.0	15.833

* $\Delta\nu_{D} = 7.16 \times 10^{-7}\ \nu_{o}\sqrt{T/M}$

$0.5 < a < 0.05$

ν_{o} - frequency of 2497 Å line

T - Temperature

M - Molecular Weight Boron

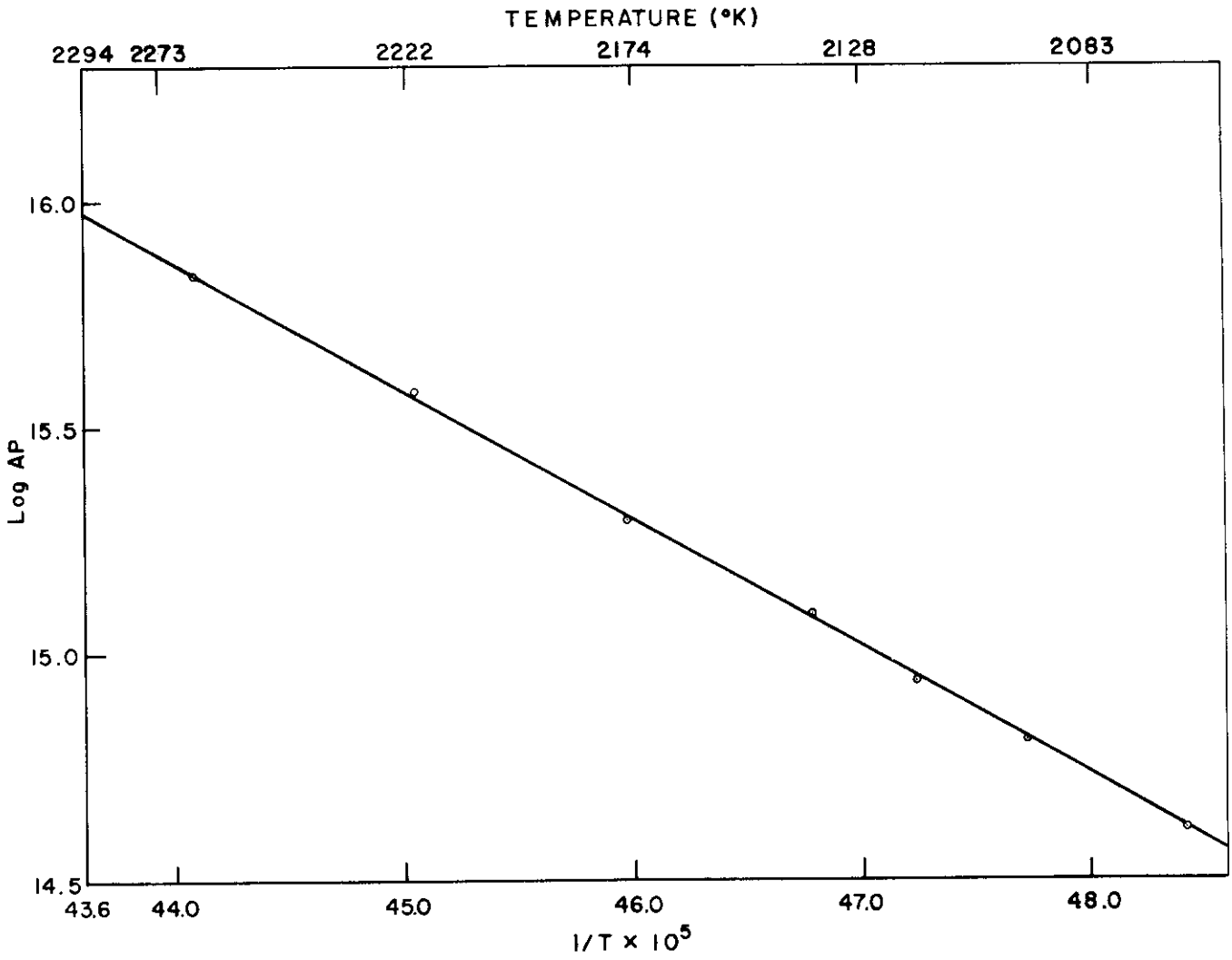

Figure 25. Log AP Vs $\frac{1}{T}$ For Boron

volving ZrB_2. In the first experiment, the boron pressures were determined as a function of temperature over the univariant system ZrB_2 and graphite. The equation for the reaction is

$$ZrB_2(s) + C(s) \rightarrowtail ZrC(s) + 2B(g) \qquad (21)$$

In this case, the partial pressure of boron determines the equilibrium constant and hence the free energy change of (21). From this, it is possible to obtain the heat of formation of ZrB_2. In the second experiment, an attempt was made to measure both the boron and zirconium pressures over pure ZrB_2 with precautions taken to prevent any reaction with carbon. The equilibrium constant and hence the free energy of vaporization of the diboride is then directly computed from both measured pressures.

The apparatus used in the first experiment was entirely similar to the set-up used in the boron vapor pressure determinations except that the boron nitride cell was replaced by a conventional graphite cell similar to those previously described[3]. A sample of zone refined zirconium diboride was obtained from the Arthur D. Little Company and a chemical analysis performed by the Ledoux Company indicated the following weight percentages:

Total Zirconium 81.47%

Total Boron 18.48%

and appears to yield a stoichiometry somewhat low in boron. This material was mixed with an equal weight of spectroscopic grade graphite and loaded into a standard graphite cell. Total absorption measurements of the boron 2497 Å line were carried out at various temperatures using an inert gas atmosphere of helium so that the "a" value was the same as that in the pure boron determinations. From the total absorption measurements, the corresponding pressures of boron were determined via the curve of growth. These results are summarized in Table 13.

The vapor pressures so obtained were subjected to a Second Law treatment and the heat of reaction for (21) was found to be, $\Delta H_{\sim 2400^\circ K}$ = 293.6 kcal/mole. Using this value and the JANAF Tables to obtain thermodynamic data for $ZrB_2(s)$, C(s), ZrC(s) and B(g), the heat of fo mation at 298°K for zirconium diboride was calculated to be $\Delta H^\circ_f 298$= -74.6 kcal/mole. Applying the Third Law to reaction (21) using the measured boron pressures, the $\Delta H^\circ_f 298$for ZrB_2 was found to be -74.4 kcal/mole. These results are summarized in Table 14. The agreement between the Second and Third Law results is quite remarkable. These results are in good agreement with those reported in the JANAF Tables.

TABLE 13

VAPOR PRESSURE OF BORON OVER ZrB_2 PLUS GRAPHITE

Temperature ^oK	$1/T \times 10^5$	$\frac{Ag\ (\ln 2)^{\frac{1}{2}}}{\Delta\nu_D}$	$\frac{Nf\ (\ln 2)^{\frac{1}{2}}}{\pi\Delta\nu_D}$	log AP *	log P_{Boron} (atm)
2264	44.17	1.16	24.5	14.811	-6.115
2320	43.10	1.70	54.5	15.174	-5.752
2380	42.02	2.17	106	15.479	-5.445
2408	41.53	2.52	163	15.674	-5.248
2463	40.60	3.03	285	15.931	-4.991
2495	40.08	3.56	450	16.138	-4.780

$$ZrB_2(s) + C(s) = ZrC(s) + 2B(g)$$

* Normalized to the same length as in pure boron determination.

TABLE 14

THIRD LAW TREATMENT OF MEASURED BORON PRESSURES OVER ZrB_2 PLUS GRAPHITE

Temperature °K	log P_{Boron} (21) (atm)	ΔF^{o}_{T} (21) kcal/mole	$-\Delta \frac{(F^{o}_{T} - H^{o}_{298})}{T}$ (21) $\frac{cal}{mole - {}^{o}K}$	ΔH^{o}_{298} (21) kcal/mole
2264	-6.115	126.71	74.200	294.70
2320	-5.752	122.13	74.192	294.26
2380	-5.445	118.60	74.179	295.15
2408	-5.248	115.66	74.173	294.27
2463	-4.991	112.5	74.160	295.17
2495	-4.780	109.15	74.153	294.16
			Ave. ...	294.62

$$ZrB_2(s) + C(s) = ZrC(s) + 2B(g) \qquad (21)$$

ΔF^{o}_{T} (21) $= -2\ RT\ \ln P_B$

$\Delta H^{o}_{f298} ZrB_2 = -294.62 + 2\ (132.62) - 45.00$

$= -74.38$ kcal/mole

In the second experiment, the apparatus was modified in order to prevent any interaction between the graphite heater tube and the ZrB_2 sample so that both the boron and zirconium vapor pressures could be measured. This was accomplished to a large extent by the following modifications. The graphite heater tube was lined with a tantalum tube slightly smaller in diameter so that no contact was made between the two in the hot zone of the furnace. The tantalum liner was supported by boron nitride rings in the cold ends of the heater tube so as to electrically insulate the liner from the graphite. In order to prevent sagging of the tantalum liner in the hot zone, a molybdenum ring was used to support the liner in the center of the furnace. A tungsten cell was used to contain the ZrB_2 sample. This was 4" in length and approximately $\frac{1}{2}$" in diameter. It was obtained from the Hoskins Manufacturing Co. and was made by vapor deposition. This cell was fitted with end pieces which were made from tantalum sheet and contained 1/8" diameter holes in order to allow light to be passed through the cell. The tungsten cell was supported in the center of the tantalum liner by means of three molybdenum rings and a sample of the same zirconium diboride as used previously was loaded into this cell. A schematic of this apparatus is given in Figure 26.

The hollow cathode resonance line absorption technique, as previously used with ZrC, was used to obtain the zirconium vapor pressures. This necessitated interchanging the continuous source, for the boron measurements, with a standard zirconium hollow cathode source. Since helium gas was used for the inert atmosphere, rather than argon (used with our previous ZrC work), a recalibration of the line absorption of pure zirconium metal in helium was carried out so that absolute vapor pressures could be obtained. This was done in a fashion completely analogous to the ZrC work except helium was substituted for argon. Furthermore, since these measurements were taken in an 8" long cell and the ZrB_2 was contained in a 4" cell, the apparent A'P obtained from these measurements had to be reduced by a factor of two in order to calculate the zirconium pressures over the ZrB_2. A similar situation exists for the boron measurements. Single point checks on both the zirconium and boron metals, contained in 4" long cells, indeed indicated that $\overline{/AP/}_{4"} = \frac{1}{2}\ \overline{/AP/}_{8"}$ within the experimental error. Absorption measurements of the $Zr_{3601\ \text{Å}}$ line were carried out over ZrB_2 at various temperatures; these results along with the measurements over the pure metal are given in Table 15. The absolute vapor pressures of zirconium were obtained by evaluating the constant A' by a comparison with the known vapor pressure of zirconium metal. Absolute values for the vapor pressures of zirconium over zirconium diboride are also included in Table 15.

Boron pressures were obtained using the total absorption technique as described before. These results are given in Table 16.

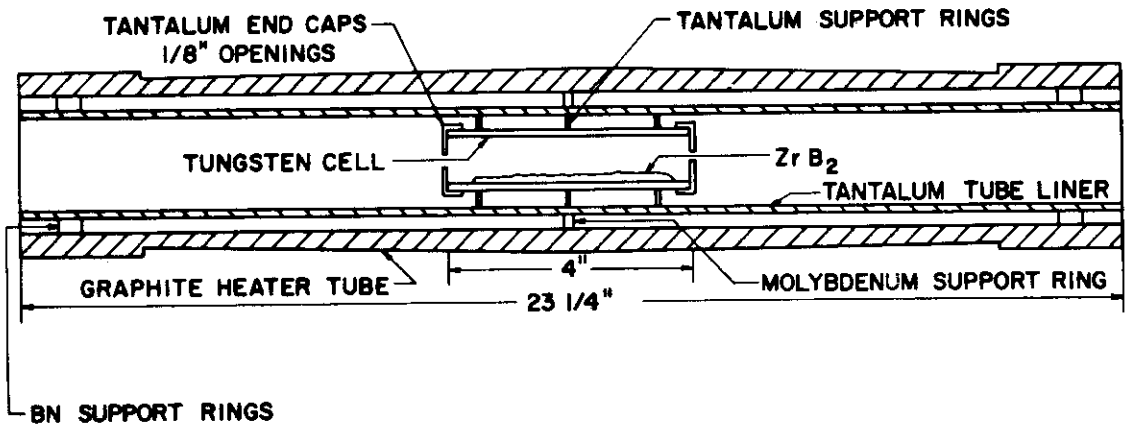

Figure 26. ZrB_2 Absorption Cell Apparatus

TABLE 15

ZIRCONIUM PRESSURES FROM RESONANCE LINE ABSORPTION

Material	Temperature °K	P_{Helium} cm.Hg	I/Io [a]	log $\overline{T^{3/2}}$ log Io/I = log A'P	- log P_{Zr}(atm)
Zr metal	2102	20.0	.792	3.9900	
	2104	20.0	.774	4.0298	
	2106	20.0	.744	4.0838	
	2103	20.0	.786	4.0035	
	2100	20.0	.764	4.0508	
	2097	20.0	.770	4.0378	
	2100	20.0	.780	$\overline{4.0145}_{8"}$	7.941 [b]
	$\overline{\log A'}_{4"} = -11.6525$			$\overline{3.7115}_{4"}$	
ZrB_2 in 4" W cell	2318	21.5	.896	3.7289	7.924
	2366	21.5	.800	4.0434	7.609
	2368	21.5	.799	4.0484	7.604
	2369	21.5	.763	4.1339	7.519
	2372	21.5	.792	4.0671	7.585
	2382	21.5	.737	4.1861	7.466
	2409	21.5	.634	4.3694	7.283
	2453	21.5	.434	4.6433	7.009
	2459	21.5	.444	4.6327	7.020
	2462	21.5	.382	4.7071	6.945
	2468	21.5	.364	4.7328	6.920

a - For The Zr 3601Å Resonance Line
b - From JANAF Tables

TABLE 16

BORON PRESSURES OVER ZrB_2 FROM TOTAL ABSORPTION MEASUREMENTS

Temperature [a] ^{o}K	P_{Helium} cm.Hg	$\frac{Ag\ (\ln 2)^{\frac{1}{2}}}{\Delta\nu_D}$ [a]	$\left[\frac{Nf\ell\ (\ln 2)^{\frac{1}{2}}}{\pi\Delta\nu_D}\right]_{4"}$ [b]	$\left[\log AP\right]_{8"}$	- log P_B (atm) [c]
2445.5	52.0	.417	6.4	14.607	6.318
2450	52.2	.439	6.8	14.635	6.290
2458	52.2	.493	7.8	14.696	6.229
2464	52.2	.528	8.5	14.735	6.190
2468	52.3	.606	9.9	14.802	6.123
2487	52.4	.696	11.8	14.884	6.041
2504	53.0	.802	14.1	14.965	5.960
2518	53.2	.899	16.4	15.035	5.890

a - average results based on at least three separate measurements

b - from curve of growth

c - log P(atm) = -20.925 + log AP

The vapor pressure data for zirconium and boron over ZrB_2 as a function of temperature are presented graphically in Figure 27.

From an examination of these results, several interesting conclusions are immediately apparent. The zirconium data show to some extent an erratic behavior and indeed during the course of the measurements, it was noticed that large fluctuations in the line absorption took place when the sample was initially heated to temperature and only after remaining at temperature for a period of time did these fluctuations begin to disappear, the trend being from larger to smaller vapor pressures. Furthermore, if indeed ZrB_2 is congruently vaporized, the pressure of boron to zirconium at a particular temperature should be 2:1. The observed ratio is more nearly 6:1, indicating a departure from congruent vaporization. Apparently there is some reduction of the ZrB_2 taking place because of contamination with carbon. Indeed a chemical analysis performed by the Ledoux Co. on the sample of ZrB_2 after our measurements were completed indicated the presence of approximately 0.5% by weight of total carbon. Therefore, some enhancement of the boron pressure via a reduction reaction must have occurred with the consequential reduction in the zirconium pressure. The initial fluctuations in our line absorption measurements can also be explained by this reaction of the ZrB_2 with a residual carbon containing specie, probably carbon monoxide, which is almost invariably present in the furnace. Presumably after the initial heating, the carbon containing specie is consumed and the measurements become stable.

It is also apparent that the temperature range over which the zirconium pressures were taken does not completely coincide with the range over which the boron pressures were taken. In fact, there is only coincidence at the upper range of the zirconium measurements and the lower range of the boron measurements. This situation was unavoidable, since, as has been pointed out previously, the line absorption technique is more sensitive than the total absorption technique; and furthermore, the oscillator strength for the zirconium transition is probably greater than for the boron transition, so that when measurable boron absorption is reached, the zirconium line absorption is almost completely black. For this reason, in order to calculate equilibrium constants for the vaporization of ZrB_2, i.e., $k_p = P_B^2 P_{Zr}$ and hence thermodynamic properties, the vapor pressures of zirconium and boron as function of temperature were least squared to a Clausius-Clapeyron type relationship and extrapolation of each vapor pressure to a common temperature was made with the help of the resulting equations. The vapor pressure equations for zirconium and boron over ZrB_2 are as follows:

$$\log P_{Zr\ (atm)} = -\frac{38.224}{T} + 8.565 \qquad (22)$$

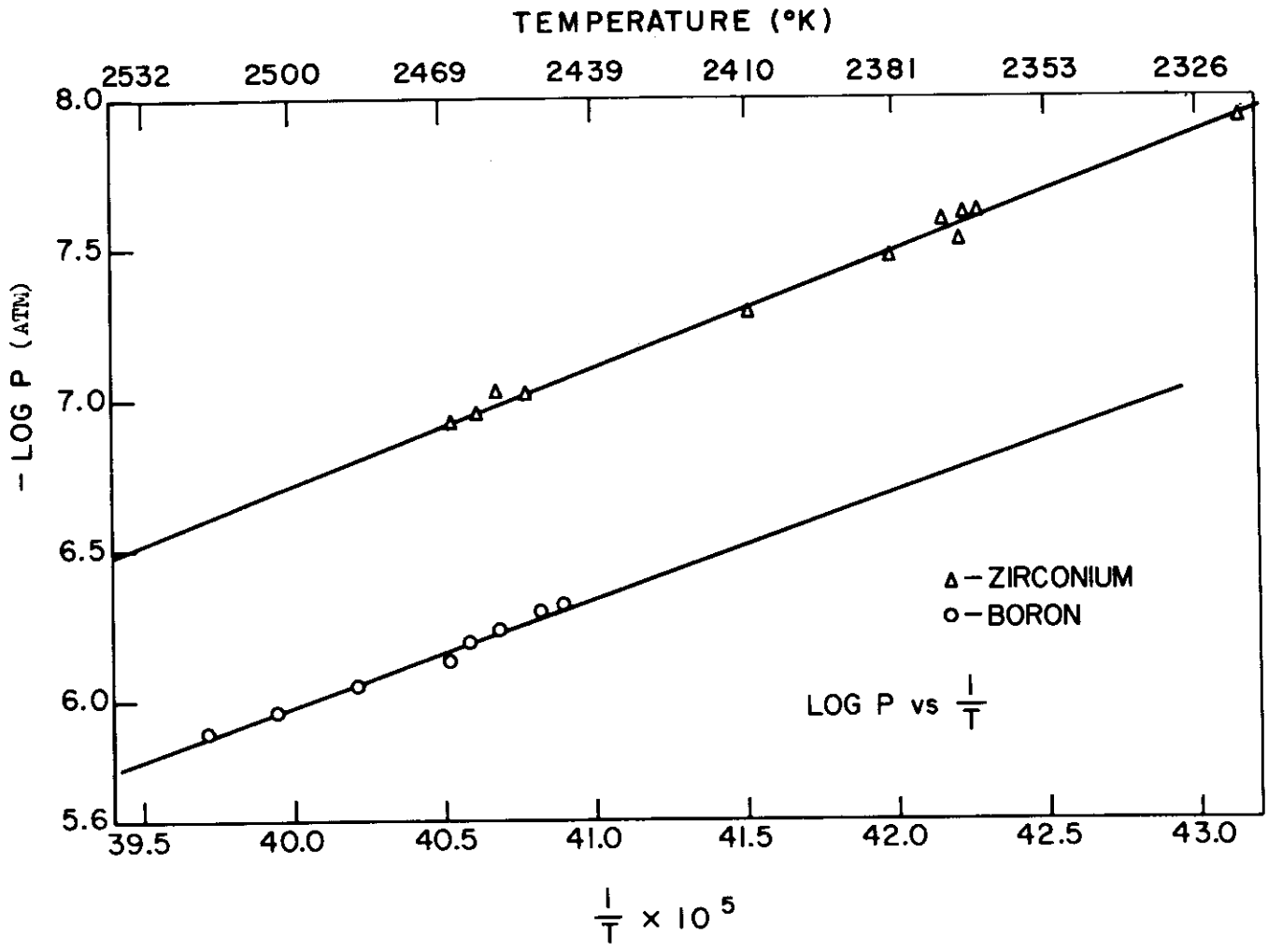

Figure 27. Log P Vs $\frac{1}{T}$ for Boron And Zirconium Over ZrB_2 (+C)

and

$$\log P_{B(atm)} = -\frac{36.205}{T} + 8.503 \qquad (23)$$

A Third Law analysis of these pressures using the thermodynamic functions for $ZrB_2(s)$, B(g) and Zr(g), as given in Reference 16, yields a heat of formation for ZrB_2 at 298°K, $\Delta H^{o}_{f298}\ ZrB_2 = -75.6$ kcal/mole. These results are summarized in Table 17.

This value for $\Delta H^{o}_{f298}(ZrB_2)$ is in excellent agreement with the value ~ -74.5 kcal/mole obtained in the first experiment.

It is rather difficult to estimate errors associated with the above measurements. Nevertheless, it is felt that, in the case of the boron absorption studies, the resulting total absorption measurements are accurate to approximately ± 10%, which leads to approximately ± 1 kcal/mole error in the resulting heat. In the case of the zirconium measurements, as mentioned earlier, large fluctuations were noted during the initial heating and as much as a factor of two change was noted. This change was always in the direction of smaller vapor pressures and indeed leads to a possible error in the heat of approximately -3 kcal/mole. It is believed, therefore, that the error to be associated with the resulting heat of formation obtained from the first experiment; i.e., reaction (21), is approximately ± 1 kcal/mole or $\Delta H^{o}_{f298}(ZrB_2) = -74.5 \pm 1$ kcal/mole and the error associated with this heat from the second experiment; i.e., reaction (24), is approximately $\pm \frac{1}{4}$ kcal/mole or $\Delta H^{o}_{f298}(ZrB_2) = -75.6 \pm \frac{1}{4}$ kcal/mole. These errors do not include the errors associated with the thermodynamic quantities obtained from the JANAF tables.

E. Summary and Conclusion

Measurements of nitrogen pressure over HfN have been made between 0.45 and 0.50 atom fraction nitrogen. Previously reported[1] discrepancies in the data have been found to be due to a diffusion limitation.

Nitrogen pressures have been measured over tantalum-nitrogen compositions from 0.02 to 0.48 atom fraction N. Very interesting discrepancies have been found at compositions above 0.35 atom fraction N. "Most probable" values for the nitrogen isotherms in this system have been proposed based on present measurements and equilibrium considerations

The vaporization of zirconium diboride has been studied using a microbalance system. Vaporization behavior shows a congruently vaporizing composition at $ZrB_{1.931}$ and an evaporation coefficient of 0.098. Equilibrium boron and zirconium pressures have been calculated yielding a heat of formation of $ZrB_{1.931}$ of -76.6 by the third law method and

TABLE 17

HEAT OF VAPORIZATION AND FORMATION OF $ZrB_2(s)$

$$ZrB_2(s) = Zr(g) + 2B(g) \qquad (24)$$

Temperature °K	- log k_p (24)	ΔF°_T (24) kcal/mole	$\Delta \frac{(F^\circ_T - H^\circ_{298})^a}{T}$ (24) $\frac{cal}{mole - {}^\circ K}$	ΔH°_{298} (24) kcal/mole
2300	-22.532	237.15	-108.76	487.29
2350	-21.503	231.24	-108.73	486.75
2400	-20.530	225.47	-108.70	486.34
2450	-19.589	219.62	-108.66	485.84
2500	-18.682	213.72	-108.63	485.29
			Ave. ...	486.30

$$\Delta H^\circ_{f298}\ ZrB_2 = -486.30 + 2\ (132.62) + 145.42$$

$$= -75.6 \text{ kcal/mole}$$

a. $-\Delta\ (F^\circ_T - H^\circ_{298})/T = \overline{/}(F^\circ_T - H^\circ_{298})/T\overline{/}_{Zr} + 2\ \overline{/}(F^\circ_T - H^\circ_{298})/T\overline{/}_B - \overline{/}(F^\circ_T - H^\circ_{298})/T\overline{/}_{ZrB_2}$

-67.1 kcal per mole by the second law method using JANAF auxiliary data.

The infrared spectra of ThO_2, ThO, ZrO_2, and ZrO have been observed in rare gas matrices. A linear model for ThO_2 and ZrO_2 is consistent with the observed frequencies and tentative assignments for these molecules have been made. No evidence for the HfO_2 molecule was found. The fundamental vibrational frequencies for ThO, ZrO, and HfO were established. More definite assignments in the case of the triatomic molecules await the use of O^{18} isotopically enriched material.

The heat of formation of zirconium diboride was obtained in two separate kinds of experiments. In the first, boron pressures were measured using a total absorption technique over the univariant system ZrB_2 and graphite. In the second experiment, both zirconium and boron pressures were measured over pure ZrB_2 by means of the resonance line absorption technique and the total absorption technique. Values for the heat of formation of ZrB2 by the third law method are -74.5 kcal/mole and -75.6 kcal/mole respectively by the two methods. The total absorption technique (curve of growth method) was perfected for use with boron and was also applied to the study of the vaporization of boron metal.

F. References - Vaporization Studies

1. Coffman, J. A., et al., Carbonization of Plastics and Refractory Materials Research, WADD Technical Report 60-646, Part I (Feb. 1961).

2. Ibid., Part II (January 1963).

3. Kibler, G. M., et al., Carbonization of Plastics and Refractory Materials Research, WADD Technical Report 60-646, Part III, Vol. 2, (March 1964).

4. Andrews, M. R., Jour. Am. Chem. Soc. 54, 1845 (1932).

5. Slade, R. E. and Higson, G. I., Jour. Chem. Soc., 115, 215 (1919).

6. Anderson, J. S., in The Physical Chemistry of Metallic Solutions and Intermetallic Compounds, Vol. II (p. 240), Chemical Publishing Co., Inc., New York (1960).

7. Veleckis, E., Rosen, C. and Feder, H., J. Phys. Chem. 65, 2127 (1961).

8. Gebhardt, E., Seghezzi, H. and Fromm, E., Z. Metallk. 52, 464 (1961).

9. Pemsler, J., J. Electrochem. Soc. 108, 744 (1961).

10. Schönberg, N., Acta Chem. Scand. 8, 199 (1954).

11. Brauer, G. and Zapp, K., Z. Anorg. Chem. 277, 129 (1954).

12. Iczkowski, R., Margrave, J. and Robinson, S., J. Phys. Chem. 67, 229 (1963).

13. McClaine, L. A., Thermodynamic and Kinetic Studies for a Refractory Materials Program.
    a) ASD-TDR-62-204 Part I (April 1962)
    b) ASD-TDR-62-204 Part II (May 1963)

14. Kriege, O. H., The Analysis of Refractory Borides, Carbides, Nitrides and Silicides, Los Alamos Scientific Laboratory Report LA-2306 (1959).

15. Motzfeldt, K., J. Phys. Chem. 59, 139 (1955).

16. JANAF Thermochemical Tables, The Dow Chemical Company, Midland, Michigan.
a) Zr(g) Table dated June 30, 1961.
b) B(g) Table dated Dec. 31, 1960.
c) ZrB_2 Table dated Mar. 31, 1963.

17. Leitnaker, J., Bowman, M., and Gilles, P., J. Chem. Phys. 36, 350 (1962).

18. Lawrie, R., "Research on Physical and Chemical Principles Affecting High Temperature Materials for Rocket Nozzles." Contract #DA-30-069-ORD-2787, Quarterly Progress Report, Dec. 31, 1962.

19. Brewer, L. and Rosenblatt, G., Chem. Rev. 61, 257 (1961).

20. Herzberg, G., Infrared and Raman Spectra, D. Van Nostrand Co., 1945.

21. Lagerquist, A., Uhler, U., Barrow, R. F., Arkiv. Fysik 8, 281 (1954).

22. Afaf, M., Proc. Phys. Soc. 63A, 1156 (1950).

23. Sommer, A., White, D., Linevsky, M., and Mann, D. E., J. Chem. Phys. 38, 87 (1963).

24. Vidale, G. L., TIS R60SD333, G. E. Company (1960).

25. Vidale, G. L., TIS R60SD331, G. E. Company (1960).

26. Vidale, G. L., TIS R61SD147, G. E. Company (1960).

27. Vidale, G. L., TIS R60SD330, G. E. Company (1960).

28. Mitchel and Zemansky, Resonance Radiation and Excited Atoms, Cambridge Press (1934).

29. Hofmann, F. and Kohn, H., J. Opt. Soc. 51, 512 (1961).

30. Kaskan, W., TIS 61-RL-(2823C), G. E. Company (1961).

III SPECTRAL EMISSIVITIES OF REFRACTORY MATERIALS

A. Background

Earlier annual reports have described the development and refinement of apparatus and experimental techniques for obtaining normal total emissivities at temperatures greater than 3000°K. These reports have also presented results obtained in measuring normal spectral emissivities of a number of refractory materials.

Specifically, the first annual report(1) dealt with the design and construction of the emissometer capable of heating the specimen under test to temperatures of 3000°K while measuring the spectral radiation from both the specimen surface and a black body reference cavity drilled into it. Also presented were normal spectral and normal total emissivity data for polycrystalline tungsten, tantalum carbide and zirconium carbide.

The second annual report(2) presented similar data for tantalum, molybdenum, zirconium, tungsten carbides (WC and W_2C), Chromalloy W_2-coated molybdenum - $\frac{1}{2}$% titanium alloy, and siliconized ATJ graphite. Niobium diboride, zirconium diboride, titanium diboride and the nitrides of zirconium, hafnium and tantalum were next studied as described in the third annual report(3).

All previous work in this project, as well as that currently reported, is summarized in Table 18 which lists the normal total emissivities computed from the measured spectral emissivity data.

B. Experimental

1. Apparatus

The apparatus used is patterned after a similar unit of Blau(4) and has been adequately described in earlier annual reports(1,2,&3) under this contract. The equipment consists of an RF heating unit, a vacuum system, gas purifying system, a specimen chamber, external transfer optics, monochromator, detectors and associated electronics. The RF specimen heating unit, Model RFS-4, manufactured by Sylvania Electric Co., supplies RF energy through a water-cooled concentrator mounted inside the specimen chamber. The specimen chamber can be operated at pressures below 5×10^{-6} Torr, or at pressures up to 2 atmospheres. It is fitted with an "O"-ring sealed calcium fluoride window which transmits radiation from the specimen through a system of external transfer optics. A mirror of the optical system oscillates to image alternately on the monochromator slit, the specimen black body reference cavity and a spot on

TABLE 18

NORMAL TOTAL EMISSIVITY - REFRACTORY SOLIDS

	Materials	Temperature °K	Spectral Bandwidth Microns	Normal Total Emissivity
1.	Polycrystalline Tungsten	1830	.5u to 4u	.22
		2040		.24
2.	Nickel	1480	.4u to 5u	---
3.	Tantalum Carbide TaC	1830	.5u to 4.0u	.22
		2250		.26
		2670		.30
		2880		.33
4.	Zirconium Carbide ZrC	2100	.5u to 4.0u	.43
		2270		.44
		2470		.45
		2870		.45
5.	Chromalloy Coated Molybdenum + ½% Titanium	1603	.4u to 5.0u	
		1775		
		1905		
6.	Siliconized ATJ Graphite	1435	to 5.0u	
		1830		
		2040		
		2236		
		2270		
7.	Tantalum	1700	.4u to 5.0u	.17
		2200		.28
		2400		.25
		2800		.30
8.	Molybdenum	1600	.4u to 5.0u	.14
		2000		.18
		2800		.28
9.	Tungsten Carbide (WC)	1400	.4u to 5.0u	.17
		1600		.21
		1800		.27
10.	Tungsten Carbide (W_2C)	1600	.4u to 5.0u	.26
		1800		.31
		2000		.38
		2200		.40
		2400		.40
11.	Zirconium	1400	.4u to 5.0u	.41
		1600		.39
		2000		.43
12.	Niobium Diboride NbB_2	1636	.4u to 5.0u	.30
		1744		.34
		1913		.35
		2289		.41
12.	Zirconium Diboride ZrB_2	1604	.4u to 5.0u	.44
		1702		.46
		2000		.52
		2330		.54
		2480		.65

TABLE 18 (Continued)

NORMAL TOTAL EMISSIVITY - REFRACTORY SOLIDS

Materials	Temperature °K	Spectral Bandwidth Microns	Normal Total Emissivity
14. Titanium Diboride TiB_2	1648	.4u to 4.7u	.48
	1850		.59
	2020		.66
15. Zirconium Nitride ZrN	1895	.4u to 5.0u	.43
	1968		.47
	2064		.59
	2287		.71
16. Tantalum Nitride TaN (Nitrogen Atmosphere)	1648	.4u to 5.0u	.72
	1882		.72
	1990		.74
	2070		.73
17. Hafnium Nitride HfN	1617	.4u to 5.0u	.60
	1809		.64
	2006		.75
	2192		.85
18. Tantalum Nitride TaN (Argon Atmosphere)	1648	.4u to 5.0u	.56
	1851		.66
	1956		.72
	2132		.75
19. Pyrolytic Graphite ("a-b" crystal plane radiating) Vacuum 10^{-6} Torr	1590	.4u to 5.0u	.57
	1611		.56
	1640		.53
	1680		.46
	1808		.39
	1820		.38
	2105		.33
	2200		.32
	2404		.33
	2430		.30
	2735		.24
20. Pyrolytic Graphite ("c" crystal plane radiating) Vacuum 10^{-6} Torr	1409	.4u to 5.0u	.81
	1531		.85
	1718*		.93
	1882		.83
	1914*		.91
	1920*		.91
	1980*		.80
	2054		.71
	2060*		.84
	2149*		.80
	2225		.69
	2319*		.75
21. Single Crystal Tungsten 200 Plane	1605	.4u to 5.0u	.17
	2140		.23
	2419		.25
	2639		.25

* Directly Heated

the surface of the specimen. A 1P21 photomultiplier detects radiation between 0.4 and 0.7 micron while a thermocouple detector is employed between 0.7 and 6 microns. After amplifying and sorting, final reading takes place on a strip chart recorder into which the surface radiation signal is fed at the same time the black body signal voltage is applied across the entire recorder slide wire. Thus the ratio of the two signals as a function of wavelength is recorded. This, taken normal to the specimen surface, is, by definition, the normal spectral emissivity of the specimen.

2. Specimen Preparation and Design

Specimen design, fabrication and preparation were as previously described(3). Variations to established procedures, or those used with specific individual materials only are dealt with while discussing the appropriate material in later sections of this report.

3. Specimen Characterization

Since emissivity values for a given material are intimately dependent upon surface structure and physical and chemical properties, a systematic procedure was followed to characterize each specimen before and after emissivity measurements according to the following sequence:

a. Chemical composition was established by wet chemical analysis to determine major components and spectrochemical analysis to determine the presence of trace elements. In most instances, a record was kept of the elements looked for, but not found.

b. Before making emissivity determinations, photomicrographs of polished specimens were made using standardized light microscope optics.

c. Electron microscope micrographs were made by replicating the polished specimen surface and the resulting surface after measurement.

d. Slow scan X-ray diffraction patterns were obtained. In this step, "d" spacings and line intensity were established and compared to ASTM standards.

e. Specimen weight and density determinations were made in order to detect possible specimen evaporation, densification and chemical changes.

f. Normal spectral emissivity values were then determined up to temperatures below which the specimen remained stable.

Although the above technique is useful in understanding material stability and changes that may take place during measurement of emissivity, it is not possible, in all cases, to relate emissivity properties to specific compositions or surface structure. This is due to the dynamic situation induced by the high temperature at which measurements were made. Thus, in some instances, emissivity properties given are characteristic only of the specimen under the conditions of measurement.

4. Procedure

In making emissivity measurements, the procedure followed was that previously described[3]. That is, the specimen chamber was first pumped to pressures below 5×10^{-5} Torr and, by manipulating the appropriate valves, the system was checked for leaks. Following this, each specimen was degassed at about 700°C. The chamber was then flushed several times with prepurified argon and finally filled with argon to a pressure of about 1.5 to 2 atmospheres. The specimen was thermally stabilized at the test temperature by taking continuous optical pyrometer readings. Also, when the temperature difference between the black body reference cavity and the surface is constant, it can be assumed that surface emissivity is not changing, at least at the pyrometer wavelength. The black body image was then brought into focus on the monochromator slit, and instrument calibration under zero and 100% energy pass conditions were accomplished. This calibration was also checked when switching from photomultiplier to thermocouple detector and again upon completion of the run. Specimen surface and black body temperatures were also measured at the end of each run using a calibrated optical pyrometer. Corrections were made for absorption through the CaF_2 windows and for incomplete reflections from the mirrors.

Wavelength calibration was accomplished periodically using a GE-AH4 mercury lamp. As before, additional periodic checks were made by inserting specific cut-off and cut-on filters in front of the monochromator slit and relating drum readings to filter characteristics. Also, measured values of emissivity at 0.65 micron wavelength were checked against computed values based on measured temperature differences between the specimen surface and black body reference cavity in the specimen, using the following relationship.

$$1/T_s - 1/T_{bb} = (.65/c_2)(\ln \epsilon) \qquad (25)$$

where ϵ = emissivity at 0.65 micron

T_s = surface temperature

T_{bb} = black body temperature

c_2 = 1.4388 (Plank's 2nd radiation constant)

Normal total emissivity was calculated for each specimen test temperature by multiplying the spectral emissivity for a given wavelength interval by the energy fraction radiated from a black body at the same temperature and wavelength interval to obtain the fraction of energy radiated from the specimen. One then simply takes the sum of the energy fractions to obtain normal total emissivity per the following expression:

$$\epsilon_{nt(T)} = \sum \epsilon_{n(T)}\, d\lambda .\ I_{bb(T)}\, d\lambda \qquad (26)$$

where $\epsilon_{nt(T)}$ = normal total emissivity at temperature T

$\epsilon_{n(T)}d\lambda$ = normal emissivity in the wavelength interval $d\lambda$ at temperature T

$I_{bb(T)}d\lambda$ = fraction of energy radiated from a black body at the same wavelength interval and temperature

C. Results and Discussion

1. Tantalum Nitride

Measurements of the spectral emissivity of tantalum nitride in vacuum have been previously reported(3). It was found that dissociation to tantalum takes place at a slow rate starting at about 2000°K. Spectral emissivity was shown to approach that of pure tantalum at temperatures above 2000°K.

When measurements were made in an atmosphere of nitrogen over a range of temperatures from 1648°K to 2070°K, the surface showed a slow change to a polycrystalline powdered structure with an associated increase in spectral emissivity. This granulation of the surface was believed to be caused by additional nitriding of the surface from a composition containing 3.53% nitrogen to a composition closer to the theoretical value of 7.7% nitrogen. Under this condition, emissivity was higher than values obtained in vacuum at the same temperatures. Therefore, it was decided to measure emissivity in an atmosphere of argon.

The specimen was part of the same lot of tantalum nitride used in previously reported studies(3). Its surface was photomicrographed employing both light and electron microscope procedures. In addition, X-ray constants and relative peak intensities were measured before and after making emissivity measurements. Results are given in Appendix B, Tables 34 and 35, respectively.

Lattice spacings, both before and after emissivity measurements, were characteristic of TaN. However, it was noted that additional weak diffraction lines appeared in the pattern after emissivity measurement. In lattice spacings, these are characteristic of Ta5Si and qualitatively could be indexed to appear as Ta_5Si. Because the specimen was observed to exhibit preferred orientation, relative intensities depend greatly on how it is positioned in the goniometer during analysis. The high vanadium and tungsten content could influence spacing values.

Weight and density measurements were made before and after emissivity measurement to 2132°K and are given in Table 19. It can be seen that virtually no change in weight and density took place.

TABLE 19
TANTALUM NITRIDE

	Weight, gm.	Density $\frac{gm}{cc}$.
Before	6.0200	14.36
After	6.0201	14.36
Change	+.0001	.00

The polished surface of the specimen was characterized by taking photomicrographs and electron microscope replicas before and after emissivity measurement. By way of review, specimen surface preparation consisted of polishing on a silk cloth using Linde A grinding compound and finally on a felt cloth with Linde A. The specimen was rinsed in alcohol, care being taken to remove polishing residues from the black body reference cavity.

Figure 28 shows the polished surface structure at 300X before emissivity measurements and after heating to 2132°K in an argon atmosphere. For the polished specimen there is evidence of porosity even though measurement of density indicates a near theoretical value. This apparent discrepancy can be explained by noting that the chemical analysis given in Appendix A, Table 31, shows an excess of 4.2% tantalum based on a TaN composition. Heating to 2132°K induces some change in surface structure with evidence of crystallization, densification and thermal etching having taken place. Figures 29 and 30 are electron microscope photomicrographs of polished TaN before and after heating to 2132°K respectively. Here again there is evidence of thermal etching having taken place bringing slip plane dislocations and

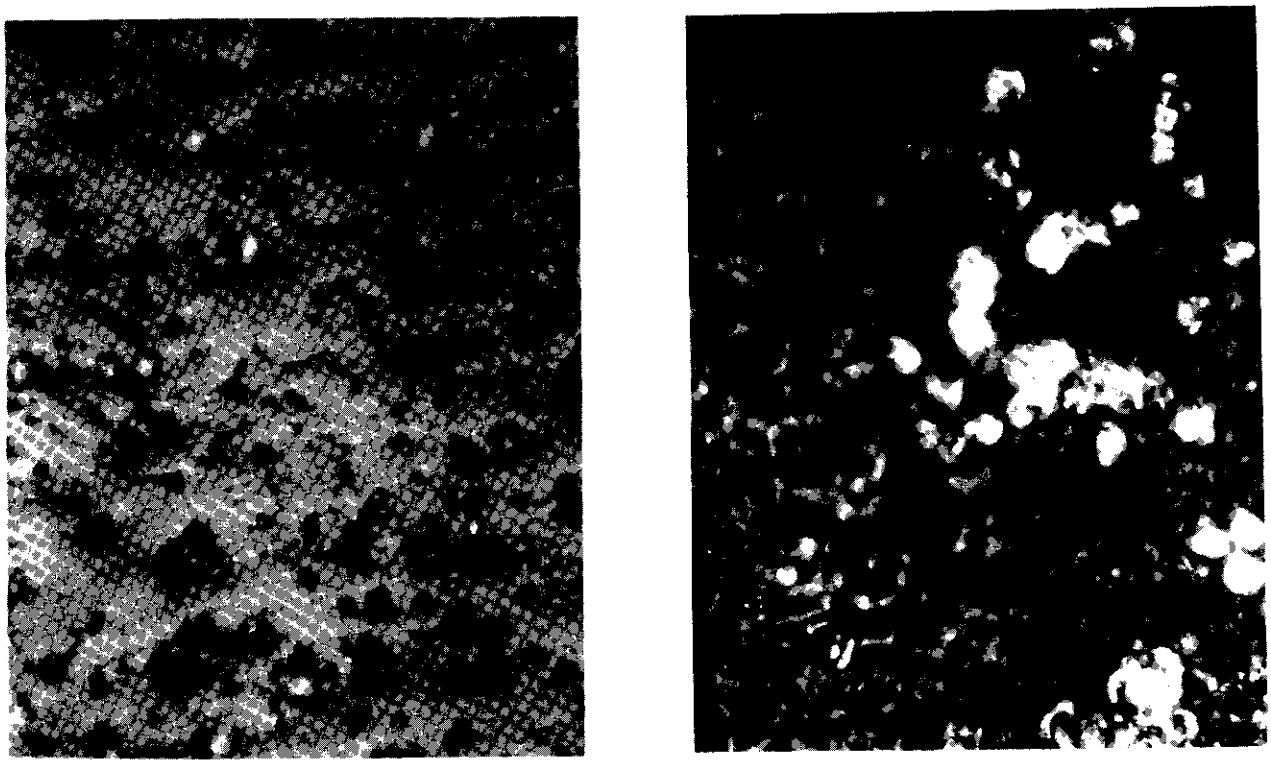

Before Heating to 2132°K

After Heating to 2132°K

Figure 28. TaN Surface Structure Before And After Heating To 2132°K (300X)

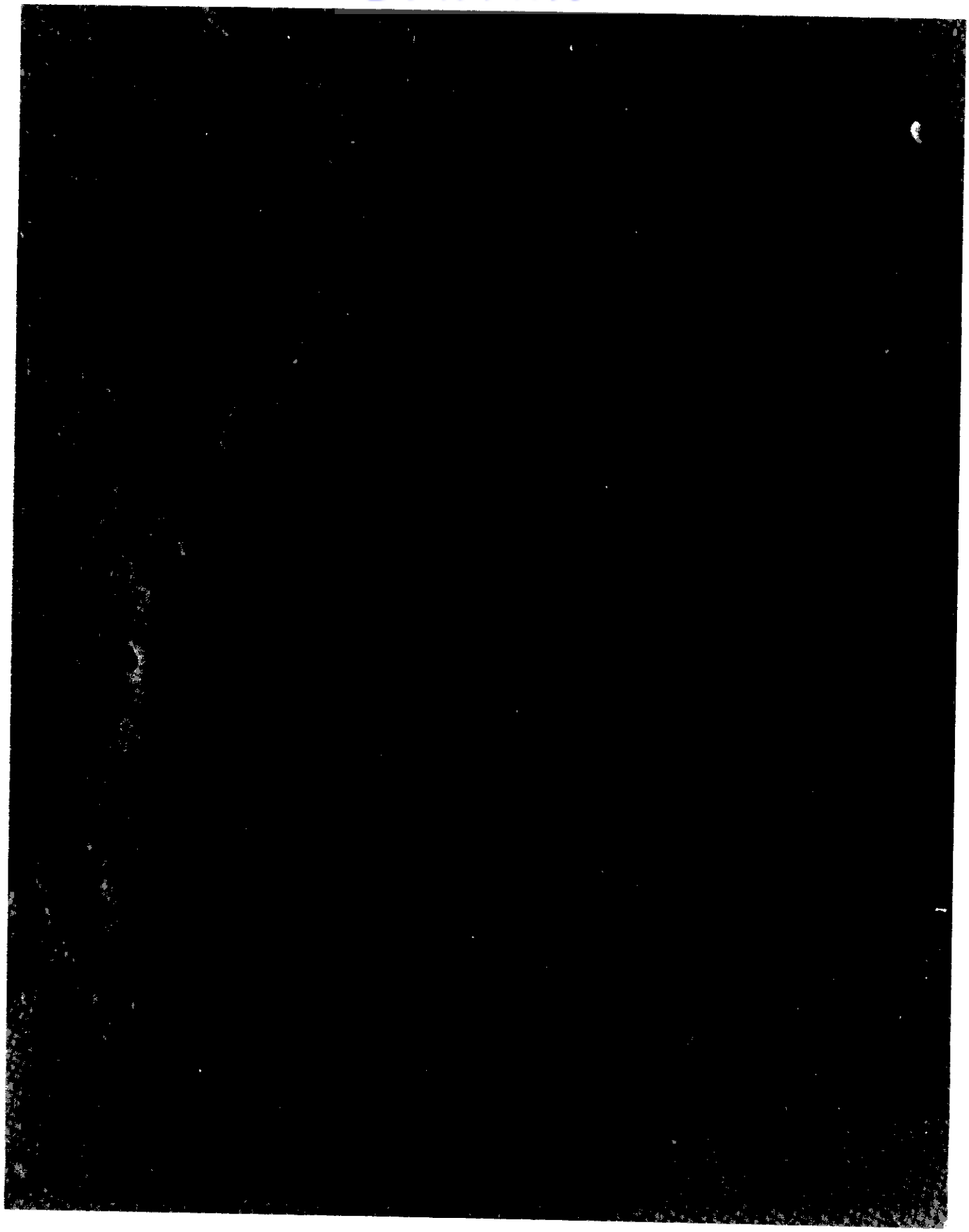

Figure 29. TaN Surface Structure Before Heating To 2132°K (56,000X)

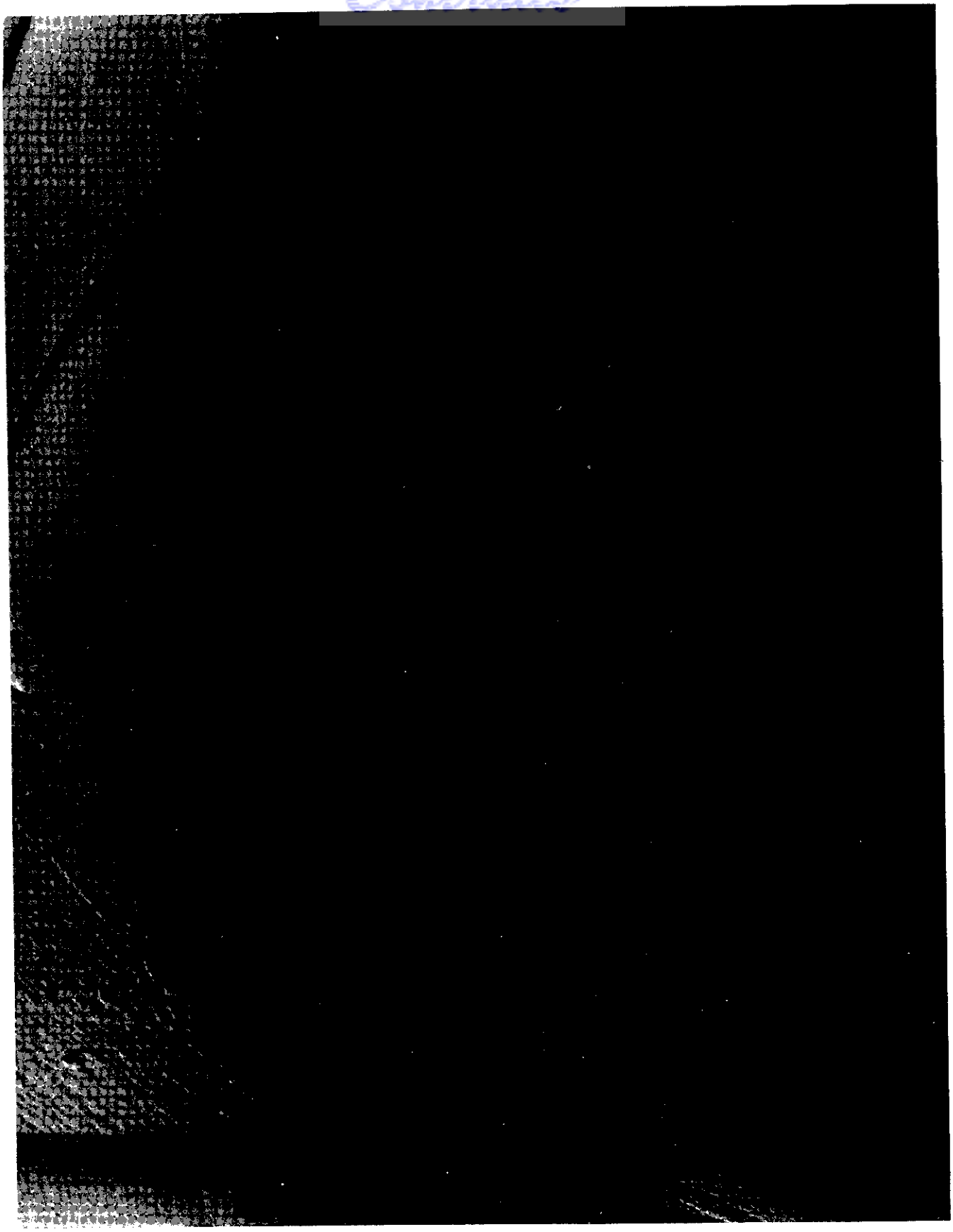

Figure 30. TaN Surface Structure After Heating to 2132°K (56,000X)

hexagonal boundaries into view.

Normal spectral emissivity measurements were made at 1648°K, 1851°K, 1956°K and 2132°K in argon at 1.5 atmospheres pressure. Figure 31 is a plot of emissivity as a function of wavelength. Below 1 micron there is only a small temperature dependency of emissivity which increases beyond 1 micron and becomes substantial at 4 microns. The crossover point, where emissivity is independent of temperature, appears to occur at 1.25 micron. Deviation of the 1648°K characteristic from the crossover point is thought to be caused by an initial modification of the polished surface structure. At 2132°K, emissivity is independent of wavelength beyond 1 micron. This latter behavior was also observed for measurements in an atmosphere of nitrogen.

Figure 32 is a plot of normal total emissivity computed from spectral data. Curve 1 is computed from data taken when the specimen was heated in an atmosphere of nitrogen and shows normal total emissivity to be virtually independent of temperature. This behavior was attributed to conversion of the surface to a fine granular structure induced by reaction to a higher nitrogen content. Curve 2 shows that when tantalum nitride is heated in an argon atmosphere, a positive temperature coefficient of normal total emissivity results at temperatures below 2000°K. Beyond 2000°K, values of emissivity are essentially the same for both atmospheres. An increase in normal total emissivity with temperature is typical of materials of this type and has been observed for the carbides of tantalum and zirconium, the borides of niobium, titanium, and zirconium and the nitrides of zirconium and hafnium. The calculated rate of change of emissivity with respect to temperature over the range of 1648°K to 2132°K for tantalum nitride is positive and 0.004 units per degree Kelvin.

2. Pyrolytic Graphite

Measurements of normal spectral emissivity have been made on pyrolytic graphite from both the "a-b" crystal plane and the "c" crystal plane. The specimens were machined from a sample of pyrolytic graphite made at the General Electric Space Sciences Laboratory by the pyrolysis of methane at reduced pressures. Rate of pyrolysis was controlled to insure a high density material free from delaminations and internal nucleation sites. A black body reference cavity, 0.020" diameter and 0.080" deep, was drilled in each specimen. For those specimens for which emissivity was measured from the surface parallel to the "c" plane, the cavity was cut with its axis parallel to the "as deposited" "a-b" plane. In specimens for which emissivity was to be measured from the "as deposited" or "a-b" plane, the axis of the cavity was perpendicular to the "as deposited" surface . Chemical composition of the pyrolytic graphite specimens on which emissivity measurements were run

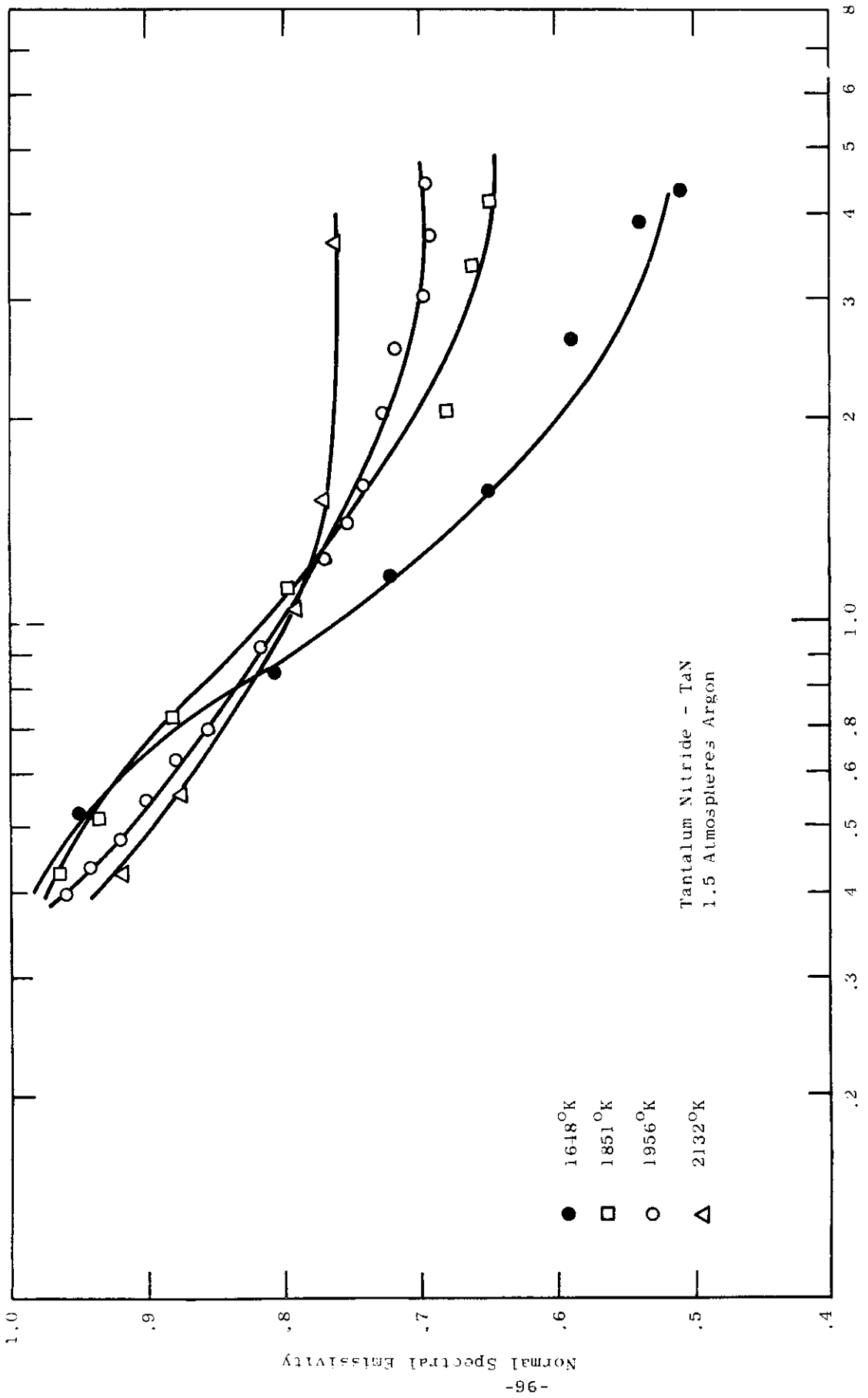

Figure 31. TaN - Normal Spectral Emissivity

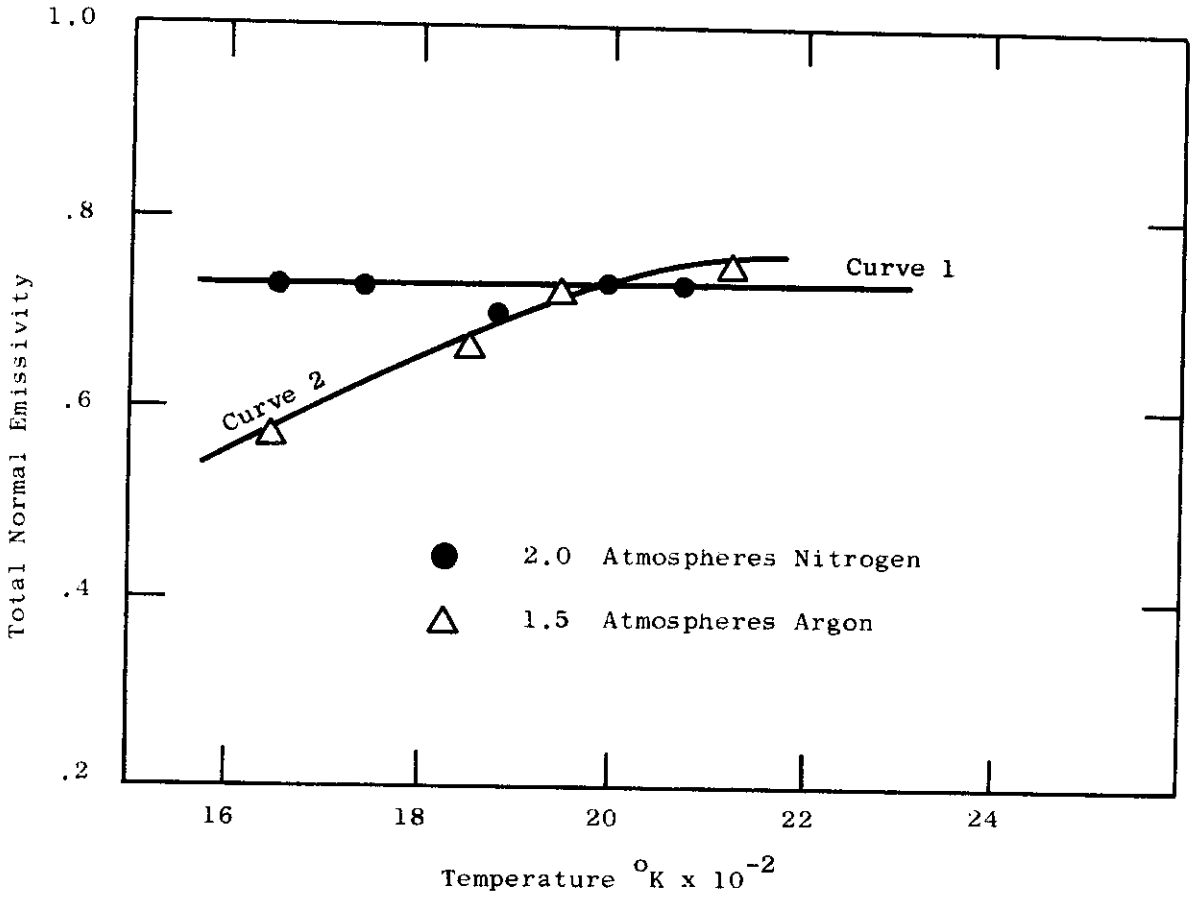

Figure 32. TaN - Normal Total Emissivity Vs. Temperature

is given in Appendix A, Table 32. The presence of a trace of silicon results from the pyrolyzing furnace. Photomicrographic structure of each crystallographic direction was established before and after emissivity measurement. Figure 33 shows a 300X photomicrograph of the "a-b" polished crystal plane before and after making emissivity measurements to 2735°K. After heating, there is evidence of re-orientation of crystal boundaries which could be the result of etching by traces of water vapor in the specimen chamber. This is seen more clearly by examining the electron microscope micrographs of the same surface. Figure 34 shows the polished surface, before heating, magnified at 76,500X and Figure 35, at 28,175X, shows the same surface after heating. The crater-like structure in the latter are boundaries at the top of a cone-shaped crystal, the apex of which is the crystal's nucleation site.

Measured values of X-ray lattice spacings for the "a-b" planes are given in Appendix B, Table 36. No change in these values was observed as a result of heating during emissivity measurement.

Weight and density measurements made before and after emissivity measurements (Table 20), indicate substantially stable conditions during emissivity measurement to 2735°K. The small loss of weight would, however, account for the observed etching of the "a-b" surface. The measured increase in density is probably due to degassing and densification of the specimen.

TABLE 20

WEIGHT AND DENSITY OF PYROLYTIC GRAPHITE
"a-b" Specimen

	Weight	Density
Before	.4062	2.194
After	.4030	2.200
Change	-.0032	+.006

Spectral emissivity measurements were made normal to the "a-b" polished crystal plane at temperatures ranging from 1590°K to 2735°K in 1.5 atmospheres of prepurified argon.

In this case, the specimen is oriented in the chamber such that the direction of maximum electrical and thermal conductivity is perpendicular to the axis of the RF concentrator and the specimen black body. This means that a temperature gradient could exist along the

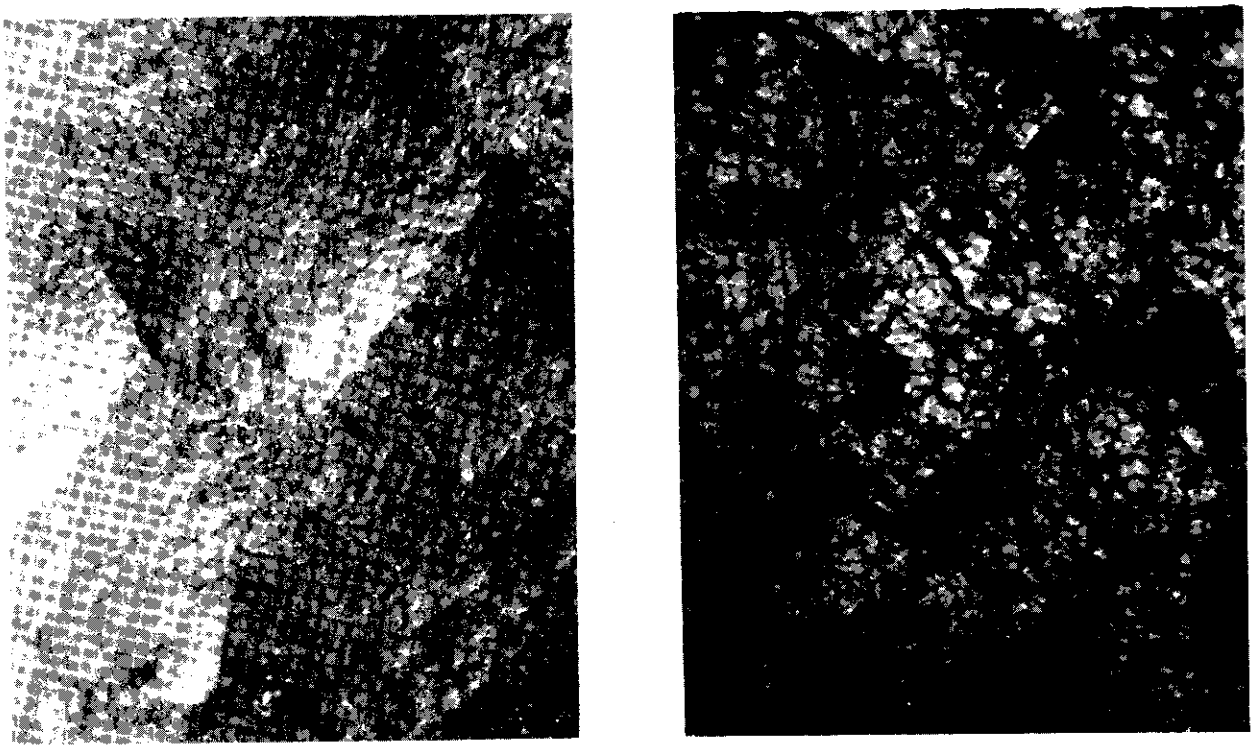

Before Heating to 2735°K

After Heating to 2735°K

Figure 33. Pyrolytic Graphite - Surface Structure Of "a-b" Crystal Plane Before And After Heating To 2735°K (300X)

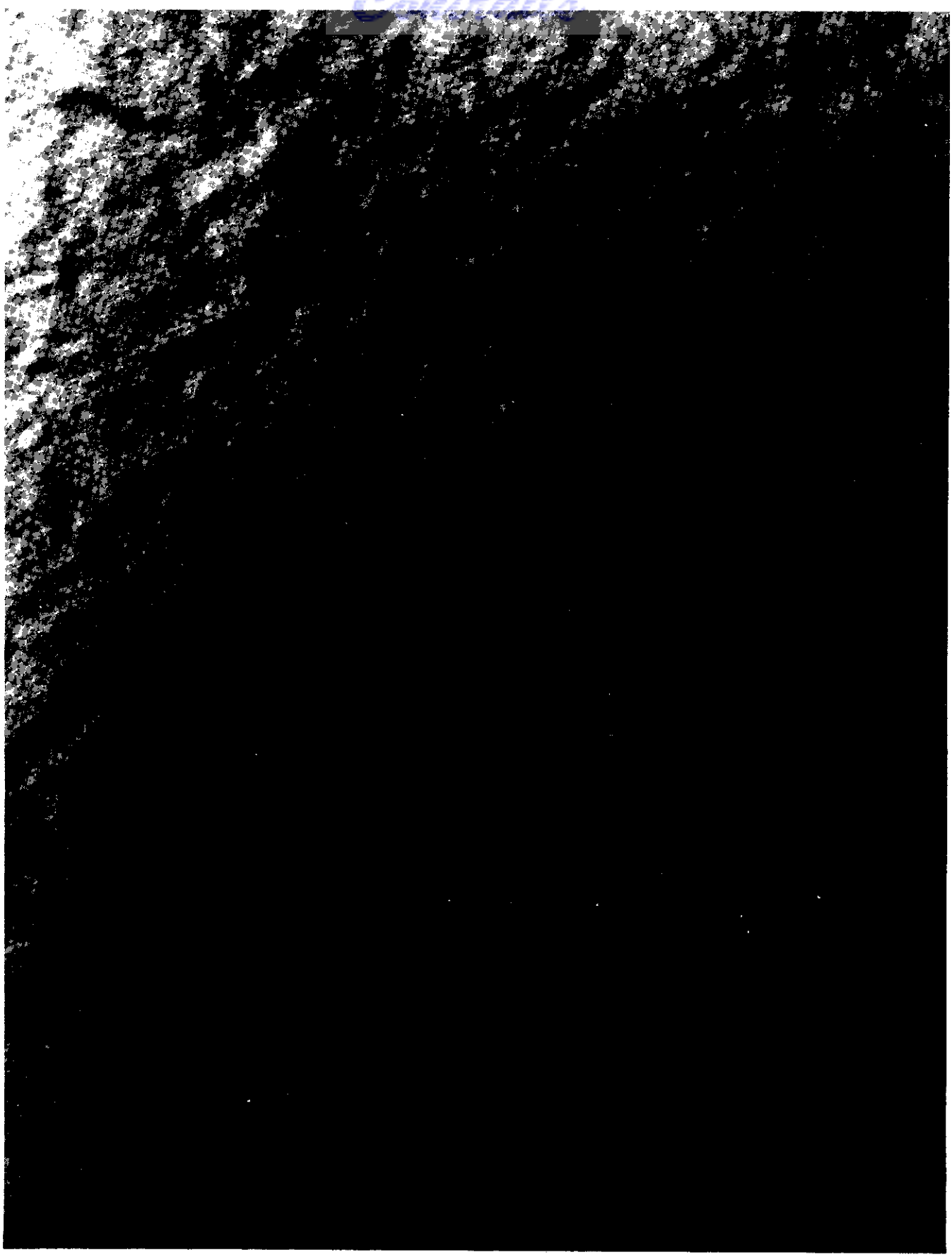

Figure 34. Pyrolytic Graphite - "a-b" Crystal Plane Before Heating To 2735°K (67,500X)

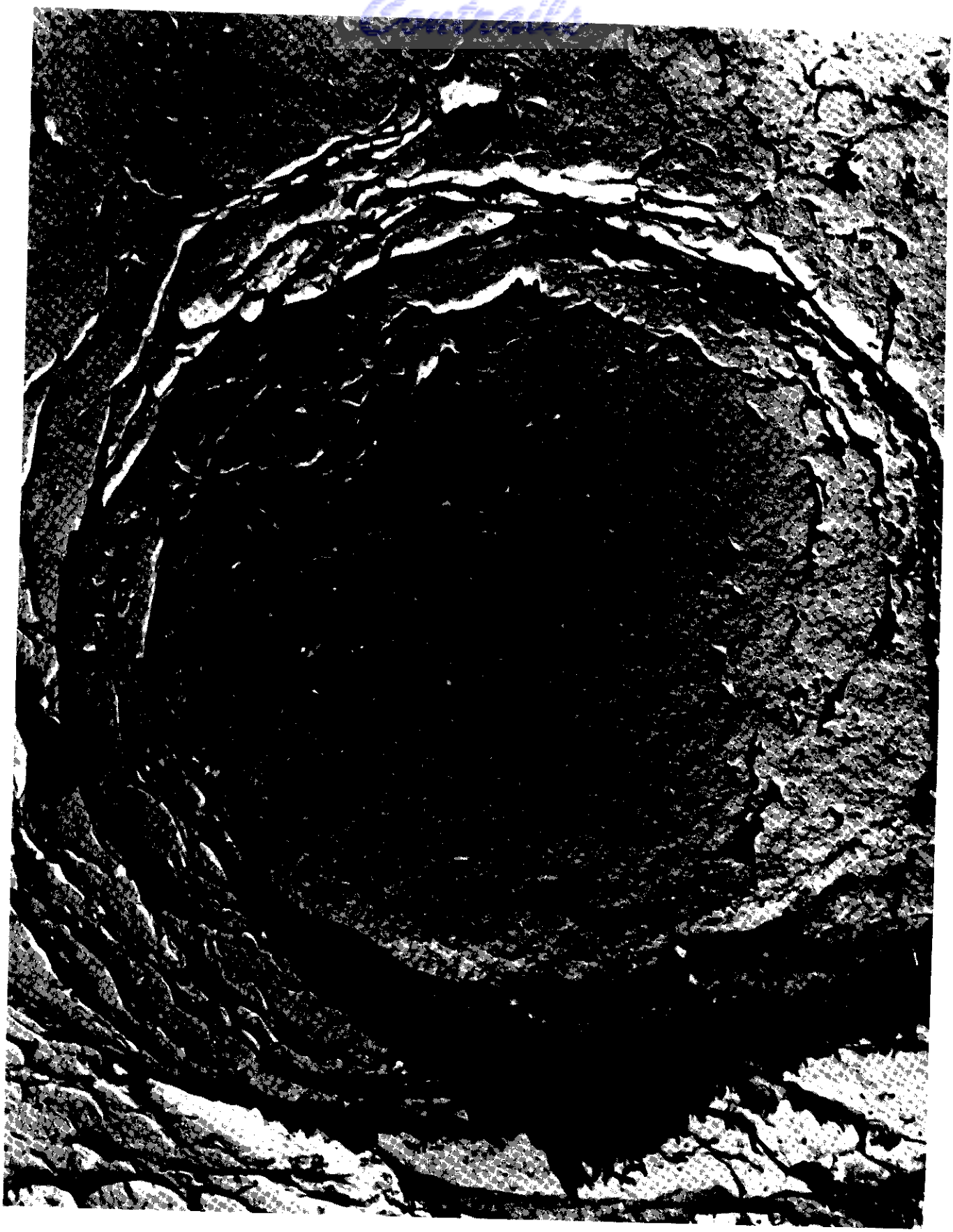

Figure 35. Pyrolytic Graphite - "a-b" Crystal Plane After Heating To 2735°K (28,125K)

black body reference cavity. The magnitude of the gradient could not be measured, but it was estimated to be not greater than 75°K. In addition, there is neat flow along radii of the "a-b" plane and the net effect of all this is for the black body to be at a higher temperature than an isotropic material at comparable surface temperatures. This could explain various points on the radiating "a-b" crystal surface indicate it to be completely isothermal.

Figure 36 shows normal spectral emissivity from the "as deposited" "a-b" plane at 2000°K. Measurements were run in an argon atmosphere. At this temperature, less than 7% of the total energy is radiated below 1 micron and 75% out to 4.5 microns. Calculation of normal total emissivity gives a value of 0.84 which is considerably higher than that determined for the polished surface. Figure 37 shows normal spectral emissivity for the same specimen after polishing. Here spectral emissivity is low below 1 micron and ranges between 0.05 and 0.12 at 0.65 micron and 0.35 to 0.62 at 3.5 microns over temperatures between 1611°K and 2735°K.

This result indicates that the "a-b" plane changes from a known black reflector in the visible bandwidth at room temperature, to a white reflector at temperatures above 1611°K. The fact that the black body reference cavity possessed a temperature gradient along its axis and achieved anisotropically induced higher temperatures under RF heating conditions, could account for the very low values of emissivity in the visible.

Figure 45, curve 1, is a plot of normal total emissivity of the "a-b" plane as a function of temperature. There is a substantial decrease of from 0.57 at 1590°K to 0.24 at 2735°K, and may, in part, be due to the temperature gradient along the black body reference cavity. Based on the observed changes in surface structure during measurement and the high value of 0.84 obtained for the unpolished surface at 2000°K, it would be reasonable to expect higher values over the range. It is possible that there are insufficient interband transitions of sufficient energy, especially in the high energy photon wavelength region, to provide high emissivity in the visible.

Measurement of normal spectral emissivity from the "c" plane was preceded by characterizing the material using methods previously outlined. Photomicrographs of the surface at 300X, shown in Figure 38, were made before and after heating in vacuum to 2054°K. A typical cone structure is evident with virtually no change taking place as a result of heating. Possibly the crystal boundaries become more definitive with heating, due to surface thermal migrations and etchings. Figure 39 is an electron microscope micrograph showing the polished surface structure

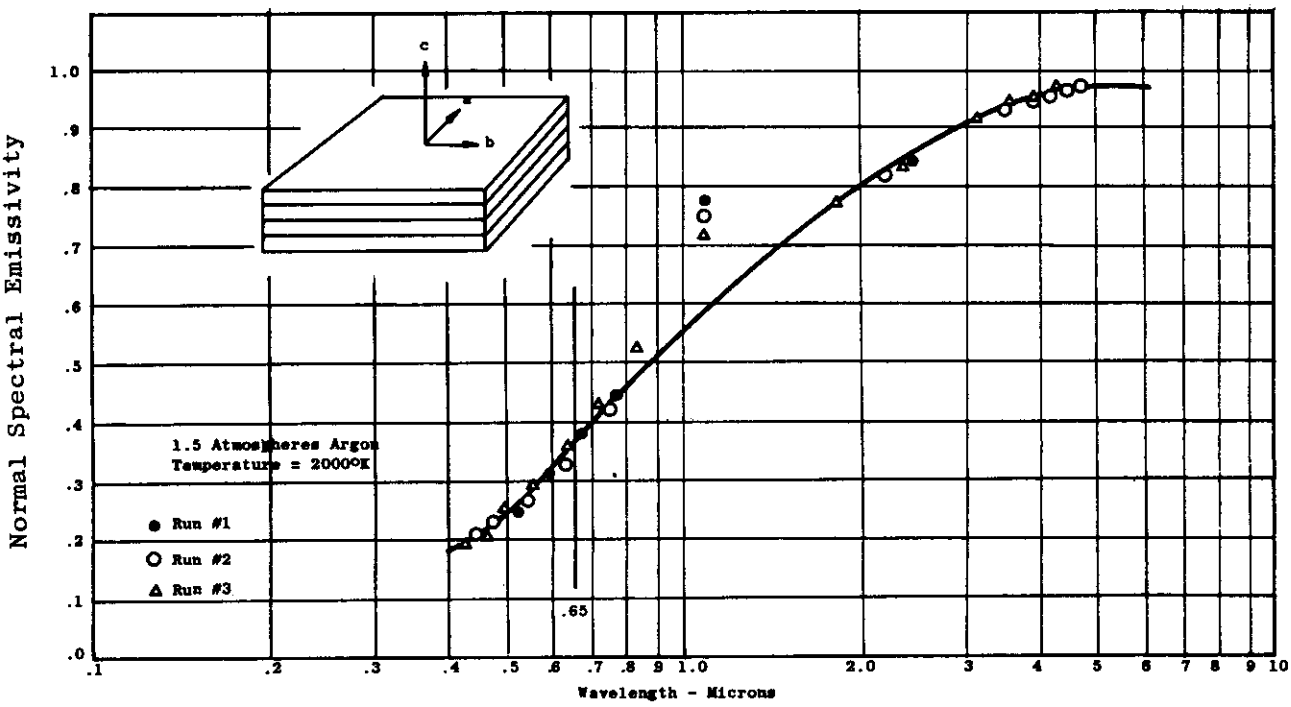

Figure 36. Normal Spectral Emissivity Of As-Deposited Pyrolytic Graphite - "a-b" Plane

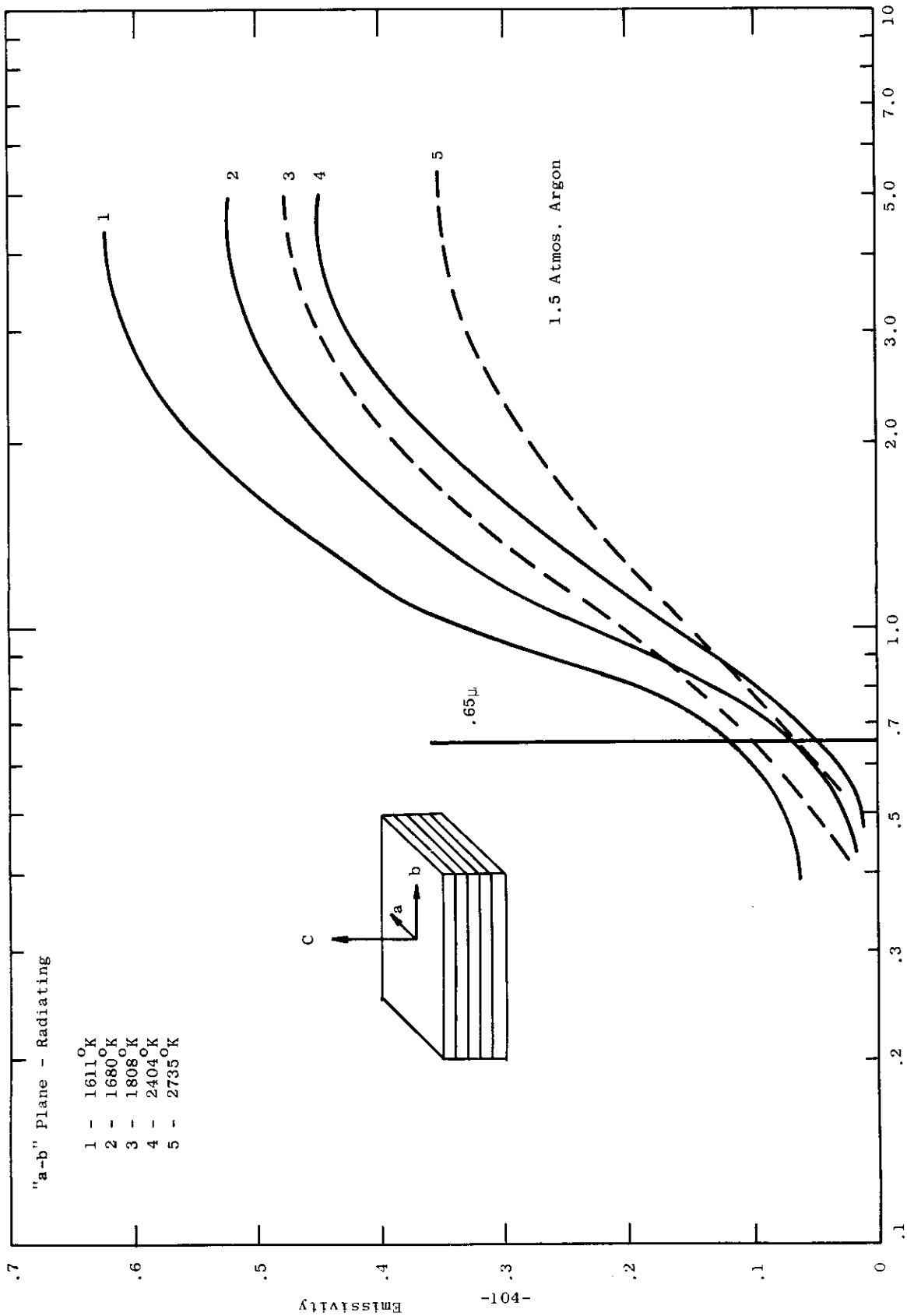

Figure 37. Normal Spectral Emissivity Of Polished Pyrolytic Graphite "a-b" Plane

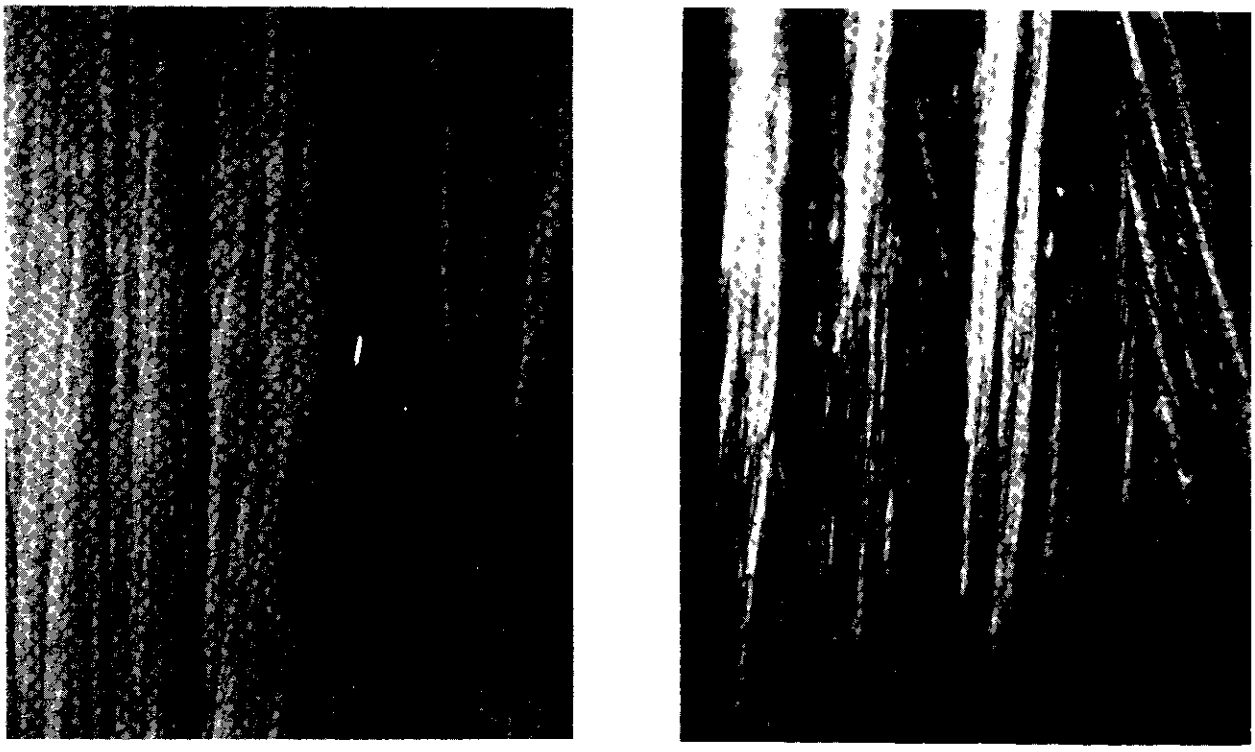

Before Heating to 2054°K

After Heating to 2054°K

Figure 38. Pyrolytic Graphite - Surface Structure Of "c" Crystal Plane Before And After Heating To 2054°K (300X)

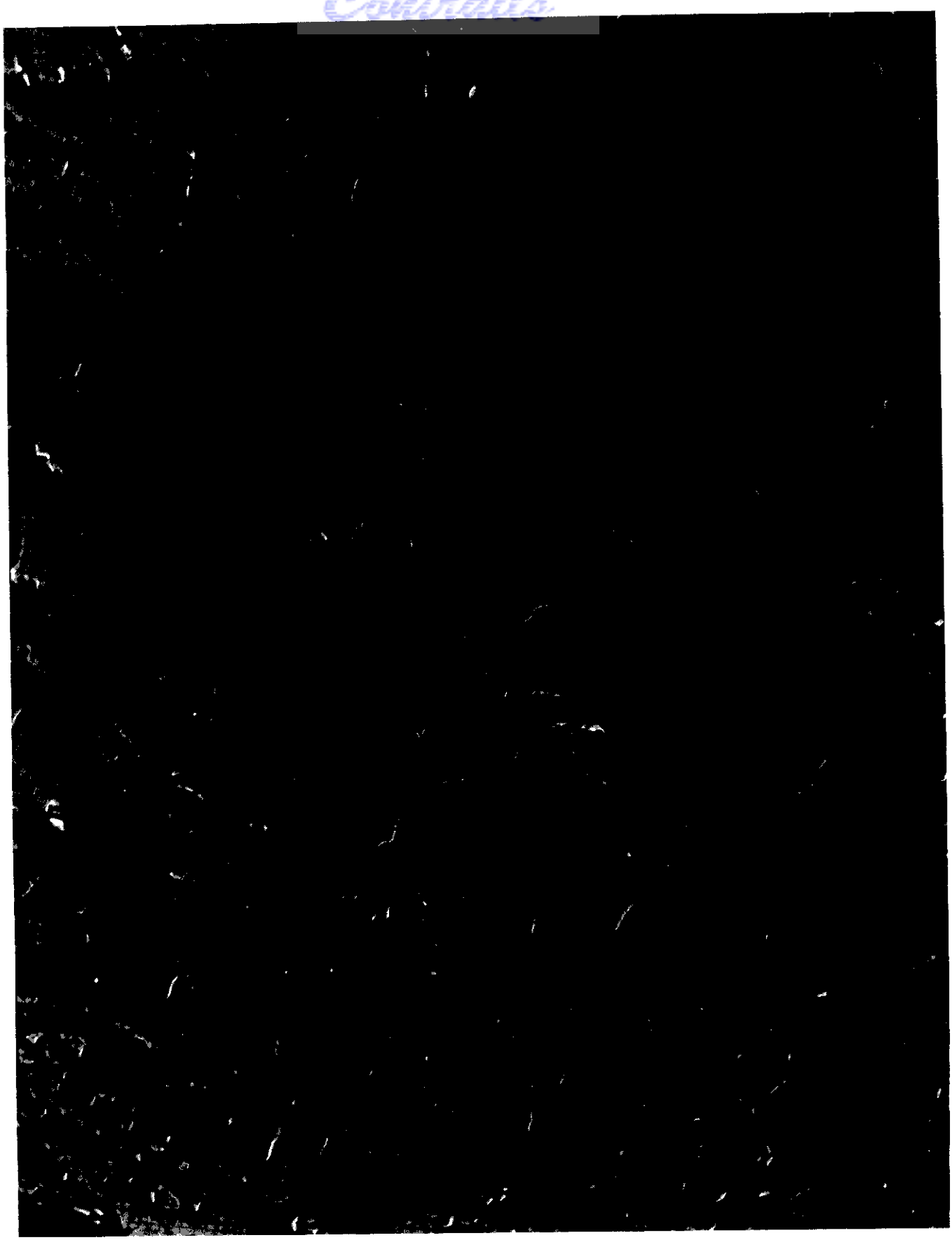

Figure 39. Pyrolytic Graphite - "c" Plane Before Heating (56,000X)

Figure 40. Pyrolytic Graphite - "c" Plane After Heating (67,000X)

before heating in vacuum to 2054°K . This can be compared with Figure 40, which shows the same surface after heating. A reordering of the surface takes place to conform with the edge structure of the "c" plane.

Weight and density measurements given in Table 21 again indicate stability during measurement. The observed small increase in density may be the result of densification and/or the diffusion of traces of tantalum from the heating sleeve holding the specimen.

TABLE 21

WEIGHT AND DENSITY OF PYROLYTIC GRAPHITE
"c" Specimen

	Weight	Density
Before	.4216	2.162
After	.4208	2.170
Change	-.0008	+.008

X-ray diffraction "d" spacings were measured with the beam incident on the "c" plane. The resulting "d" spacing values are given in Appendix B, Table 36. The same values were measured after heating in vacuum indicating that no basic changes in specimen structure took place during emissivity measurement.

Initial measurements of spectral emissivity were made in vacuum at temperatures of 1718°K, 1914°K and 2149°K. It was observed that temperature differences as great as 130°K existed across the surface of the specimen. Figure 41 is a sketch of surface temperature profile induced by the anisotropy of electrical and thermal conductivity in a directly coupled RF heated specimen. Figure 43 is a plot of spectral emissivity at 1718°K and 1914°K determined under conditions of the above temperature profile. It should, however, be pointed out that these temperatures were measured close to the point on the surface from which radiation is analyzed and while they remain constant under stabilized RF power input, values can only be estimated from temperature profile data.

To minimize temperature gradients, the specimen was placed in a tight-fitting tantalum sleeve. Figure 42 shows the resulting change in isotherms and an associated decrease of surface ΔT to 38°K. Spectral emissivity data, with the specimen mounted in the tantalum sleeve, for temperatures at 1409°K, 1531°K, 1882°K and 2054°K at pressures of

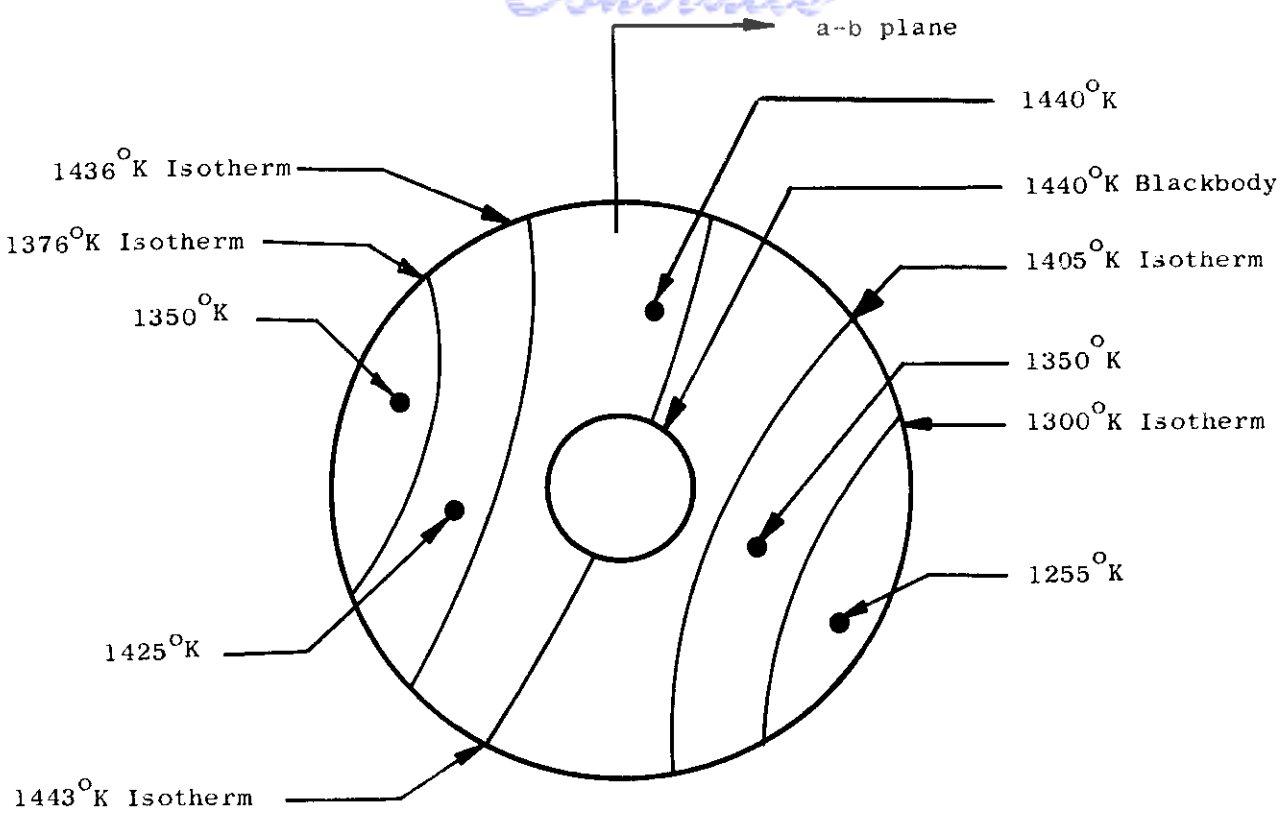

Figure 41. Temperature Profiles - Pyrolytic Graphite Specimen "c" Plane Radiating (Specimen Heated by Direct RF Coupling)

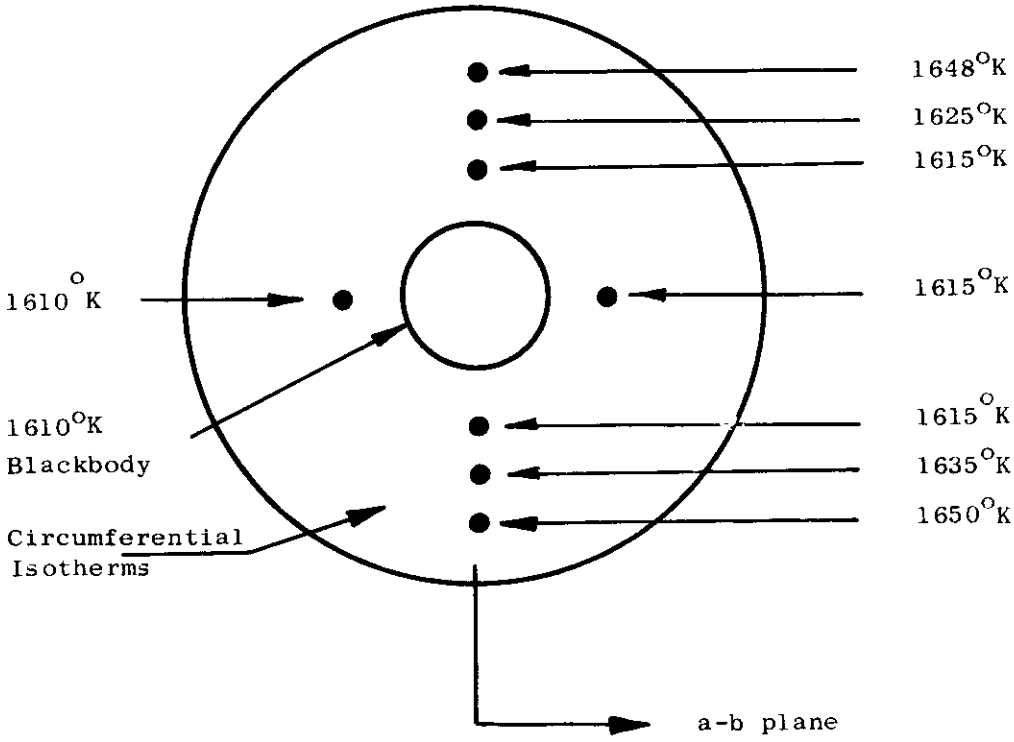

Figure 42. Temperature Profiles - Pyrolytic Graphite Specimen "c" Plane Radiating (Specimen Heated by Using Tantalum Sleeve Susceptor)

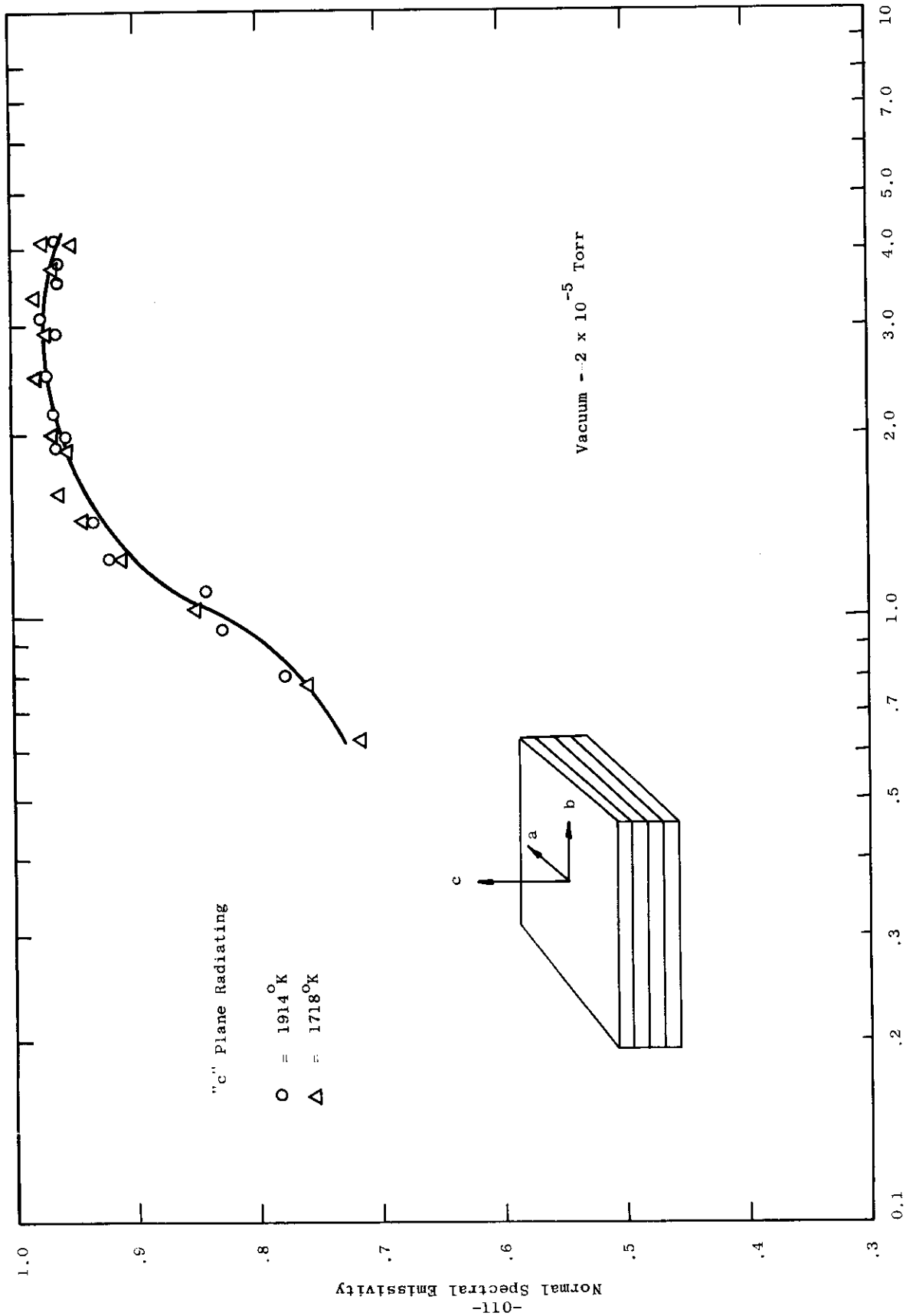

Figure 43. Normal Spectral Emissivity Of Pyrolytic Graphite "c" Plane Radiating (Specimen Heated by Direct RF Coupling)

less than 10^{-6} Torr, are shown in Figure 44. At these temperatures, emissivity increases from 0.4 micron to a maximum at 1.1 microns and then decreases beyond this wavelength. Also, emissivity decreases with increased temperature. The increase at the shorter wavelength may be caused by interband transitions while the decrease measured in the infrared is probably due to the free charge carriers. Similar effects are responsible for the decrease in emissivity of metals and doped semiconductors in the infrared.

Normal total emissivity computed from spectral data for the "c" plane is given in Figure 45. Curve 2 is a plot of values measured while RF-heating the specimen in a tantalum sleeve, and curve 3 for direct RF heating.

Total emissivity values differ by about 0.12 unit maximum over the temperature range. In each case, there is a decrease in emissivity as temperature increases. For the directly-heated specimen, total emissivity ranges from 0.93 at 1718°K to 0.75 at 2319°K and, when heated in a tantalum sleeve, from 0.81 at 1409°K to 0.69 at 2225°K.

Comparing emissivity of the "c" plane (Curves 2 and 3) with emissivity from the "a-b" plane (Curve 1) there is substantial anisotropy of emissivity with the highest values being measured from the "c" plane or the surface perpendicular to the direction of highest thermal and electrical conductivity. While this result would be predicted on the basis of theory, the low values of emissivity for the "a-b" plane, especially above 1800°K, are doubtful.

3. Single Crystal Tungsten - 200 Plane

Preceding emissivity measurements, a specimen of single crystal tungsten having the chemical composition given in Appendix A, Table 33, was prepared in the form of a rod 1/2-inch long and 1/4 -inch in diameter. A black body reference cavity was ultrasonically drilled along the specimen axis with the axis normal to 200 crystal plane. There was no apparent generation of crystallites as a result of this operation. A photomicrograph of the polished surface at 300X is shown in Figure 46, along with the same surface after heating to 2639°K in an atmosphere of argon. There is no evidence of structural change or conversion to a polycrystalline form. In fact, the specimen, if anything, increased in reflectivity as a result of thermal polishing during heating. This is somewhat verified by examining electron microscope micrographs. Figures 47 and 48 show the surface structure of the 200 plane at 60,000X before and after heating respectively. There is evidence of dislocations and crystal defects on the polished surface before heating which became less prominent after heating. However, a bead-like structure does develop which may cause some scatter of emitted radiation but should have little

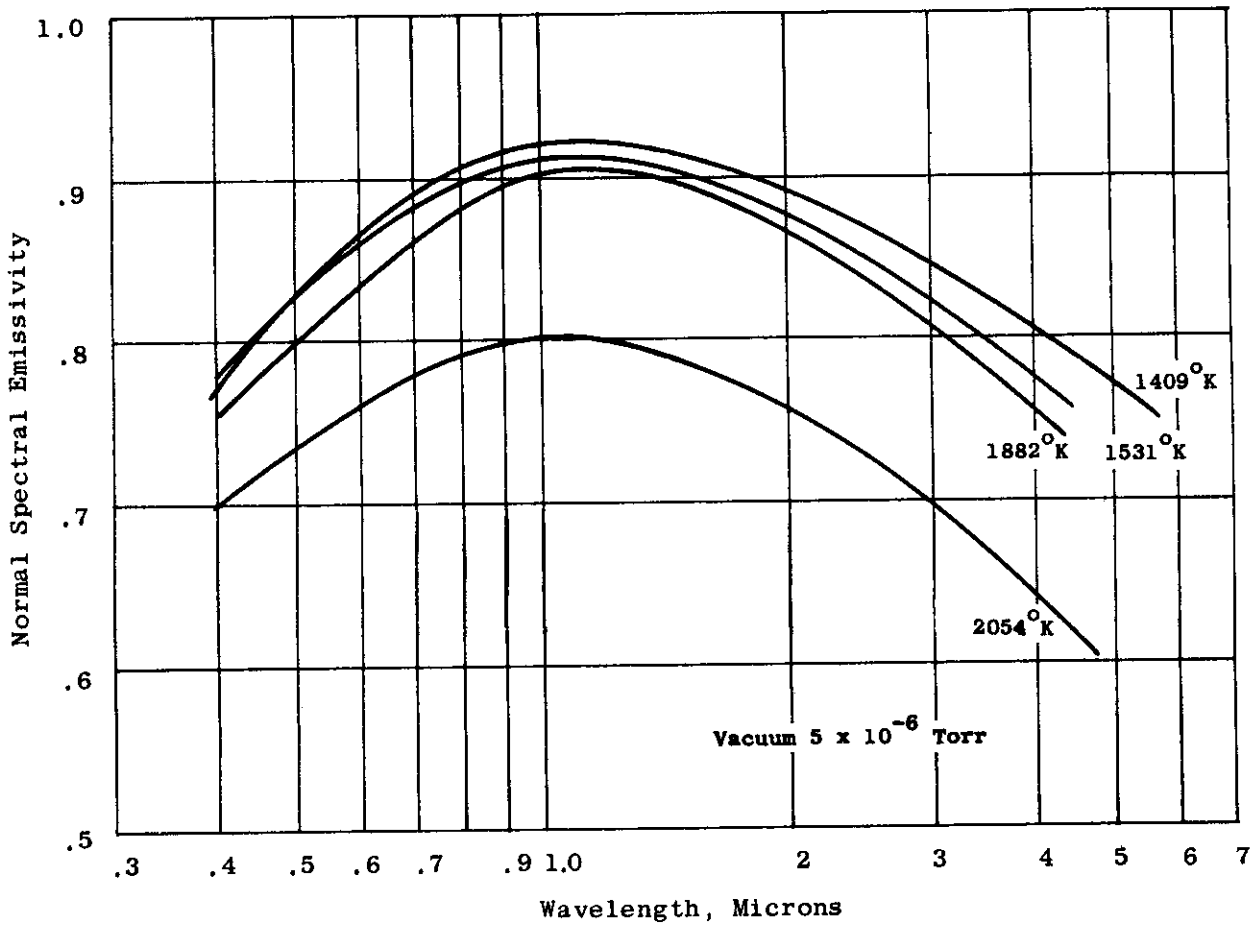

Figure 44. Normal Spectral Emissivity of Pyrolytic Graphite - "C" Plane Radiating (Specimen Heated in Tantalum Sleeve)

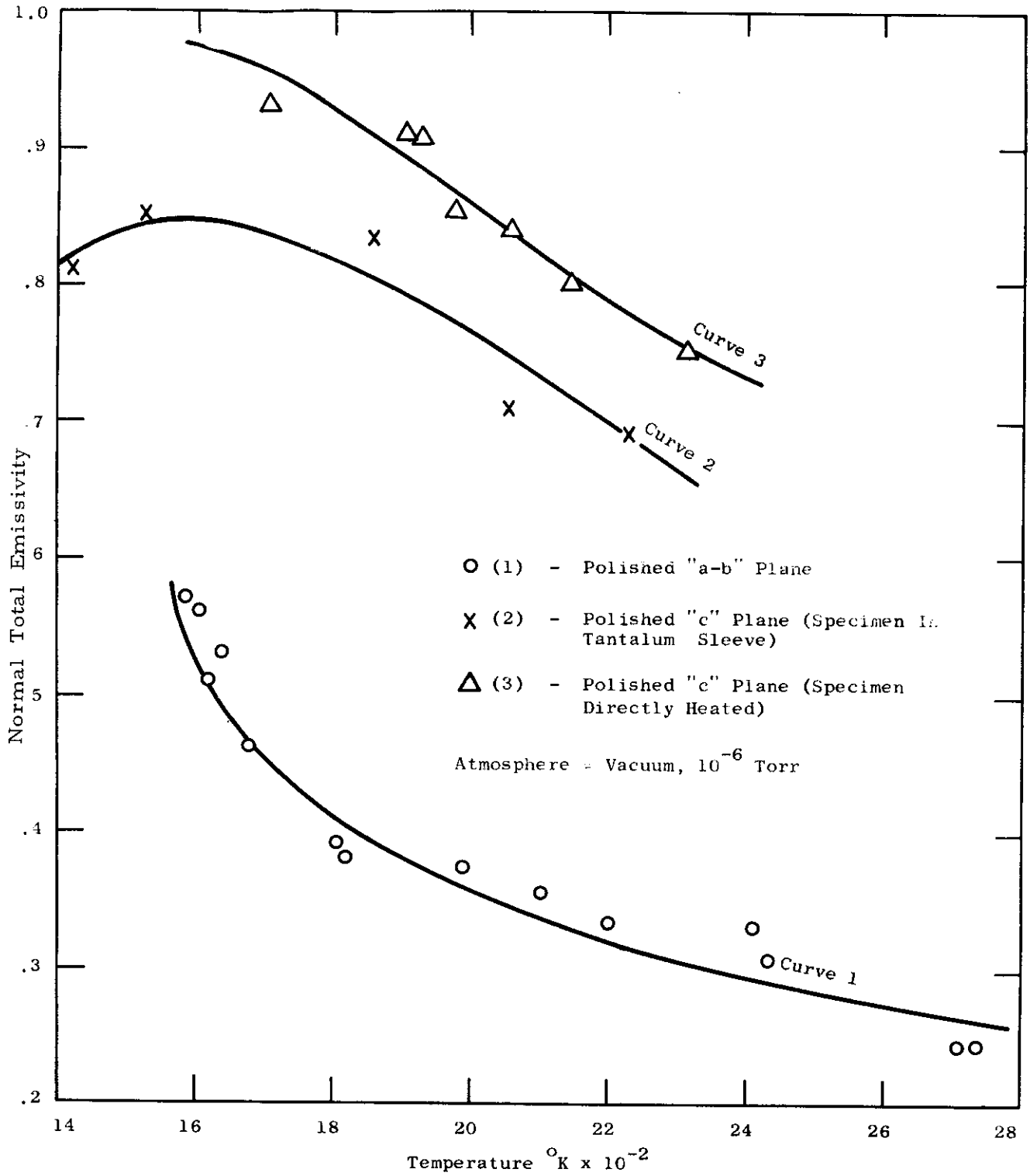

Figure 45. Comparison of Normal Total Emissivity vs Temperature for Pyrolytic Graphite with "a-b" and "c" Orientation

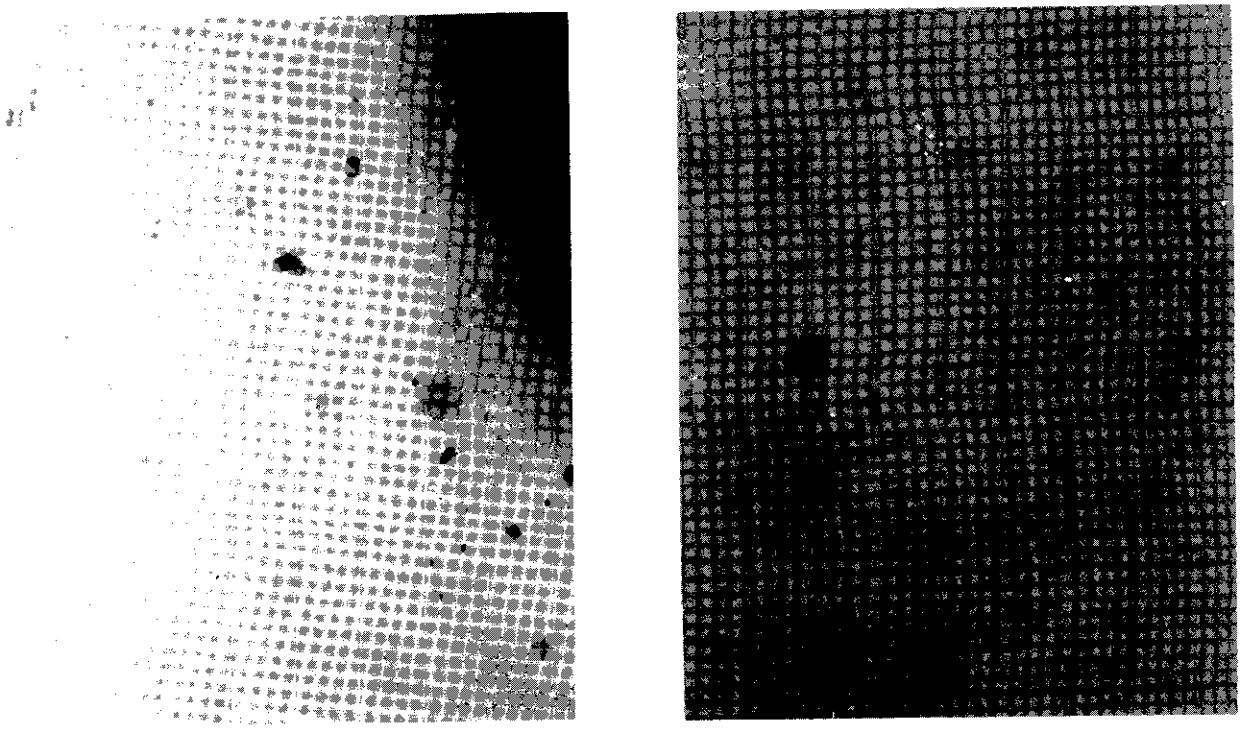

Before Heating
to 2639°K

After Heating
to 2639°K

Figure 46. Single Crystal Tungsten Before And After Heating (200 Plane, 300X)

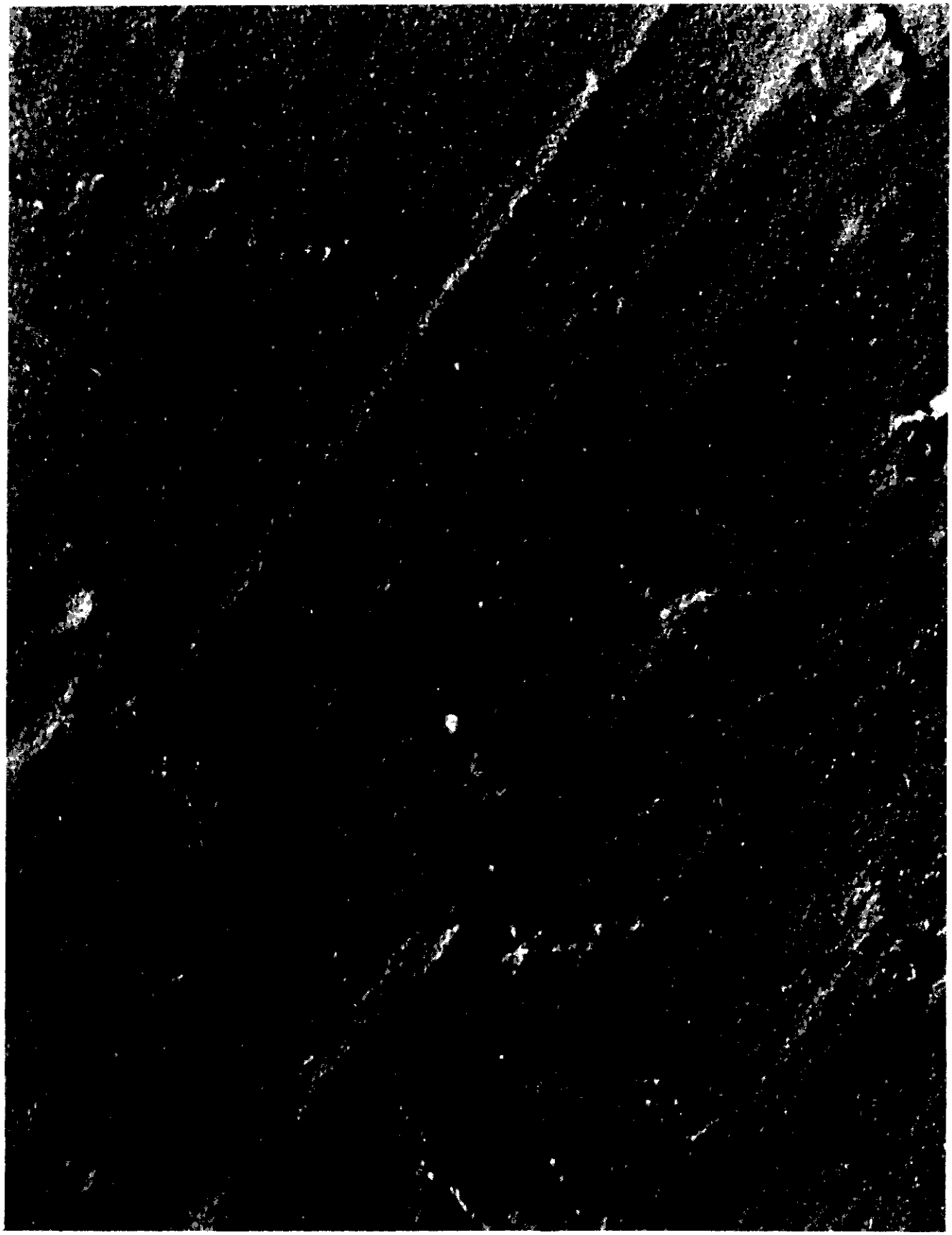

Figure 47. Single Crystal Tungsten Before Heating (60,000X)

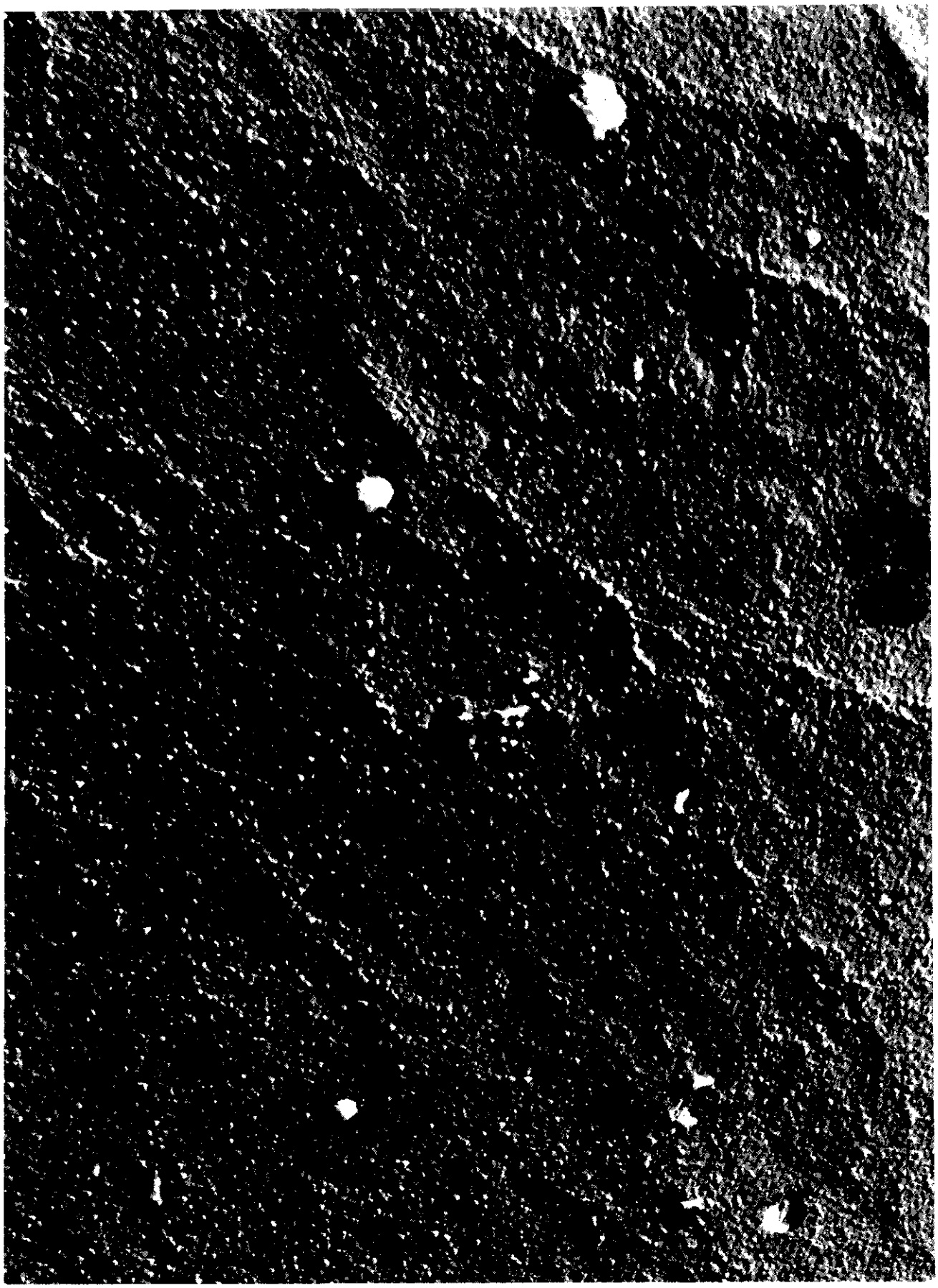

Figure 48. Single Crystal Tungsten After Heating (60,000X)

effect on emissivity. If anything, slightly high values of total emissivity could be expected. X-ray lattice "d" spacing, given in Appendix B, Table 37, determined before and after heating, indicated that no changes in crystal lattice structure took place as a result of heating to 2639°K. Weight and density measurements were made before heating but because the specimen sintered to the ceramic holder, measurements to determine possible changes after heating were not made.

Following characterization, the single crystal tungsten specimen was placed in the test chamber being supported by means of a ceramic holder with the 200 plane radiating into the monochromator slit. Processing was carried out in accordance with previously described procedures. Spectral emissivity measurements were made over a wavelength range from 0.4 micron to 5 microns at temperatures of 1605°K, 2140°K, 2419°K and 2639°K.

Figure 49 shows a plot of emissivity as a function of wavelength. Here, the crossover point, where emissivity is independent of temperature, occurs at 1.15 microns. DeVos [5] has shown that this point falls at 1.3 microns for polycrystalline tungsten. In addition to this difference, single crystal tungsten shows spectral values of emissivity over the bandwidth studied to be slightly lower than for polycrystalline tungsten. The thermal etching of polycrystalline tungsten that normally takes place at high temperature could account for this result. Any slight formation of oxide films on the surface of tungsten causes low values of spectral emissivity in the visible and higher values in the infrared which when integrated over the bandwidth could give values of total emissivity that are comparable to clean tungsten at equivalent temperatures.

Figure 50 is a plot of normal total emissivity computed from spectral data, showing that from 1600°K, emissivity increases at a rate of 0.03 units per degree to 2420°K and remains constant from this temperature out to 2639°K. The two points shown for polycrystalline tungsten were computed from spectral data employing the same emissometer used for the measurements made on single crystal tungsten. Again, slightly higher values of normal total emissivity are indicated for polycrystalline tungsten.

D. Conclusions

Instrumentation developed in the early stages of this project, and improved during its span, has resulted in a technique for measuring normal spectral emissivity at temperatures in excess of 1400°K. The following are general remarks on advantages and limitations of the technique.

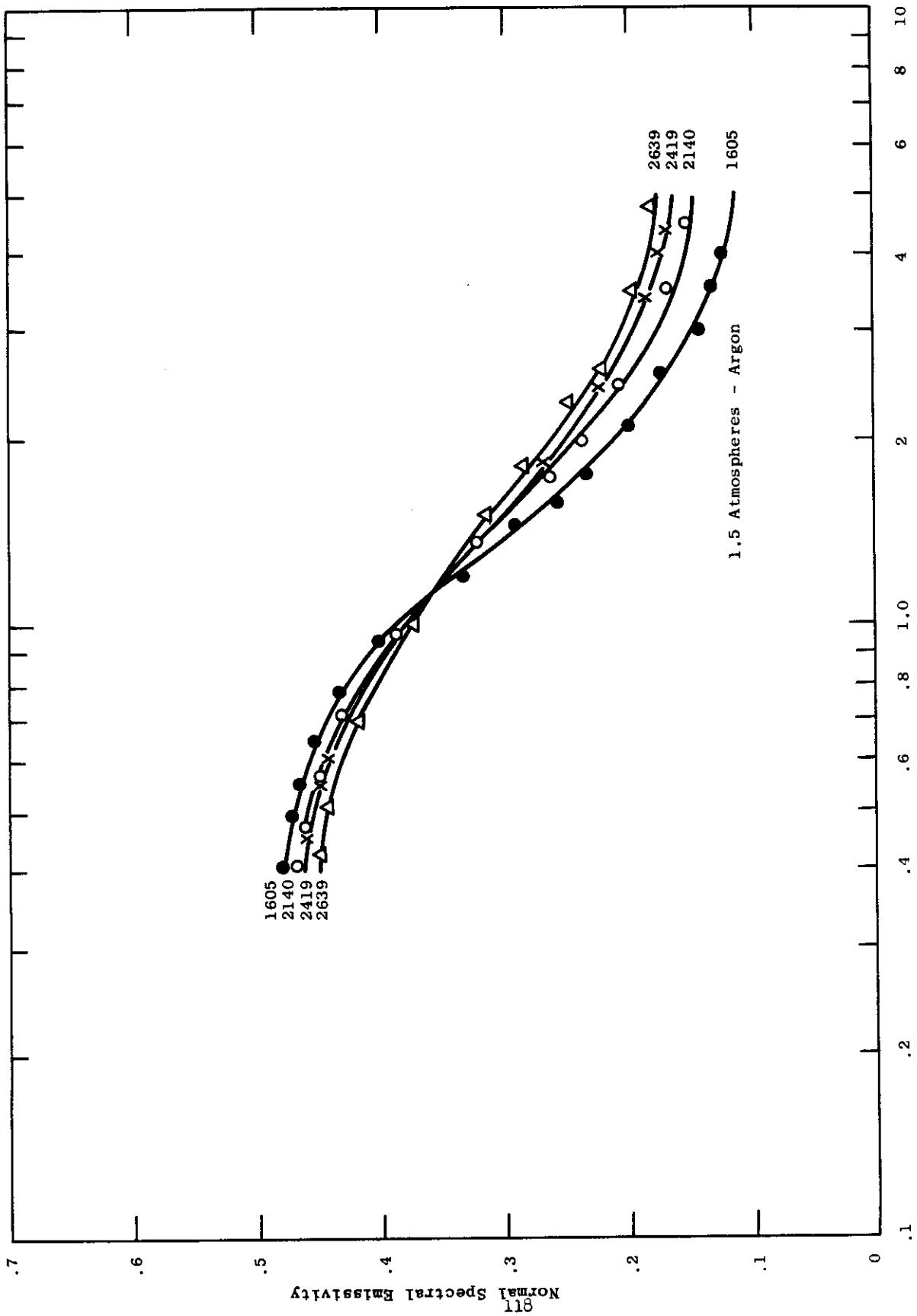

Figure 49. Normal Spectral Emissivity Of Single Crystal Tungsten (200 Plane)

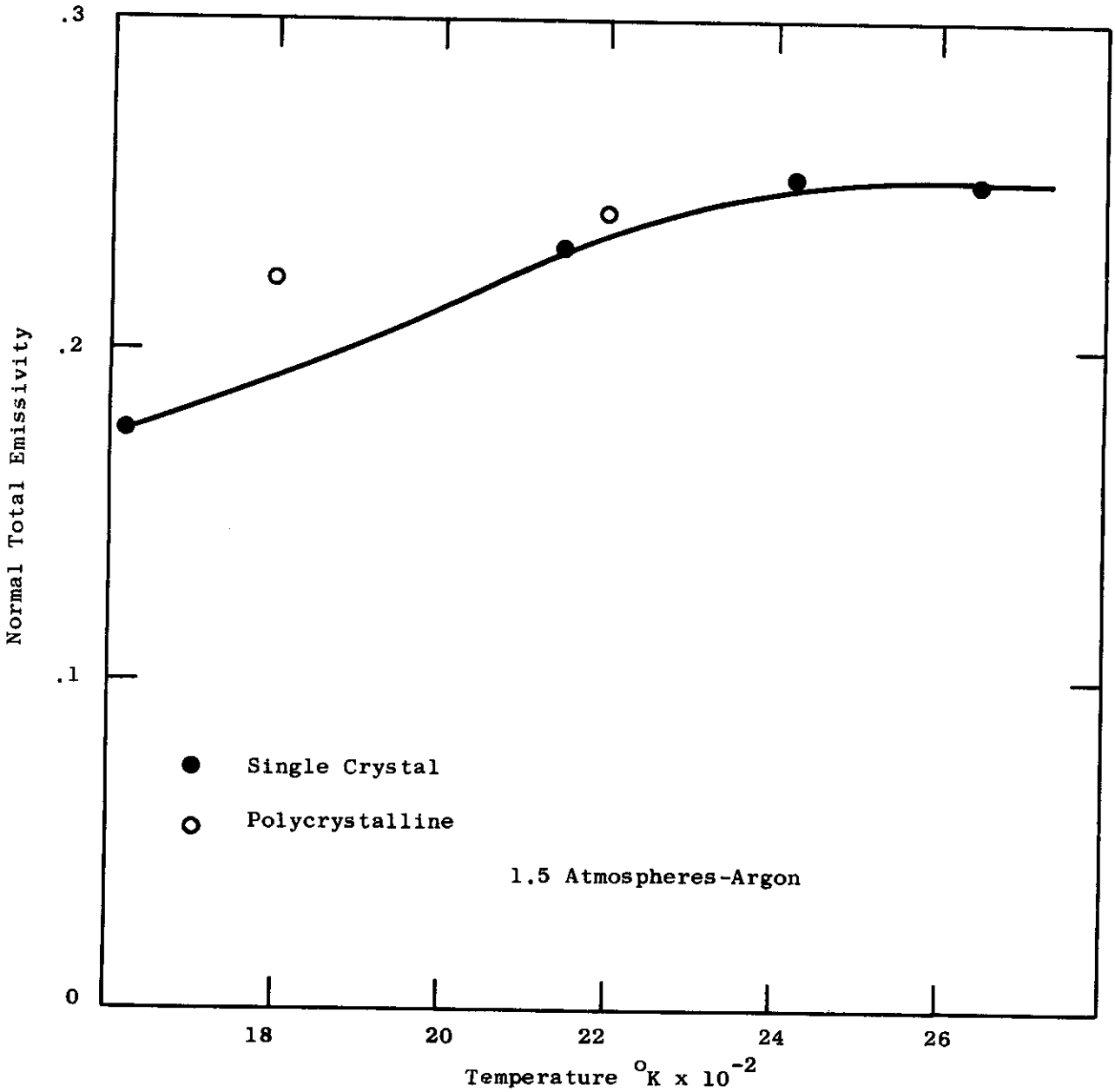

Figure 50. Normal Total Emissivity Of Single Crystal And Polycrystalline Tungsten (200 Plane)

1. Specimen

- The required specimen is small. It need not exceed 0.5" in length and can range from 0.125" to 0.250" in diameter.

- Specimens must be optically opaque and stable at temperatures in excess of 1400°K in vacuum or inert atmospheres.

- Because of RF heating considerations, it is preferable that the specimen be isotropic and a good electrical conductor. Although it is possible to study non-conductors by inserting them into a non-reactive refractory metal sleeve, greater difficulty is encountered in establishing uniform stable specimen temperatures. For strongly anisotropic materials, a modified specimen design and alternative methods of heating are suggested, such as radiative heating using solar or arc image power sources.

- Blackbody reference cavity is intrinsic within the specimen, thus assuring that true temperatures of the specimen surface and the blackbody are the same. The design of this and other types of blackbody cavities have been analyzed by DeVos [5].

- Specimen geometry is such that surfaces can be easily polished, etched, photographed and otherwise conveniently characterized.

2. Specimen Chamber

- Permits heating specimen in vacuum of 10^{-6} Torr or any desired gas at up to 2 atmospheres pressure.

- The chamber contains a water-cooled RF concentrator into which RF energy from an external coil is coupled. Without the concentrator, only a fraction of RF flux energy would be effective in inducing a current into the specimen. The concentrator, therefore, acts as a tank transformer to provide a means of attaining specimen temperatures up to 3500°K. Increased flux currents through the specimen are achieved by a factor equal to the ratio of the outside coil cross-sectional area to the cross-sectional area of the concentrator hole and also the area of this hole to the cross-sectional area of the specimen.

- The chamber can be fitted with a lens compatible with spectral band pass requirements. Some back reflection to

the specimen from the lens and chamber walls is encountered but is not a significant error at high temperature. This can be minimized by coating the chamber walls and non-transmitting area of the lens with a good absorber and maintaining surface temperatures below 100°C.

- Condensation of distillates from the specimen on the CaF_2 lens decreases energy intensity to detectors but has essentially no effect on emissivity since the optical path is common to both the surface and blackbody reference cavity. However, such deposits do substantially effect temperature measurements and should therefore be avoided.

3. Optics

- Blackbody radiation from a 0.010" diameter area coaxial with the 0.020" diameter black body reference cavity passes into the monochromator. Thus, scattering from circumference edges is eliminated. Radiation from an equivalent area on the surface of the specimen is measured. It is evident that changes in structure of this surveillance area could be different from the average for the surface and thus introduce uncertainties as to scattering effects, degree of normalcy of radiation and the intensity of intersurface multiple reflections.

- Possible sources of systematic errors in the transfer optics have been minimized by making distances between spherical mirrors equal in order to eliminate spherical abberation. In addition, the spherical mirrors are adjusted so that the planes containing rays leaving and striking the centers of spherical mirrors are inclined 90^{o} with respect to each other and the angles of the beams leaving and striking each spherical mirror are the same for all spherical mirrors. This insures the elimination of astigmatism for an image point on the optical axis.

4. Electronics

- Signal-to-noise ratio is maintained at a minimum by maintaining complete synchronization between the chopper and common cam shaft driven microswitches that activate the oscillating mirror. In addition, it is important that the optical axis be coincident with that of the black body through proper positioning of oscillating mirror. Also, a suitable low noise level is maintained in first stage

amplifiers by operating filaments at reduced current and applying minimum screen grid and plate voltages. Shielding from the induction furnace oscillator has been found important to the reduction of noise.

5. Summary of Sources of Error

- Systematic error sources are attributable to non-blackness of the black body referenced cavity in the specimen, temperature gradients on the specimen surface and along the blackbody axis, differences in transmission between the blackbody and surface radiation signal through the optical system, light scattering and nonlinearity of amplifiers, detectors and recording potentiometer.

- Random errors can be attributed to temperature drifts in the specimen, changes in transmission and reflectivity of optics through which temperature is measured and random detector noise.

6. Spectral Bandwidth Considerations

- In measuring normal spectral emissivity over a wavelength bandwidth of from 0.4 to 5 microns, a variable percentage of the total radiation is included depending upon the temperature of the specimen. For example, at 1400°K 81% of the total spectral energy is dealt with; at 2000°K it is 91%; and at 3000°K it is 97% of the total. In computing normal total emissivity values, it is assumed that emissivity is constant beyond 5 microns and equal to the 5 micron value.

E. References

1. Coffman, J.A., et al, "Carbonization of Plastics and Refractory Materials Research," WADD Technical Report 60-646 Part I, (February 1961)

2. Coffman, J. A., et al, "Carbonization of Plastics and Refractory Materials Research," WADD Technical Report 60-646, Part II (January 1963)

3. Kibler, G. M., et al, "Carbonization of Plastics and Refractory Materials Research, Volume 2 Refractory Materials", WADD Technical Report 60-646, Part III, Volume 2, (March 1964)

4. Blau, H. H., et al, "High Temperature Thermal Radiation Properties of Solid Materials", AFCRC, TN-60-165, March 31, 1960.

5. DeVos, J.C. "A Determination of the Emissivity of Tungsten Ribbon", Physica 20 690, 1954.

APPENDIX A

CHEMICAL COMPOSITION

Tables 22 and 23 give the chemical composition of materials investigated earlier and reported, except for composition, in reference 1.

Tables 24 through 30 give the chemical composition of materials investigated earlier and reported, except for composition, in reference 2. Tables 31 through 33 cover materials investigated in the past year and reported herein. (Composition of materials studied in the third year were previously reported in reference 3.)

TABLE 22

TUNGSTEN

POLYCRYSTALLINE

BY SPECTOGRAPHIC ANALYSIS

PARTS PER MILLION

IRON ----------10

MOLYBDENUM----30

TUNGSTEN -----Balance

(NOTE: All other trace elements not detected.)

TABLE 23

ZIRCONIUM CARBIDE

BY WET CHEMICAL ANALYSIS

ZIRCONIUM ------ 85.96%

CARBON --------- 14.17%

BY SPECTOGRAPHIC ANALYSIS

ALUMINUM ------- 0.003%

CHROMIUM ------- 0.002%

IRON ----------- 0.01%

HAFNIUM -------- 0.1%

MAGNESIUM ------ 0.001%

MANGANESE ------ 0.001%

MOLYBDENUM ----- 0.005%

SODIUM --------- 0.001%

SILICON -------- 0.002%

TITANIUM ------- 0.005%

POTASSIUM ------ 0.001%

(NOTE: All other elements not detected.)

TABLE 24

MOLYBDENUM + 1/2% TITANIUM (COATING W2 CHROMALLOY)

BASE ALLOY ONLY

MOLYBDENUM -------- 99.48%

TITANIUM ---------- 0.47%

BY SPECTROGRAPHIC ANALYSIS

	BASE ALLOY	COATING
ALUMINUM	ND	0.08%
BORON	ND	0.04%
CHROMIUM	ND	0.48%
COPPER	ND	0.003%
IRON	0.005%	0.09%
MANGANESE	ND	0.01%
MOLYBDENUM	High	High
SILICON	0.01%	High
TITANIUM	medium	0.28%

(NOTE: All other elements not detected.)

TABLE 25

SILICONIZED ATJ GRAPHITE

BY WET CHEMICAL ANALYSIS

CARBON	88.97%
SILICON	8.97%

BY SPECTROGRAPHIC ANALYSIS

SILVER	0.002%
ALUMINUM	0.10%
BORON	0.002%
BARIUM	0.01%
CALCIUM	0.14%
CHROMIUM	0.01%
COPPER	0.002%
IRON	0.10%
MAGNESIUM	0.005%
MANGANESE	0.002%
MOLYBDENUM	0.01%
SODIUM	0.005%
NICKEL	0.002%
TITANIUM	0.03%
VANADIUM	0.001%
TUNGSTEN	0.07%
ZIRCONIUM	0.01%
POTASSIUM	0.005%

(NOTE: All other elements not detected.)

TABLE 26

TANTALUM

BY SPECTROGRAPHIC ANALYSIS

IRON	0.001%
MOLYBDENUM	0.015%
COLUMBIUM	0.02%
SILICON	0.001%
TUNGSTEN	0.02%
TANTALUM	Balance

(Note: All other trace elements not detected.)

TABLE 27

MOLYBDENUM

BY SPECTROGRAPHIC ANALYSIS

PARTS PER MILLION

COPPER	30
IRON	50
MOLYBDENUM	Balance

(Note: All other trace elements not detected.)

TABLE 28

TUNGSTEN CARBIDE (WC)

BY WET CHEMICAL ANALYSIS

TUNGSTEN	93.71%
CARBON	5.88%

BY SPECTROGRAPHIC ANALYSIS

SILVER	N.D.
ALUMINUM	10 PPM
ARSENIC	N.D.
GOLD	N.D.
BORON	N.D.
BARIUM	N.D.
BERYLLIUM	N.D.
BISMUTH	N.D.
CALCIUM	N.D.
CADMIUM	N.D.
COBALT	N.D.
CHROMIUM	N.D.
COPPER	10 PPM
IRON	80 PPM
GALLIUM	N.D.
GERMANIUM	N.D.
HAFNIUM	N.D.
INDIUM	N.D.
IRIDIUM	N.D.
LITHIUM	N.D.
MAGNESIUM	N.D.
MANGANESE	N.D.
MOLYBDENUM	10 PPM
SODIUM	N.D.
COLUMBIUM	N.D.
NICKEL	N.D.
OSMIUM	N.D.
LEAD	N.D.
PALADIUM	N.D.
PLATINUM	N.D.
RHODIUM	N.D.
RUTHENIUM	N.D.
ANTIMONY	N.D.
SILICON	10 PPM
TIN	N.D.
STRONTIUM	N.D.
TANTALUM	N.D.
TELLURIUM	N.D.
THALLIUM	N.D.
TITANIUM	N.D.
VANADIUM	N.D.
TUNGSTEN	High
ZINC	N.D.
ZIRCONIUM	N.D.

(N.D. = Not Detected)
(PPM - Parts Per Million)

TABLE 29

TUNGSTEN CARBIDE (W_2C)

BY WET CHEMICAL ANALYSIS

TUNGSTEN	96.82%
CARBON	3.15%

BY SPECTROCHEMICAL ANALYSIS

ALUMINUM	< 8 PPM
COPPER	< 10 PPM
IRON	40 PPM
MOLYBDENUM	10 PPM
SILICON	< 10 PPM

(NOTE: All other trace elements not detected.)
(PPM = Parts Per Million)

TABLE 30

ZIRCONIUM

BY SPECTROGRAPHIC ANALYSIS

ALUMINUM	0.005%
CHROMIUM	0.03%
COPPER	0.001%
IRON	0.31%
HAFNIUM	0.01%
MANGANESE	0.001%
MOLYBDENUM	0.01%
NICKEL	0.002%
SILICON	0.005%
TITANIUM	0.002%
ZIRCONIUM	Balance

(NOTE: All other trace elements not detected.)

TABLE 31

TANTALUM NITRIDE

BY WET CHEMICAL ANALYSIS

TANTALUM	95.84%
NITROGEN	3.53%
SILVER	N.D. <5 PPM

BY SPECTROCHEMICAL ANALYSIS

ALUMINUM	70 PPM	MOLYBDENUM	2000 PPM
ARSENIC	N.D. <100 PPM	SODIUM	20 PPM
BORON	N.D. <10 PPM	COLUMBIUM	300 PPM
BARIUM	N.D. <10 PPM	NICKEL	40 PPM
BERYLLIUM	N.D. <10 PPM	LEAD	N.D. <10 PPM
BISMUTH	N.D. <10 PPM	ANTIMONY	N.D. <50 PPM
CALCIUM	50 PPM	SILICON	20 PPM
CADIUM	N.D. <10 PPM	TIN	N.D. <10 PPM
COBALT	N.D. <10 PPM	STRONTIUM	N.D. <10 PPM
CHROMIUM	70 PPM	TELLURIUM	N.D. <100 PPM
COPPER	N.D. <10 PPM	THALLIUM	N.D. <10 PPM
IRON	1900 PPM	TITANIUM	600 PPM
GERMANIUM	N.D. <10 PPM	VANADIUM	1200 PPM
HAFNIUM	N.D. <100 PPM	TUNGSTEN	500 PPM
INDIUM	N.D. <10 PPM	ZINC	N.D. <50 PPM
LITHIUM	N.D. <10 PPM	ZIRCONIUM	N.D. <50 PPM
MAGNESIUM	50 PPM	POTASSIUM	20 PPM
Manganese	5 PPM		

NOTE: N.D. = Not Detected, less than
PPM = Parts Per Million

TABLE 32

PYROLYTIC GRAPHITE

BY SPECTROGRAPHIC ANALYSIS

ALUMINUM ----- 1 PPM

IRON --------- 3 PPM

MAGNESIUM ---- 1 PPM

SILICON ------ 5 PPM

CARBON ------ Balance

(Note: All other trace element not detected.)
PPM = Parts Per Million

TABLE 33

TUNGSTEN

SINGLE CRYSTAL

BY SPECTROCHEMICAL ANALYSIS

MOLYBDENUM ------- 10 PPM

TUNGSTEN -------- Balance

Note: PPM = Parts Per Million

APPENDIX B

X-RAY DIFFRACTION CONSTANTS

TABLE 34

X-RAY CONSTANTS FOR TANTALUM NITRIDE

BEFORE EMISSIVITY MEASUREMENT

		A.S.T.M. STANDARD VALUES		
d	I/I_1	d	I/I_1	hkl
2.64	50	2.66	45	100
2.45	50	2.47	45	002
2.32	100	2.34	100	101
1.80	30	1.80	65	102
1.52	30	1.53	90	110
1.39	30	1.39	100	103
1.32	10	1.32	20	200
1.29	30	1.30	100	112
1.27	20	1.27	90	201
1.22	10	1.23	20	004
1.16	10	1.16	45	202
1.11	10	1.12	45	104
1.03	30	1.03	90	203
0.996	5	0.999	65	210
0.978	20	0.980	110	211
0.956	15	0.963	100	114
0.920	30	0.930	100	212
		0.907	20	204
0.880	10	0.883	65	300
0.851	15	0.858	100	213
		0.834		302
0.828	10	0.824		006
		0.797		205
		0.782		303

System: Hexagonal

$A_o = 3.06$

$C_o = 4.95$

TABLE 35

X-RAY CONSTANTS FOR TANTALUM NITRIDE

AFTER EMISSIVITY MEASUREMENT

		A.S.T.M. STANDARD VALUES		
d spacing	I/I_1	d	I/I_1	hkl
2.61	30	2.66	45	100
2.42	35	2.47	45	002
2.29	100	2.34	100	101
2.02	100	---	---	---
1.78	30	1.80	65	102
1.60	5	---	---	---
1.52	30	1.53	90	110
1.39	40	1.39	100	103
1.319	10	1.32	20	200
1.295	40	1.30	100	112
1.27	30	1.27	90	201
		1.23	20	004
1.227	15	---	---	---
1.16	10	1.16	45	202
1.113	15	1.12	45	104
1.026	25	1.03	90	203
0.995	10	0.999	65	210
.977	30	.980	110	211
.955	20	.963	100	114
		.930	100	212
.921	15B	---	---	---
		.907	20	204
.898	10	---	---	---
.878	20	.883	65	300
.850	30	.858	100	213
		.834		302
		.824		006
		.797		205
		.782		303

System: Hexagonal

$A_o = 3.06$

$C_o = 4.95$

TABLE 36

X-RAY CONSTANTS FOR PYROLYTIC GRAPHITE

NORMAL TO "AS DEPOSITED" SURFACE - "a - b" PLANE		A.S.T.M. Standard Values for Single Crystal Graphite		
d spacing	I/I_1	d spacing	I/I_1	hkl
3.43	100	3.37	100	002
1.71	60	1.682	8	004
1.41	5	1.12	2	006
NORMAL TO SURFACE OF "c" PLANE				
2.13	100	---	---	---
1.23	20	---	---	---

TABLE 37

X-RAY CONSTANTS FOR TUNGSTEN

SINGLE CRYSTAL

		A.S.T.M. STANDARD VALUES		
d spacing	I/I_1	d spacing	I/I_1	hkl
2.24	<5	2.238	100	110
1.581	100	1.582	15	200
1.30	<5	1.292	23	211
		1.1188	8	220
		1.0008	11	310
		0.9137	4	222
		.8459	18	321
		.7912	2	400

(cubic A_o = 3.1648)